Resolving temporal links between the Högberget granite and the Wigström tungsten skarn deposit in Bergslagen (Sweden) using trace elements and U-Pb LA-ICPMS on complex zircons

Anders Plan

Dissertations in Geology at Lund University,
Master's thesis, no 580
(45 hp/ECTS credits)

Department of Geology
Lund University
2020

Resolving temporal links between the Högberget granite and the Wigström tungsten skarn deposit in Bergslagen (Sweden) using trace elements and U-Pb LA-ICPMS on complex zircons

Master's thesis

Anders Plan

Department of Geology
Lund University
2020

Contents

Cover Picture: Main pit at the Wigström deposit, looking south west, photo: Anders Plan. Inset: BSE image of a devilishly good looking zircon from the Wigström deposit.

Abstract

ANDERS PLAN

Plan, A., 2020: Resolving temporal links between the Högberget granite and the Wigström tungsten skarn deposit in Bergslagen (Sweden) using trace elements and U-Pb LA-ICPMS on complex zircons. *Dissertations in Geology at Lund University*, No. 580, 58 pp. 45 hp (45 ECTS credits).

Abstract: Combined U-Pb and REE trace element LA-ICPMS analyses were performed on zircons, from the scheelite-bearing Wigström skarn, associated micro-granitic dykes and the highly evolved parental Högberget (*sensu stricto*) granite. Combined systematic of zircon typology and microtextures, trace elements and isotopic chemistry suggest the presence of several diverse zircon types, spanning from early- to late- magmatic stage into a hydrothermal stage. Early stage magmatic zircons (type M1 and M2-S) have high concentrations of U (3300–11500 ppm), Th (1500–7300 ppm), REEs (average ΣREE_n: 11500) and Pb-C signatures and yield highly discordant data. Typological features are varying, but the majority consists of prismatic crystals with oscillatory zonations. In comparison, late stage magmatic zircons (type M2) have lower concentrations of U (200–3000 ppm), Th (100–1900 ppm), REEs (average ΣREE_n: 7600) and Pb-C signatures (e.g. average ^{204}Pb CPS: 300). Typological features include irregular, quasi-smooth forms which lack internal zonations. Geochronological analyses yield concordant data, after interpretation an $^{207}Pb/^{206}Pb$ weighted mean age of ~1.8 Ga is achieved. Hydrothermal zircon (skarn hosted, type H) associates with hydrothermal quartz, calcite, fluorite and scheelite within the skarn. Type H zircons shares similarities with type M2, yielding low concentrations of U (100–6200 ppm), Th (1–1500 ppm), and Pb-C signatures (e.g. average ^{204}Pb CPS: 300), but slightly higher concentrations of REEs (average ΣREE_n: 17800). Typological features display various forms, i.e. skeletal, irregular, oblong, and typically lacks prisms. Internal textures vary from zoned to homogenous, and spongy textures are common. Geochronological data are scattered, but display a concordant cluster around 1.8 Ga, calculated as $^{207}Pb/^{206}Pb$ weighted mean age of 1795±20 Ma (2.0 MSWD). The achieved ages further fortify a ~1.8 Ga for the tungsten metallogenesis in Bergslagen. Magmatic (early- and late types) and hydrothermal zircon can be distinguished via trace elemental discrimination diagram and in CI-chondrite normalized spidergrams. For discrimination diagram, Th versus Th/U, U versus Th, and ΣREE_n versus Th diagrams clearly displays evolutionary transitional trend between the different zircon types. In spidergrams, Magmatic zircons have typical patterns for magmatic zircons (but shows LREE enrichments), whereas hydrothermal zircons display a convex pattern, which clearly distinguish the zircon populations apart.

Keywords: Bergslagen, Wigström, Högberget, geochronology, geochemistry, U-Pb, REE, trace element, zircon, hydrothermal zircon, LA-ICPMS, SEM, skarn, tungsten, wolfram, scheelite, deposit, ore, critical raw material.

Supervisor(s): Ulf Söderlund (LU), Edward Lynch (SGU)

Subject: Bedrock Geology

Anders Plan, Department of Geology, Lund University, Sölvegatan 12, SE-223 62 Lund, Sweden. E-mail: plan.anders@gmail .com

Sammanfattning

ANDERS PLAN

Plan, A., 2020: Undersökning av den tidsmässiga relationen mellan Högberget-graniten och Wigström-tungstensmineraliseringen i Bergslagen (Sverige) med hjälp av spårelement och U-Pb LA-ICPMS på komplexa zirkoner. *Dissertations in Geology at Lund University*, No. 580, 58 s. 45 hp (45 ECTS credits).

Sammanfattning: Kombinerade U-Pb och REE-spårelements LA-ICPMS-analyser utfördes på zirkoner från det scheelitbärande Wigström-skarnet, mikrogranitiska gångar och Högberget (*sensu stricto*) graniten. Utifrån kombinerad systematiskt baserat på zirkontypologi och mikrotexturer, spårelement och isotopkemi antyds förekommandet utav olika zirkontyper, vars bildningar har tolkats att förekomma från ett tidigt till ett sent magmatiskt stadium, samt vid övergången till ett hydrotermalt system. Magmatiska zirkoner i tidigt magmatiskt stadium (av typ M1 och M2-S) uppvisar höga koncentrationer av U (3300–11500 ppm), Th (1500–7300 ppm), REEs (medelvärde på ΣREEn: 11500) och Pb-C-signaturer, geokronologiskt data plottar diskordant. Typologiska särdrag inkluderar ett brett spektrum, dock består populationens främst utav prismatiska kristaller med karaktäristiska tillväxtzoneringar internt. I jämförelse har magmatiska zirkoner i ett sent magmatiskt stadie (typ M2) låga koncentrationer av U (200–3000 ppm), Th (100–1900 ppm), REEs (genomsnitt ΣREEn: 7600) och Pb-C-signaturer (t.ex. genomsnitt ^{204}Pb CPS: 300). Typologiska särdrag inkluderar oregelbundna, icke prismatiska former som helt saknar interna zoneringar. Geokronologisk data plottar konkordant och lägre diskordant, efter tolkning uppnås ett viktat ^{207}Pb/^{206}Pb medelvärde av ~1.8 Ga, vilket anses representera Högberg granitens kristallisations ålder. Den hydrotermala zirkonpopulationen (skarnzirkoner, typ H) associeras tillsammans med hydrotermala faser (tex. kvarts, kalcit och fluorit) och scheelit, de delar likheter typologiskt med typ M2 zirkoner, och likmässigt uppvisar låga koncentrationer av U (100–6200 ppm), Th (1–1500 ppm) och Pb-C signaturer (t.ex. genomsnitt ^{204}Pb CPS: 300), men något högre koncentrationer av REE (genomsnitt ΣREEn: 17800). Stora variationer förekommer typologiskt, former varierar från t.ex. skeltala, oregelbundet, avlångt och är generellt oprismatiska, interna strukturer varierar från zonerade till homogena, och ”spongey” texturer är vanliga. Geokronologiska data ger en bred spridning, men med ett representativt kluster runt 1.8 Ga, som vidare uppnår ett viktat ^{207}Pb/^{206}Pb medelvärde 1795±20 Ma (2,0 MSWD). De magmatiska och hydrotermala zirkon populationer kan särskiljas via diverse spårelementsdiagram, och även i CI-chondrit normaliserade ”spidergrams”. I bivarata diagram som: Th mot Th/U, U mot Th och ΣREEn mot Th kan man tydligt urskilja övergångstrend mellan de olika zirkontyperna (d.v.s. från typ M1 till M2 till H). I CI-normaliserade ”spidergrams” innehar de magmatiska zirkonerna särtypiska mönster för magmatiska zirkoner (men visar LREE-anrikning), medan hydrotermala zirkoner uppvisar ett konvext mönster.

Nyckelord: Bergslagen, Wigström, Högberget, geokronologi, geokemi, U-Pb, REE, spårelement, zirkon, hydrotermal zirkon, LA-ICPMS, SEM, skarn, tungsten, wolfram, scheelite, fyndighet, malm, kritisk råvara.

Handledare: Ulf Söderlund (LU), Edward Lynch (SGU)

Ämnesinriktning: Berggrundsgeologi

Anders Plan, Geologiska institutionen, Lund Universitet, Sölvegatan 12, SE-223 62 Lund, Sverige. E-mail: plan.anders@gmail .com

1 Introduction

Tungsten (W), also known as Wolfram, is notable for its material robustness (e.g. Lassner & Schubert 1999 and the references therein) and is mainly used to manufacture composite materials and alloys for industrial, medical and military applications. In the daily life, tungsten is commonly recognized as alloys, in form of hardmetals (cemented carbides) for manufacturing tools. The metal is highly coveted on the global market, broadly recognized for having outstanding mechanical properties e.g. very high hardness (>9 Mohs), ductility and fracture toughness (Hegeman et al. 2001). Globally, China accounts for the majority of tungsten production (>80%), and also has the largest reserves in the world, ~1900000 tons (>50%) (Jifu et al. 2015; www.usgs.gov). Currently, the global market is strictly regulated, as China has imposed tungsten export quotas, causing the price to skyrocket over the last decade. As a response, the European commission has assigned tungsten as a critical raw material (CRM) as the metal is regarded vital for Europe's economy and ranks as the highest CRM regarding economic importance (ec.europa.eu). This study is part of an EU (European Union) founded project, assign to SGU (Geological Survey of Sweden), with the aim to investigate tungsten potentials around Europe to secure future market stabilities. The SGU project aims to constrain and assess potential resources within the extensively W-mineralized Ludvika area in the Bergslagen region, which includes voluminous tungsten occurrences and older mined deposits such as e.g. the Yxsjöberg and the Wigström deposits.

The study of accessory minerals in rocks can provide important information regarding different evolutionary -stages and processes. Zircon ($ZrSiO_2$) is undoubtedly the most widely used accessory mineral due to its ubiquitous presence in the geological record, its ability to incorporate and retain high abundancy of incompatible elements (e.g. U-Pb-Th and REE), has a low elemental diffusivity and is highly refractory. As a result, zircon has chiefly been employed for U-Pb dating, yielding accurate and precise emplacement age, and for trace element geochemistry (e.g. REEs) whereas variable ratios can provide insights of controlling geological processes (e.g. Wang et al. 2016). As a assecory mineral zircon has a strong potential to influence trace elemental behavior during magmatic crystallization. Therefore, incorporated zircon trace elements can provide significant information of hydrothermal processes, and metallogenesis (Li et al. 2014 and the reference therein). However, studies from recent decades reveals that refractory elements, such as e.g. zirconium (Zr), can be mobilized and re-mobilized over a broad range of geological settings—allowing zircon to form in early- to late stages in a magmatic system, and also forming in later, transit, periods into a hydrothermal system, as precipitated "hydrothermal zircon" (Hoskin & Schaltegger 2003). The latter, can originate from fluid-saturated magma related post-magmatic fluids. It has further been shown that zircon can crystalize and/or be affected at relatively low temperatures of 300–600°C, in hydrothermal systems (Schaltegger 2007). Recognition of hydrothermal zircons is however not straightforward as diagnostic characteristics differs from location to location. Discrepancy includes typology, morphology, microtextures and geochemistry. The best arguments, so far, for zircon of hydrothermal origin are based on constrains from petrological- and paragenetic textures i.e. grains occurring in hydrothermal phases (e.g. quartz) with other hydrothermal minerals (e.g. sulfides), and the incorporation of hydrothermal mineral inclusions (Schaltegger 2007). Further, hydrothermal zircon and hydrothermal overprints commonly display almost complete extinction in cathodoluminescence (CL; c.f. Kozlik et al. 2016; Wang et al. 2016), which can further be used as an preliminary interpretation tool for hydrothermal processes. In the advent of recent advancements of high spatial resolution techniques (e.g. LA-ICPMS, SIMS), hydrothermal zircons have been utilized to constrain e.g. ore-emplacement via U-Pb ages of mainly metasomatically induced deposits, and thus providing ages of hydrothermal events related to mineralizations i.e. yielding ages of the deposit (e.g. Wang et al. 2016).

The main aim of this study is to provide new absolute ages of both the Wigström tungsten deposit and the Högberget granite, via LA-ICPMS U-Pb zircon dating. Supplemented studies include: zircon geochemistry, zircon systematics, and skarn/ore distribution within the strata in relation with the Högberget granite. This will provide a comprehensive insight in skarn genesis at the Wigström deposit, and further providing details for better understanding the Bergslagen tungsten metallogenesis.

2 Background

2.1 The Bergslagen region

The 1.91–1.89 Ga Bergslagen region constitutes a part of the 2.0–1.8 Ga the Svecokarelian orogeny (Sk) (Fig.1, inset map), which encompass a large portion of Sweden and Finland (Fig. 1, inset map). The region is delimited by the Archean (A) and Korelian (K) subprovinces to the north-east, and the Caledonian- (Ca) and Sveconowegian orogeny (Sn) westerly (Fig 1, inset map). Geographically, the Bergslagen region covers an area of ~320x280 km (Fig 1, red square in inset map), approximately from Falun in the north down to Motala in the south and from Filipstad in the west to Stockholm in the east (Fig. 1). The Bergslagen

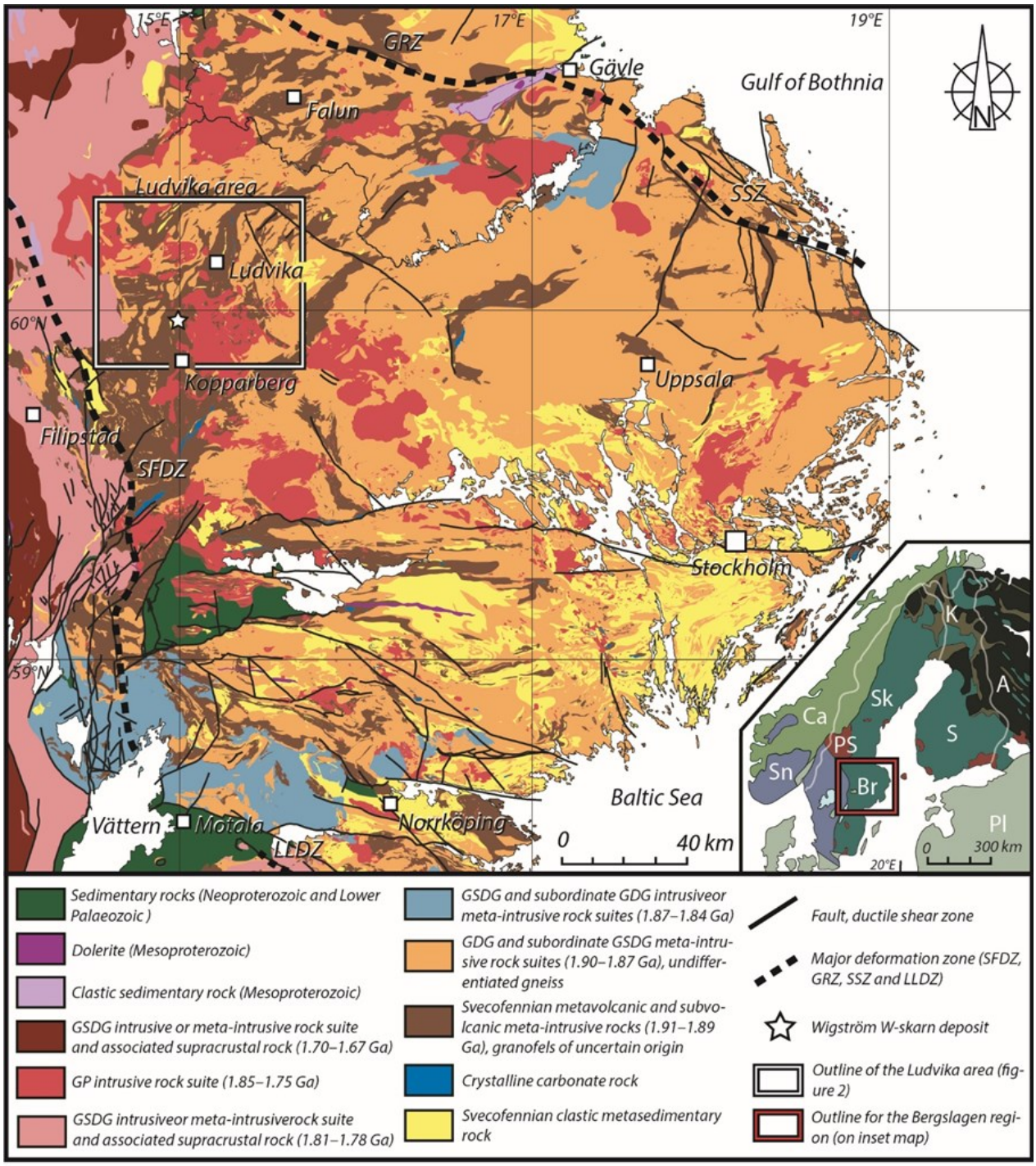

Fig. 1. Simplified bedrock map of the Bergslagen region (modified after Stephen et al. 2009). Inset map comprise main lithounits of Scandinavia and Finland (modified after (Bergman et al. 2001; 2012) and highlights the location of the Bergslagen region (red and black square). Inset map abbreviations: Br = Bergslagen region, Sk = Svecokarelian orogen, Sn = Sveconorwegian orogen, Ca = Caledonian orogen, Pl = Platformal sedimentary cover rocks, A = Archaean rocks, K = Karelian rocks, S = Svecofennian supracrustal rocks and Svecokarelian intrusive rocks, PS = post-Svecokarelian rocks. The Ludvika area (referring to Fig. 2) are highlighted with a black and white square. Thick dotted lines: major faults and deformation zones.

region is an extensive Proterozoic pluto-volcano-metallogenic complex comprising an 8–10 km thick supracrustal succession of mainly Paleoproterozoic metavolcanic rocks with subordinate intercalated marble, clastic metasedimentary- and intrusive rocks of younger ages (Fig. 1). In classic Bergslagen literature the metavolcanic-succession refers to the leptite-hälleflinta formation (e.g. Geijer & Magnusson 1944; Oen et al. 1982). In this thesis the nomenclature adopted from Beunk and Kuipers (2012) will instead be used; The Bergslagen group (BG). The BG consists of crudely sorted mixture of ash-, silt-, pumice- and la-

pilli stones, collectively denoted as ignimbrites i.e. depositions from pyroclastic flows (Allen et al., 1996). Westerly and delimited by the Sveconorwegian frontal deformation zone, the region is dominated by felsic metavolcanites with superimposed metasediments (Fig. 1). Further east, the felsic volume successively diminishes (Fig. 1), and mafic to intermediate mafic metavolcanics interposed within metasediments prevails (Lundström, 1987). This observation was interpreted by Lundström (1987) as a predominant volcano-centre, situated in the west which progressively provided the eastern parts with materials. Based on Lundströms reasoning, Allen et.al. (1996) interpreted the Bergslagen region as evolving during two main episodes. The first episode commenced during an extensional tectonic regime accompanied by explosive volcanic eruptions, pyroclastic flows and magmatism. Later followed waning magmatism, whereas the tectonic setting reverted to a compressional state. Allen et.al. (1996) interpreted these episodes to occur in an extensional back-arc setting on an active continental margin. These volcanic event were active at ~1.91 to 1.89 Ga (see the geochronological summary of Lundström et.al. (1998 and the reference within) and Stephen et.al. (2009 and the reference within)), whereas these eruptions occurred into an unknown Archean basement. As inferred by Allen et.al. (1996), the ejected material was deposited into stagnant and relatively deep water, trailed by immense sedimentation and aquatic fluctuations ranging from shallow water to sub-aerial. Intercalated marble and limestone units are mostly reoccurring in the upper BG-stratigraphy (Allen et al., 1996). Isotopic $\delta^{13}C$ and $\delta^{18}O$ signatures imply that they are of marine sedimentary origin, and thus probably grew as microbial stromatolites in shallow seas coeval with the volcanic eruptions (Allen et al. 2003).

The BG stratigraphy is intruded by voluminous granitoidal rock, recognized as three separate suites (i–iii), distinguishable by their different compositions and ages (Fig. 1). These were affected by various degrees of deformation and metamorphism owning to the Svecokarelian orogeny (Stephens et al., 2009). (i) The GDG (granitoid-dioritoid-gabbroid) suite with subordinate (ii) GSDG (granite-syenitoid-dioritoid-gabbroid) and sub-volcanic meta-intrusive rocks are the oldest of the three i.e. 1.90–1.87 Ga (Fig. 1), and generally plots as I-type granites (Stephens et al. 2009). These intrusions occurred coeval with the volcanism, thus active during the proposed extensional setting by Allen et.al (1996). The GDG suite (i) constitutes the largest area of intrusive rocks within the Bergslagen region, and dominates the central- and eastern parts (Fig. 1). The GSDG suite (ii) (Fig. 1) comprise three episodes of intrusion; late-Svecokarelian GSDG of ages 1.87–1.84 Ga and 1.81–1.78 Ga and a post-Svecokarelian GSDG intrusive of an age between 1.70–1.67 Ga. These suites are included in the 1.85–1.67 Ga Transscandinavian Igneous Belt (TIB; Patchett et al. 1987) which delimits the Bergslagen region westerly (Fig. 1). (iii) The 1.85–1.75 Ga granite-pegmatite (GP) suite occurs as isolated plutonic complex which mainly dominates the north-western and central areas in Bergslagen (Fig. 1). They are subordinate to the previous two granitic suites, and are of focus in this study. The GP suite is a granite *sensu stricto*, interpreted to be of crustal anatectic origin, associated with crustal thickening and migmatization throughout abated stages of the Svecokarelian orogeny. The GP granites occurring as sets of intrusions interpreted to have derived from late- and/or post-tectonic orogenic activities (Johansson 2019 and the reference therein). As a result, the GP suite associates with extensive portions of pegmatites, aplites and granitic dykes (e.g. micro-granite) which often crosscuts the adjacent country rocks, and the granitic further associates with W-F-Mo±Cu mineralizations.

2.2 Granite- and skarn-related W-F-Mo±Cu mineralization in western Bergslagen

The Bergslagen region is known as one of Europe's oldest and most prosperous ore provinces, hosting several thousand deposit and mineral prospects: ~7000 iron oxides- (FeO) and ~1500 base metal sulphide occurrences (e.g. Cu, Pb), ~150 special metal occurrences (e.g. W, Mo) and a few precious metal occurrences (e.g. Au, Ag) of mainly Fe±Mn, Zn-Pb-Cu-Au-Ag-(W-Mo-REE) mineralizations (e.g. Eilu 2012). Historically, exploitation of metallic resources has primarily occurred from polymetallic base metal sulphide deposits (Cu-Pb-Zn; e.g. Falun mine (Zn-Pb-Ag-(Cu-Au)) and Fe-oxide deposits (i.e. Grängesberg mine (Apatite-Fe Kiruna-type)). As of today, Bergslagen has three active mines; Garpenberg (stratabound Zn-Pb-Ag-(Cu)-(Au)), Zinkgruvan (stratiform Zn-Pb-Ag) and Lovisa (Pb-Zn; with additional mining including dolomite and limestone for industrial purposes). The tonnage of the three is relatively small, but the two former yield world class ore-grades.

Western Bergslagen contains numerous W-Mo-F occurrences (Ohlsson 1979) commonly hosted by Orosirian (~1.9 Ga) metasupracrustal rocks (Fig. 2, e.g. Stephens et al. 2009). The largest quantity of these occurrences are found within the Ludvika area (inset square in Fig.1; Fig. 2 geological map for the area). Locally, the mineralization occurs adjacent to leucogranites assigned to the 1.85–1.75 Ma GP intrusive suite (Wilson & Åkerblom 1982; Baker & Hellingwerf 1988). Mineralization generally occurs as intragranitic (e.g. Pingstaberg) and/or as within spatially related calc-silicate skarn horizons within the supracrustal succession, neighbouring parental granitic

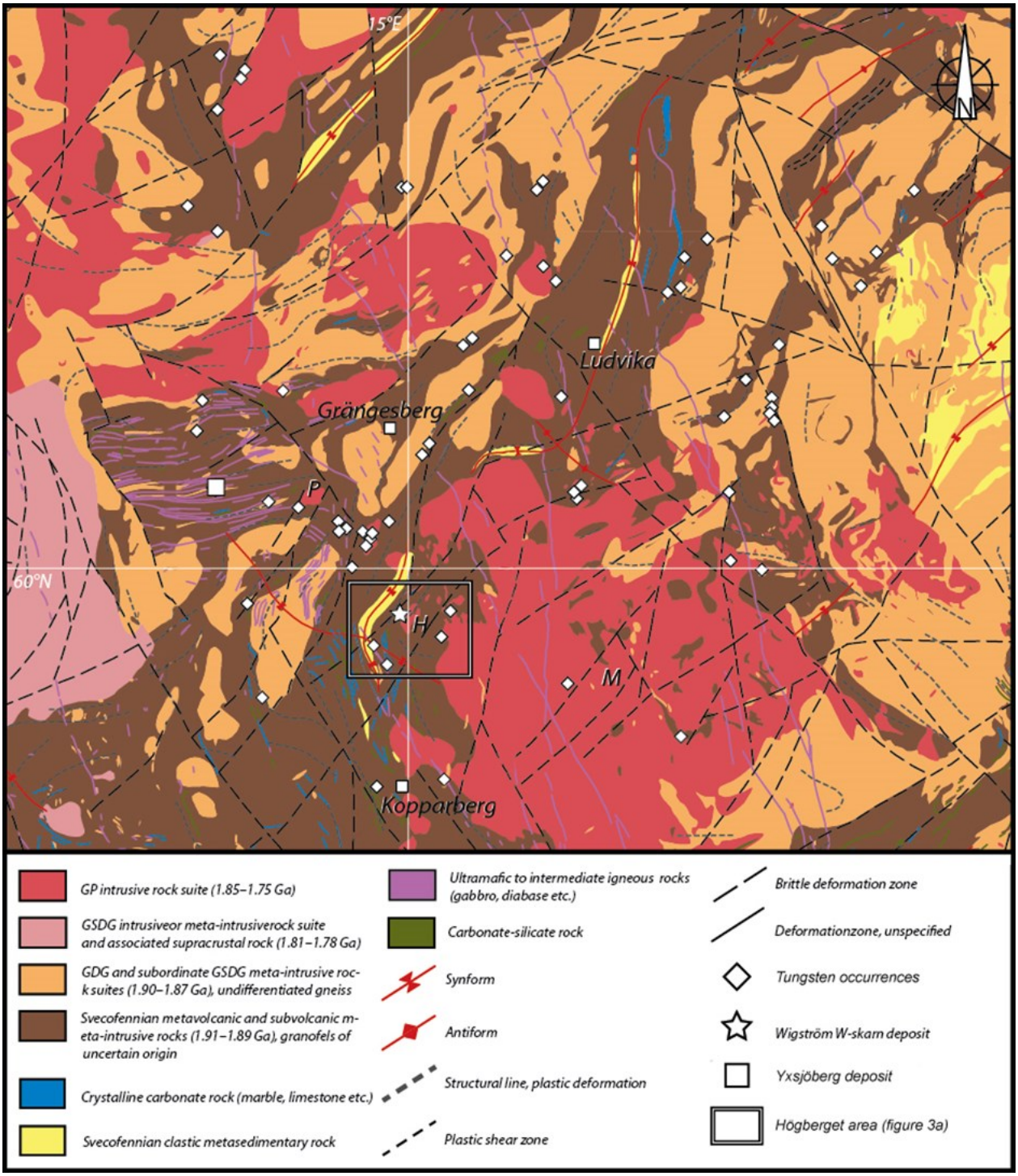

Fig. 2. Simplified bedrock map of the Ludvika area (modified after SGU.se). The star marks the location of the Wigström tungsten deposit, Big square marks the Yxsjöberg tungsten deposit, diamonds marks other tungsten occurrences and deposits. Abbreviations (GP-suits): M = Malingbo granite suit, P = Pingstaberg granite suit, H = Högberget granite suit. Black and white square refers to Fig. 3a

-suit(s) (e.g. Wigström and Högberget, Fig. 2 and Fig. 3). Granite-derived hydrothermal fluids are regarded as the source for W-Mo mineralization (Lindroth 1922; Magnusson 1940; Ohlsson 1979; Hellingwerf et al. 1987; Billström 1990), whereas skarn related mineralization insinuate an epigenetic origin induced by contact metasomatic processes, with the related granites as progenitor (e.g. Bergman et al. 1995; Stephens et al. 2009; c.f. Webster et al. 1997).

In contrast, the world's most prominent tungsten deposits occur as scheelite-skarn mineralizations (Pitfeld et al. 2011 and the references therein), these are often associated in space and time with highly evolved, metalliferous, peraluminous and F-saturated

parental granites (e.g. Webster et al. 1997; Wei et al. 2018; Zhao et al. 2018), and the related skarn formations are mainly a product of contact metasomatism (see Meinert et al. 2005 for skarn review)—as seen in the many W-occurrences within the Ludvika area in Bergslagen. The Bergslagen W-Mo-rich parental granites, such as the investigated Högberget granite (and the GP suite in general) commonly display relative enrichments of F, U, Th, Pb, Sn, Rb, Cs, Ta, Au and LREE and are relatively depleted of Zr in comparison with non-related W-Mo granites within the region (Wilson & Åkerblom 1982; Baker & Hellingwerf 1988; Billström et al. 1988; Stephens et al. 2009). Geochemical analyses of Bergman et. al. (1995) study indicate that the Högberget granite has a composition attributed to that of an evolved fractionated S-type granite, with a peraluminous character. The Högberget granite also display enrichments of incompatible elements such as U, Th, Ga, Ce, Y, Nb and LREE and has a low Zr saturation. Accessory mineral phases within the granite includes fluorite, molybdenite, pyrite and ilmenite (Bergman et al. 1995), thus intragranitic F-enriched and Mo-Py-Ilm bearing. According to Stephens et al. (2009), elevated U and Th content is also a distinct signatures for the GP-suites, whereas the Malingbo-type has amongst the highest granitic U-enrichments in the Svecokarelian terrane, i.e. 22 ppm (Wilson & Åkerblom 1982 and the references therein). Uranium analyses from literature yields a content of 18.54 and 18.70 ppm for the Högberget granite (Baker & Hellingwerf 1988)—an uranium content about 5 to 6 times as high as average granites (U: ~4 ppm according to Artemieva et al. 2017). Similar characteristics with W-Mo granites in the Ludvika area can be seen in the Chinese region Jiangxi, were many of the extensively W-bearing Shimensi granites have similarities with the GP suite granites. The Shimensi granites have e.g. S-type signatures, are highly fractionated and evolved, and are peraluminous, with low Zr contents and U-enrichments, and W-mineralizations occurs e.g. intragranitic and/or in adjacent skarn assemblage (c.f. Wei et al. 2018 and the references therein). This geochemistry is shared with numerous W-deposits and parental granites worldwide, thus these characteristics further support genetic links between the Högberget granite and W mineralization at Wigström deposit.

2.3 Geology of the Wigström-Högberget area

Of the special metal deposits within the Bergslagen region, Tungsten has been mined most successfully, upon which the Yxsjöberg mine stands pre-eminent (Fig. 2). The Yxsjöberg deposit is located ~20 km south-west of Ludvika and was discovered in early 18th century, and during the ongoing century the mine produces scarce amounts of Cu. During the 20th century production shifted focus towards Tungsten in form of skarn-bearing scheelite. A total of 5 Mt W-ore was processed during three phases; 1917–1920, 1935–1963 and 1973–1989, with an average WO_3 content of 0.35% (equivalents to ~15 000 t of pure W). This production represents ~92 % of Sweden's total tungsten production, hence proclaimed as Scandinavia's most prolific W-deposits (SGU 2008). The latter regime (1973–1989) was orchestrated under LKAB:s affiliated company, AB Statsgruvor (ABSG). In order to secure sufficient W-ore for the Yxsjöberg ore-dressing plant, an extensive boulder-tracing (UV) and regional heavy-mineral geochemistry program was founded. In 1976, an area ~10 km north from the old mining town Kopparberg in Ljusnarsberg municipality was found to exhibited high W anomalies. Further investigations concluded the finding of a ~3000 m^2 skarn-body enveloping 1000 m^2 scheelite bearing ore with economically viable W-content. The deposit was later entitled the Wigström deposit (Berglind, 1983).

The Wigström deposit is situated between the Ställdalen synclinal and the Maingbo suite (belonging to the GP-suite), and closely neighbouring the Högberget granite (Fig. 3a, 3b, 3d). The Högberget granite occurs as a small plutonic complex with a surface area of ~2.5 km^2, and is embedded into a biotite-rich felsic metavolcanites (Fig. 3a, 3b, 3d). The granite has an interpreted age of 1750±10 Ma based on discordant ID -TIMS-data (Isotopic Dilution- Thermal Ionization Mass Spectrometry; Bergman et al. 1995). The granite is mainly reddish-grey and with an equigranular texture consisting of medium-sized grains (<1–2.5 mm). The complex has several micro-granitic dykes and pegmatite off-shoots from the body. These often have the similar textures as the parental granite but with a more greyish appearance. At least two of these dykes cross-cuts the Wigström ore at surface level.

The Wigström ore-body (Fig. 3b–3d) is enveloped in an intricate stratigraphic sequence belonging to the Wigström group (Parr & Rickard 1987), which mainly comprises felsic metavolcanites with subordinated metasediments, metabasite, marbles and skarns horizons. Age constrains via molybdenite Re-Os has yielded an age of ~1.8 Ga for the Wigström deposit (Stein et al. 1996; Sundblad et al. 1996; published as abstracts only). Excavation and mining, as an open-pit, was initiated in 1978 and lasted until 1981, during this time the Wigström deposit acted as a satellite deposit to Yxsjöberg ore-dressing plant, and contributed with totally 0.2 Mt of W-ore, with an average WO_3 content of 0.28 % (Berglind, 1983). The open-pit area covers ~350x<50 meters and stretches in a NNE-SSW direction (Fig. 3b, 4a, 4b). The deposit is divided into two pits, here referred to as the main-pit and the northern-pit (Fig. 3b, 4a, 4b). Ore-distribution was comprehended from ~50 diamond drill holes, which was continuously drilled during the mines active years.

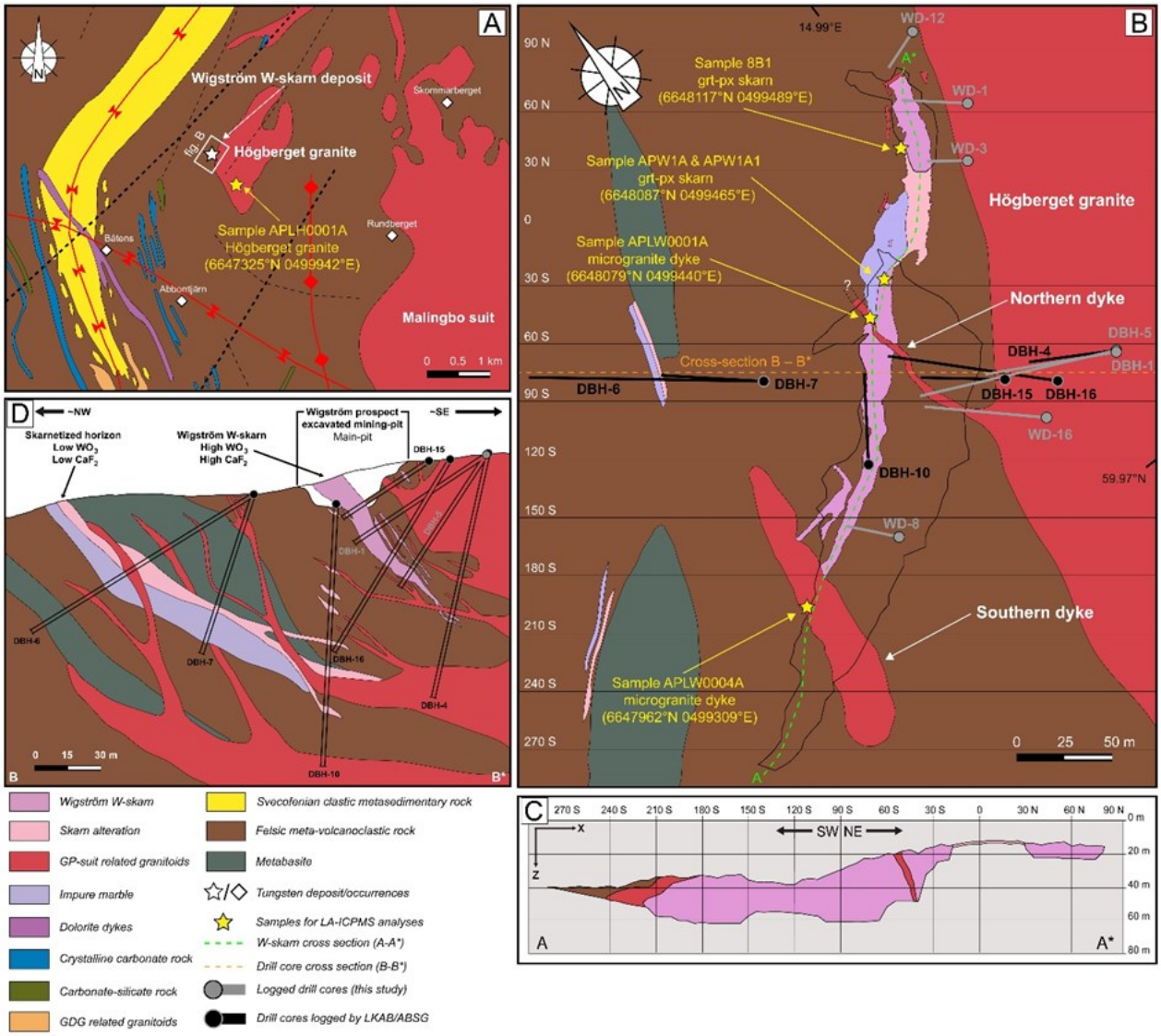

Fig. 3. 3a: Simplified bedrock map of the Wigström tungsten deposits location (white star), white square refers to figure 3b, yellow stars mark the location of this studies samples, diamonds marks W-occurrences in the vicinity. 3b: Simplified geological map of the Wigström tungsten deposit. Black lines mark the excavation site of the deposit, which today is partially water filled (e.g. Fig 4a, 4b), green dotted line (A–A*) refers to figure 3c. Orange dotted line (B–B*) refers to figure 3d. Grey circles with grey lines marks logged drill-holes in this study. Black circles with black lines logged drill-holes by LKAB/ABSG (unpublished reports, 1976; 1981) which are interpolated into cross-section B–B* (Fig. 3d). 3c: Cross-section A–A*; excavation depth and bedrock units according to unpublished reports LKAB reports (1983). 3d: Cross-section B–B*; interpreted geological sketch based on drill-core logs. Grey dots and drill-core name are cores logged in this study. Black dots and drill-core name are cores logged in by LKAB/ABSG (unpublished reports, 1983).

Some of the drill cores are currently stored at the SGU´s drill-core archive in Malå, Sweden. Production ceased due to diminishing scheelite amounts within the strata, as weathering prevailed with depth. Mining excavation extended ~40 m vertical into the bedrock (Fig. 3c, 3d). Today the excavation site is drenched in water, and skarn outcrops only exist at the NNW-tip of the main pit, here entitled “skarn horizon-wall” (Fig. 4c) and along the SW-borders of the northern-pit (Fig. 4b).

The skarn horizon-wall (following text relates to Fig. 4c) encompasses the hanging wall which is composed of various degree of skarnified country rock and several skarn units. A clear paragenetic sequence is distinguishable—interpreted to reflect skarn prograde stages and retrograde stages. The retrograde stage consists of centimetre to decimetre sized aplitic veins infested along the hanging wall. In relation to the veins, the skarnification becomes gradually intensified and chaotic. The veins mainly contain quartz, calcite, fluorite and accessory minerals occurs as disseminated molybdenum clasts (<1.5 cm in size), scheelite grains (<0.5 mm) and sulfides (e.g. pyrite and chalcopyrite), and occasionally inclusions of garnet, pyroxene, and hornblende are found within. The prograde stage com-

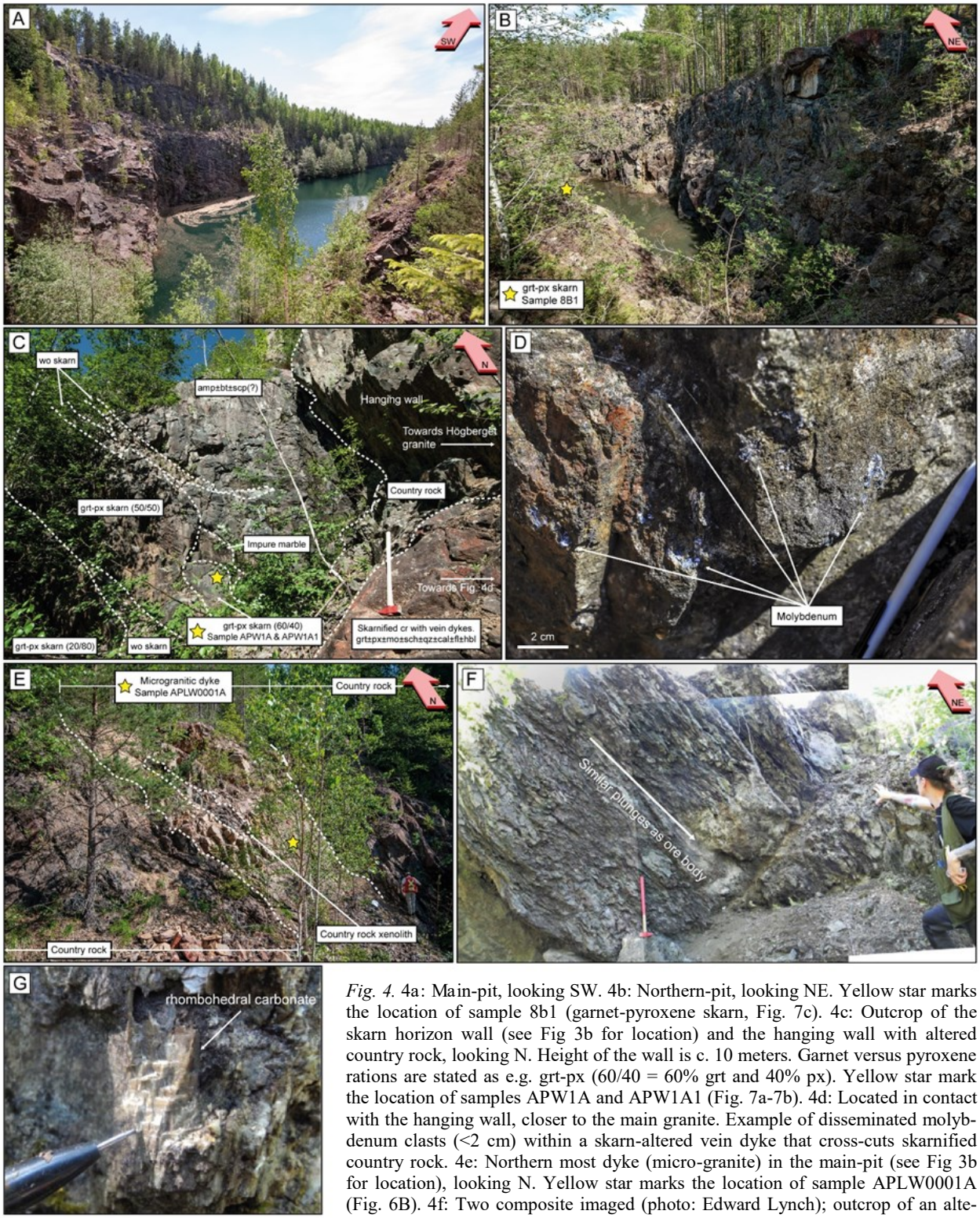

Fig. 4. 4a: Main-pit, looking SW. 4b: Northern-pit, looking NE. Yellow star marks the location of sample 8b1 (garnet-pyroxene skarn, Fig. 7c). 4c: Outcrop of the skarn horizon wall (see Fig 3b for location) and the hanging wall with altered country rock, looking N. Height of the wall is c. 10 meters. Garnet versus pyroxene rations are stated as e.g. grt-px (60/40 = 60% grt and 40% px). Yellow star mark the location of samples APW1A and APW1A1 (Fig. 7a-7b). 4d: Located in contact with the hanging wall, closer to the main granite. Example of disseminated molybdenum clasts (<2 cm) within a skarn-altered vein dyke that cross-cuts skarnified country rock. 4e: Northern most dyke (micro-granite) in the main-pit (see Fig 3b for location), looking N. Yellow star marks the location of sample APLW0001A (Fig. 6B). 4f: Two composite imaged (photo: Edward Lynch); outcrop of an altered, i.e. impure, marble unit, looking N. Notice that the plunge corresponds to the plunge-angle of the skarn ore-body. 4g: Example of a remnant carbonite clast incorporated within an impure marble outcrop (photo: Edward Lynch).

prises skarn units, mainly garnet-pyroxene skarn with various ratios—but generally has a distal increase of pyroxene and a decrease of garnet from the hanging wall. Wollastonite skarn seems to be tectonically controlled, occuring as semi-brittle horizons in faults in-between skarn and country rock units. An altered unit of, mainly, amphibolite, biotite±scapolite(?) is situated aside from the hanging wall and are in contact with the garnet-pyroxene skarn. Further, subordinate units of impure marble (~1x1 meter) is also present with the skarn assemblage, which suggest these to be the skarn progenitor. Larger units of impure marble outcrops are

scatters just NE of the wall, the marble textures there suggest a similar plunge angle and orientation as the Wigström ore-body (~50–60°; Fig. 4f compared to Fig. 3d). Small portions of these outcrops also contains preserved rhombohedral carbonates (Fig. 4g) inferred to be the precursor unit of the marble. The skarn horizon-wall has a close relationship with one of the two micro-granitic dykes that cross cuts the main-pit, and the northern dyke is located just ~10 meters SW of the wall (Fig. 4e).

2.4 Previous geochronology of GP suite granites and related mineralization, and analytical challenges

Little is known about the timing of W-Mo mineralization at the Wigström deposit, as previous Re-Os geochronology are published in abstract only, and therefore should not be seen as absolute. However, these ages coincide with recent constrains of the Bergslagen W-metallogenesis: ~1.8 Ga (see coming discussion), and thus points towards a similar age for the Wigström deposit. Further, the only study with a focus on the Högberget granite is done by Bergman et. al. (1995), age constrains of the granite are however based on highly discordant data and should therefore be treated with caution. The overall quality of historical geochronological data for GP suite granites in Bergslagen, in terms of precision and accuracy, varies somewhat (see Table 5 in Stephens et al. 2009). Dating of GP intrusions in the 1980s and 1990s mainly relied on zircon multi-grain U-Pb TIMS analyses which typically yielded discordant and relatively imprecise ages (Stephens et al. 2009 and the references therein). Thus, genetic links between specific granites and proximal W-Mo-F mineralization based on accurate and precise age constraints has remained equivocal, although the role of ~1.8 Ga Late Svecofennian magmatism as a driver of skarn W mineralization in western Bergslagen is broadly accepted (Stephens et al. 2009, Stephens 2013).

Historical U-Pb TIMS dating utilized multigrain isotopic dissolution (ID) where uranium and lead extraction followed the methods of Krogh (1973) and Manhes et al. (1978) (e.g. Bergman et al. 1995). Basically, large amounts of zircon grains, up to milligrams (>100 grains), were dissolved with hydrofluoric acid and all of the extracted U and Pb within the dissolution was analysed with a mass-spectrometer. This approach neglects possible heterogeneous zircon domains as all U, Th and Pb bearing phases (e.g. recrystallized- and metamict areas) are included in the solution. Such analyses could yield data representing the mixing of age domains (e.g. Schoene 2014), as these heterogeneities could contain variable isotopic composition. Evidently this mixing would lead to a disturbed isotopic system (e.g. Košler 2007), which can produce erroneous intercepts compared to single grain analyses (c.f. Söderlund 1996). At best, previously determined U-Pb TIMS ages for GP granites in western Bergslagen represent an average "mixed" age for all analysed U-Pb isotopes contained within the bulk zircon sample (e.g. Larson & Tullborg 1998).

In contrast, modern geochronological techniques like LA-ICPMS and SIMS analyses, combined with detailed zircon textural-petrographic studies using SEM-BSE and -CL imaging, offer high spatial resolution analyses such that zircon internal heterogeneities can be avoided (e.g. Košler 2007; Degryse 2012). Where performed, re-dating GP granites using modern *in situ* techniques appears to yield older igneous ages compared to the previously determined dates. For example, Billström et al. (1988) determined an emplacement age of 1781±46 Ma for the Mo-mineralized Pingstaberg granite using multigrain zircon U-Pb TIMS dating and discordant isotopic data. In comparison, re-dating of the Pingstaberg granite by Lynch et al. (2019) using zircon U-Pb SIMS dating produced a concordant igneous age of 1805±9 Ma, while Re-Os N -TIMS dating of intragranitic molybdenite from the same intrusion yielded an largely identical age of 1801±10 Ma. The similarity of both dates based on independent isotopic systems indicates an accurate emplacement age of ~1805 Ma for the Pingstaberg granite, some 20 million years older than the previous age constraint. These results further demonstrate that some GP-suite intrusions may be older than previously thought, and that previously reported multigrain zircon U-Pb TIMS ages for Late Svecofennian granites in Bergslagen should be treated with caution (e.g. Woodward et al. 2009; Lynch et al. 2019).

3 Study Methods

3.1 Drill-core logging – Documentation and sampling

The Swedish Geological Survey (SGU) facilitates an extensive drill-core archive in Malå, Sweden, where cores from numerus Swedish mines and prospects are stored. Between the years of 1976 to 1981, 51 drill core was unearthed at the Wigström prospect, and some of these was later shipped to Malå for future storage.

The Wigström prospects original drill core text logs, some geochemical analyses of skarn (WO_3, CaF_2, Fe, Mn, Mo, S, Cu) and maps of the claimed prospect area; along with geological sketch maps and profiles, were acquired from Bergstatens and SGUs archive. These documentations were beforehand studied and was used as a reference material for selection drill cores of interest i.e. those which contains skarn with a high distribution of scheelite. The original logs are fairly simple and mainly focus on skarn distribut-

Fig. 5. 5a: Example of a drill-core box at Malå, Sweden. 5b: Scheelite "glow" under UV-C light.

ion, ore concentration with little denotations on other interesting features e.g. sulfides, pegmatites (endoskarn) etc. From the available Wigström collection at Malå, seven drill cores were chosen for sampling and logging; four with an origin in the main pit (DBH-1, DBH-5, WD-8 and WD-16) and three originated in the north pit (WD-1, WD-3 and WD-12; see Fig. 3b). Throughout ten days, these drill cores were sampled and logged with centimetre precision (Fig. 5a – core-box example) with the aim of producing detailed digitalized logs and for better understanding the skarn and ore distribution, and also to get a clearer insight on the lithostratigraphy, alternating skarn assemblage and other features. Documentation and logging was performed according to following parameters: distribution of rock type, mineralogy, litho -transitions and other interesting features and structures (e.g. scheelite, sulfides and alterations). All of the cores were examined with a handheld UV-C field lamp (Fig. 5b), in order to document scheelite distribution. Based on ocular inspection, fluorite, molybdenum and sulfides distribution was also documented. The main logging effort was put on skarn assemblages, neighbouring and/or cross cutting rocks to these assemblages. Additionally, Bergstatens geological maps over the Högberget-Wigström area and a newly produced cross section leapfrog model done by Edward Lynch (unpublished), laid the foundation for producing this thesis geological map of the Wigström prospect and the cross section, were the latter were modified according to the drill core logs results from this study.

3.2 Rock samples, zircon separation and thick section production

Field work was carried out at the Wigström prospect, the adjacent Högberget granite and other surrounding skarn prospects (Yxsjöberg, Elgfall and Sandudden) over six days in June 2018. Field samples were collected from the Wigström skarn deposit, adjacent country rocks, and Högberget granite, and two cross-cutting granitic dykes. Geographical positions of collected samples were recorded using a hand held GPS.

Three granitic samples, were obtained from fresh outcrops: sample APLH0001A (6647325°N 0499942° E; Fig. 6a) from the Högaberget granite, and samples APLW0001A (6648079°N 0499440°E; Fig. 6b) and APLW0004A (6647962°N 0499309°E; Fig. 6c) from two microgranitic dykes that crosscut the Wigström-skarn. Representative and non-weathered rock samples were selected and crushed with a sledge hammer on a clean steel block. The crushed fragments were placed in a grind-barrel of chromium steel and milled into a fine powder. Heavy mineral from the fine powder was separated using a Wilfley-Holman 700 water shaking table, following the procedure of Söderlund & Johansson (2002). Magnetic minerals in the heavy mineral fraction were removed using a neodymium hand magnet. In general, zircons were rather scarce, but approximately 90 zircons were separated from the three samples via handpicking under binocular microscope. The grains were transferred onto adhesive tape and cast into three standard size (25.4 mm) epoxy-resin pucks, followed by conventional grinding and polishing techniques to expose zircon mid-section.

Field samples of skarn were acquired from both fresh outcrops and mine dumps at Wigström. Four garnet-pyroxene skarn hand-samples were selected for further investigation. These samples were sawed, grinded and polished into eight standard-sized rock chips (3x1.8 cm) i.e. "thick sections", two for each sample. Initially, titanite was the main target mineral for U-Pb geochronology in order to date the skarn mineralization, similar to the approach for the Yxsjöberg tungsten deposit by Romer and Öhlander (1994). However, only a few grains of titanite were discovered during SEM-analyses and imaging. Instead, skarn-hosted zircons were discovered, and thus chosen as a replacement for titanite since their relationship indicate that they crystallized co-genetic with the skarn assemblage (see chapter 4.1). Three of the original eight thick sections were selected for further analyses, as these con-

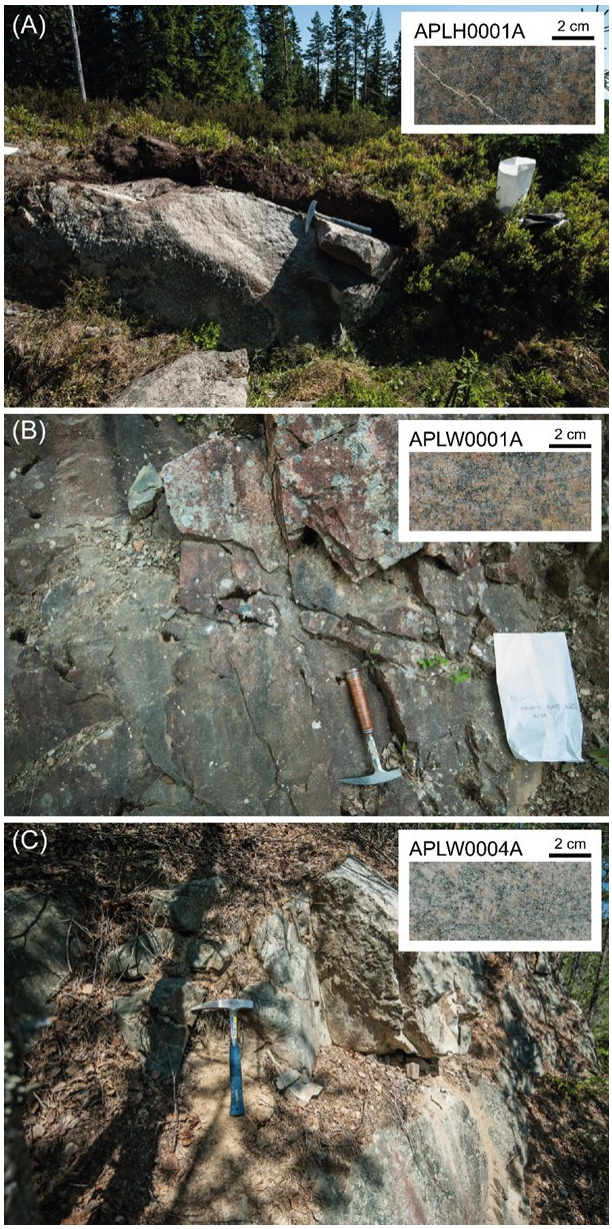

Fig. 6. 6a: Outcrop and sampling site for the Högberget granite, and thicksection (inset picture) – sample APLH0001A. 6b: Outcrop and sampling site of the northern most dyke within the main-pit (sample APW0001A) and thicksection (inset picture), 6c: Outcrop and sampling site of the southern most dyke within the main-pit (sample APW0004A) and thicksection (inset picture).

tained the most prominent and abundant zircon and scheelite populations of the eight investigated samples. Two of these thick sections were derived from one hand-sample, collected at the "skarn-horizon wall" within the main-pit; APW1A and APW1A1 (6648087° N 0499465°E; Fig. 7a and 7b), while another was derived from a hand sample collected at the south-western side of the northern-pit; 8B1 (6648117°N 0499489°E; Fig. 7c).

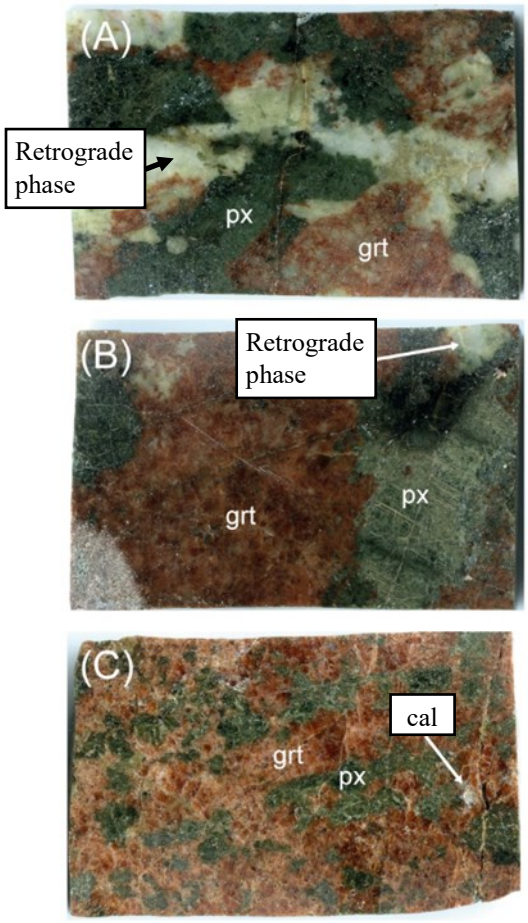

Fig. 7. Investigated thick sections of the garnet-pyroxene skarn. 7a: Sample APLW1A from the main-pit, 7b: Sample APLW1A1 from the main-pit and 7c: Sample 8b1 from the northern-pit.

3.3 Analytical techniques – SEM and LA-ICPMS

Imaging of zircon and skarn were performed at the Department of Geology, Lund University using a Tescan Mira3 High Resolution Schottky Field Emission (FE)-scanning electron microscope (SEM) equipped with Oxford backscattered electrons (BSE), cathodoluminescence (CL) and energy-dispersive X-ray spectroscopy (EDS) detectors (full analytical procedure can be found in appendix 1). Combined zircon U-Th-Pb isotopes and REE trace element analyses were carried out at Lund University in-house Laser Ablation Inductively Coupled Plasma Mass Spectrometry (LA-ICPMS) laboratory, and followed similar analytical protocol as Chaves et al. (2019). The analyses involved ablation of both zircon crystals cast in epoxy-pucks (granitic separates) and *in situ* embedded (skarn thick sections). All acquired geochronological data are quoted with ratio errors at a ± 2σ confidence level. LA-ICPMS set-up are listed in table 1, and detailed analytical methodology can be found in appendix 1.

Tabel 1. LA-ICPMS set-up

Laser ablation system	
Make, Model & type	Photon machines, Analyte G2 excimer laser
Ablation cell & volume	HelEx 2-volume sample cell with eQC
Laser wavelength	193 nm
Pulse width	<4 ns
Fluence	~2.5 J/cm^2
Repetition rate	9 and 12 Hz
Spot size	20x20 µm, 15x27 µm and 14x29 µm
Carrier gas	He carrier gas; N_2 and Ar make-up gas added down-stream from sample chamber
Background collection	30 seconds
Ablation duration	30 seconds
Cell carrier gas flow	0.8 l/min He and 6.5 ml/min N2
ICP-MS Instrument	
Make, Model & type	Bruker Aurora Elite Quadrupole ICP-MS
Sample introduction	Via 2 mm ID PFTE tubing with insert "squid"
RF power	~1300 W
Make-up gas flow	~0.95 l/min Ar
Detection system	Single collector discrete dynode electron multiplier or DDEM
Masses measured (dwell time in milliseconds)	^{29}Si(6), ^{90}Zr(7), ^{139}La(9), ^{140}Ce(9), ^{141}Pr (9), ^{146}Nd(9), ^{147}Sm(9), ^{153}Eu(8), ^{157}Gd (7), ^{163}Dy(7), ^{172}Yb(7), ^{202}Hg(6), ^{204}Pb(9), ^{206}Pb(9), ^{207}Pb(12), ^{232}Th(7), ^{238}U(7)
Total scan time	150 milliseconds

4 Results

4.1 Skarn petrology

Based on results from drill-core logging (appendix 2) and field work, four main lithologies are recognized at the Wigström deposit. These are: (1) intermediate to felsic metavolcaniclastic wall rocks (mainly various degree of skarn altered BG; Fig. 4c, 8a and appendix 2), (2) a remnant marble horizon or zones that is intercalated with the metavolcaniclastic sequence in the deposit footwall (see Fig. 4c, 4f, 4g), (3) biotite granite (Högberget granite) and microgranitic dykes which display various degrees of phyllic alteration (Fig. 6a–6c, appendix 2), and (4) calc-silicate skarn rocks comprising four sub-types: (1) endoskarn, (2) garnet-pyroxene skarn, (3) pyroxene-scapolite skarn and (4) wollastonite skarn (Fig. 8b–8e, respectively and appendix 2).

(1) endoskarn (~20 vol.% of the skarn (based on drill-core logging); Fig. 8b) occurs in the country rock, as thin (<1–3 m) horizons, in close relationship with the main skarn assemblages and pegmatites. The main mineralogy consists of quartz, plagioclase, hornblende and calcite with variable amounts of fluorite, scheelite, molybdenum and sulfides. The unit is strongly sericitized, suggesting phyllic alteration.

(2) the garnet-pyroxene skarn (Fig. 8c) accounts as the most abundant skarn type (~40 vol.% of the skarn (based on drill-core logging)). The matrix is massive with a granoblastic texture and mainly consists of garnet, pyroxene, fluorite, quartz and calcite. Scheelite, sulfides and molybdenum mainly associates with the retrograde phase which cross-cuts the matrix and disassociates minerals (e.g. garnet) at contact.

(3) the pyroxene-scapolite skarn (Fig. 8d) accounts for ~35 vol.% of the skarn (based on drill-core logging) and display a patchy granoblastic texture of pyroxene, scapolite and fluorite. Fluorite, quartz, calcite associates with the accessory minerals; scheelite, sulfides and

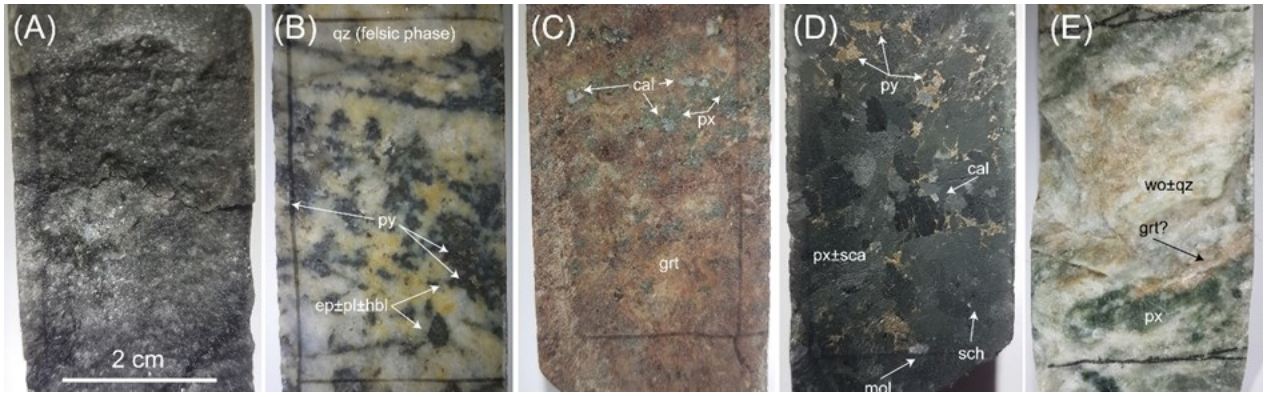

Fig. 8. Main litholigie examples within the Wigström deposit. 8a: Country rock. 8b: Endoskarn, a mixture of quartz, calcite and fluorite with subordinate portions of extensivly altered country rock, pyroxene, garnet, plagioclase, hornblende, sulfides (e.g. pyrite), molybdenum and scheelite. 8c: Garnet-pyroxene skarn with subordinate portions of quartz and calcite. 8d: Pyroxene-scapolite skarn with subordinate portions of calcite, pyroxene, sulfides (e.g. pyrite), molybdenum and scheelite. 8e: Wollastonite skarn with subordinate portions of quartz, pyroxene and garnet.

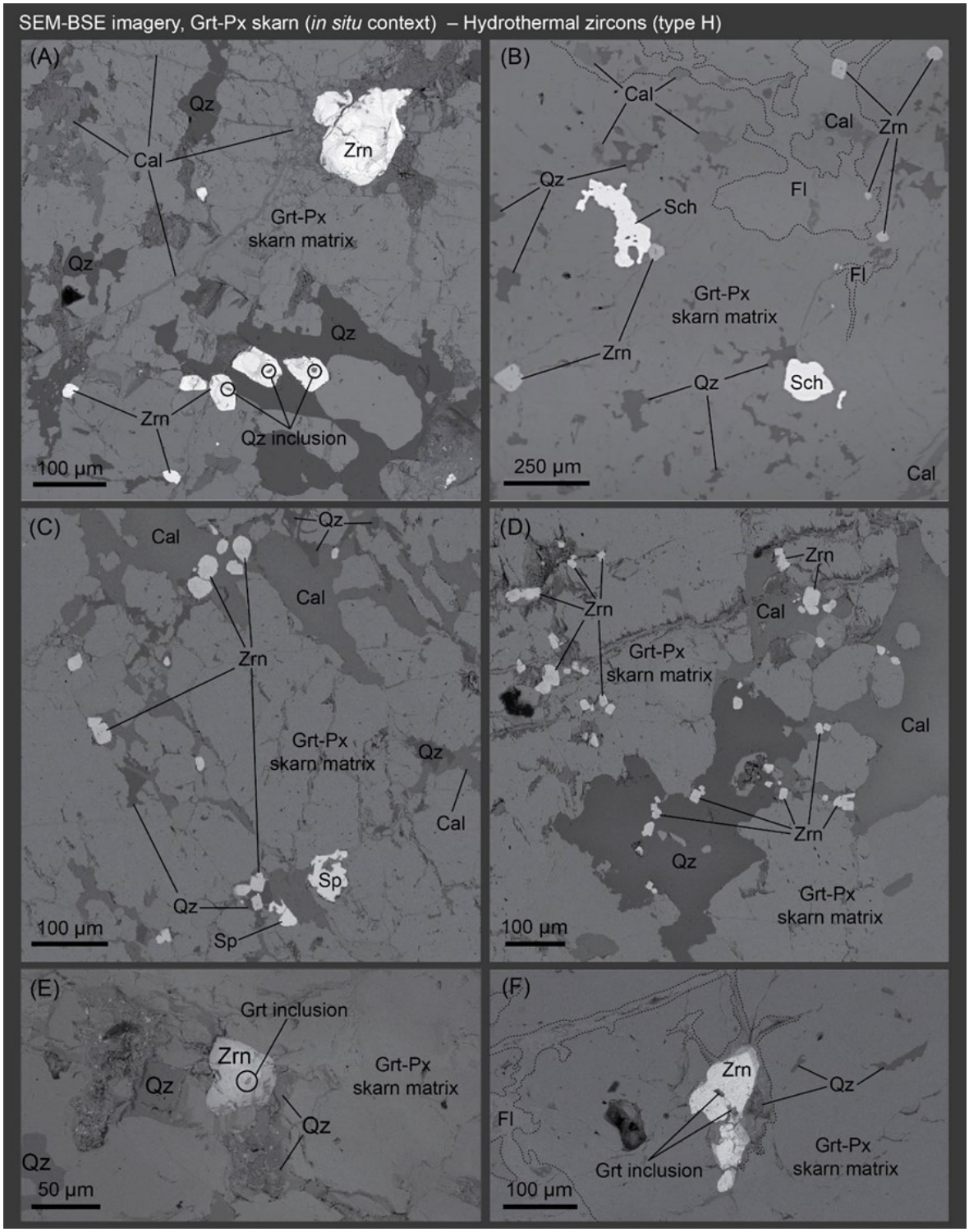

Fig. 9. Example of garnet-pyroxene skarn-hosted zircons and their petrological context, note that zircons always associates with the retrograde phase i.e. quartz and/or calcite and/or fluorite and zircon inclusions consists of mainly quartz, garnet. 9a: Zircons occurs here as an isolated grains and as clusters within quartz. 9b: Isolated zircons and scheelite in association with fluorite, calcite and quartz. One scheelite grain are intergrown with zircon. 9c: Clusters of garnet mainly occurring in veinlets of calcite. Note that sphalerite and zircon occurs paragenetically. 9d: Densely stacked zircon clusters in quartz and calcite veinlets. 9e: Garnet inclusion rich zircon, occurring as an isolated grain within quartz. 9f: Garnet inclusion rich irregular zircon, occurring as an isolated grain in association with fluorite and quartz.

molybdenum. Sulfides can locally be abundant, occurring as disseminated network between gauge crystals.

(4) Subordinate wollastonite skarn (~5 vol.% of the skarn (based on drill-core logging); Fig. 8e) occurs as <2 m horizon within the country rock, and occurs just before and/or after the main skarn units in drill cores (appendix 2). The mineralogy consists of wollastonite, quartz and disseminated garnet, and are completely

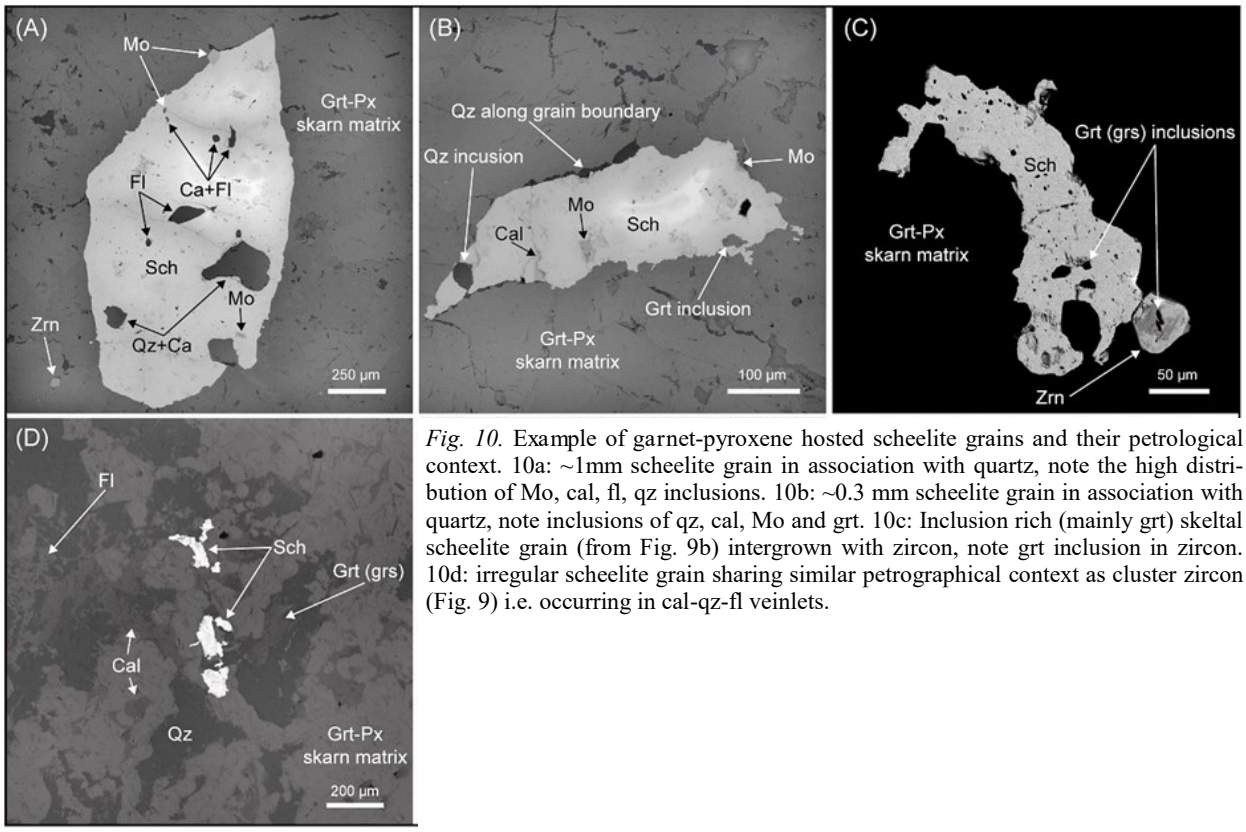

Fig. 10. Example of garnet-pyroxene hosted scheelite grains and their petrological context. 10a: ~1mm scheelite grain in association with quartz, note the high distribution of Mo, cal, fl, qz inclusions. 10b: ~0.3 mm scheelite grain in association with quartz, note inclusions of qz, cal, Mo and grt. 10c: Inclusion rich (mainly grt) skeltal scheelite grain (from Fig. 9b) intergrown with zircon, note grt inclusion in zircon. 10d: irregular scheelite grain sharing similar petrographical context as cluster zircon (Fig. 9) i.e. occurring in cal-qz-fl veinlets.

barren of fluorite, sulfides and ore minerals.

Based on UV-C light fluorescence, scheelite is typically associated with garnet-pyroxene-, pyroxene-scapolite- and endoskarn (appendix 2). Locally, violet fluorite constitutes a major part of the skarn matrix together with quartz and calcite, i.e. the retrograde phase, which occasionally can constitute up to 40 vol.% of a sample, and share the same aforementioned skarn affiliations (appendix 2), similar to the observation at the skarn horizon-wall (chapter 2.3). Molybdenite occurs as small (<2 mm) disseminated grains mainly in endo- and pyroxene-scapolite skarn (appendix 2). Other sulfides (e.g. chalcopyrite and pyrite) occur in endo-, garnet-pyroxene- and pyroxene-scapolite skarn (appendix 2) and are generally associated with retrograde phase accession, but are also present in granite and the country rock which is however uncommon and mainly dependent on the degree of phyllic alteration. Wollastonite skarn appears to be completely barren of scheelite (appendix 2).

Based on SEM-analyses, the mineralogy of the prograde stage consists of garnet and pyroxene as intergrown assemblages, which locally occupy approximate 60–90 vol. % (Fig. 9a–9f), accommodating slightly greater amounts of garnet over pyroxene on average. The retrograde stage consists of quartz, calcite and fluorite which accommodate many of the Wigström skarns ore and other minerals e.g. scheelite, zircon, sphalerite, chalcopyrite, pyrite, molybdenite (Fig. 9a–9f). This retrograde mineral assemblage mainly occurs as veinlets (similar to previous observations) which cross-cuts the matrix and/or as cavities-, pore-filling and/or interstitial between gauge (Fig. 9ab–9f). Zircons are recurrently encompassed by quartz or calcite and often appears in clusters (Fig. 9a–9d), while other zircon in the skarn regularly occurs as isolated grains within the skarn matrix (Fig. 9b–9f), but always associates with retrograde minerals (i.e. quartz, calcite and fluorite) and contains skarn prograde (e.g. garnet) inclusions (Fig. 9a–9f) and skarn retrograde (sulfides) inclusion (Fig. 12). Scheelite grains are disseminated within assemblage and mainly occurs as cavities and/or as pore-fillings (Fig. 10a–10c), but also within quartzitic veinlets similar to zircons (Fig. 10d). Scheelite occurs as elongated anhedral and/or ovoid subhedral crystals with sizes between ~20–300 µm. Inclusions of garnet, quartz, calcite and fluorite occurs frequently in scheelite. Scheelite and zircon can occur as intergrowth (Fig. 10c). Molybdenite inclusions are also present in some scheelite grains and are mostly confined to the crystal grain boundaries (Fig. 10a, 10b). Hand specimens under UV-C light fluorescence in white-yellow to blue, whereas a yellow(ish) fluorescence implies the presence of the calcium molybdate powellite ($CaMoO_4$) in solid solution with scheelite (Hsu & Galli 1973 and the reference therein), as observed in SEM imaging (as Mo-inclusions: Fig. 10a and 10b).

4.2 Zircon characterization

Zircons characterization from granite samples

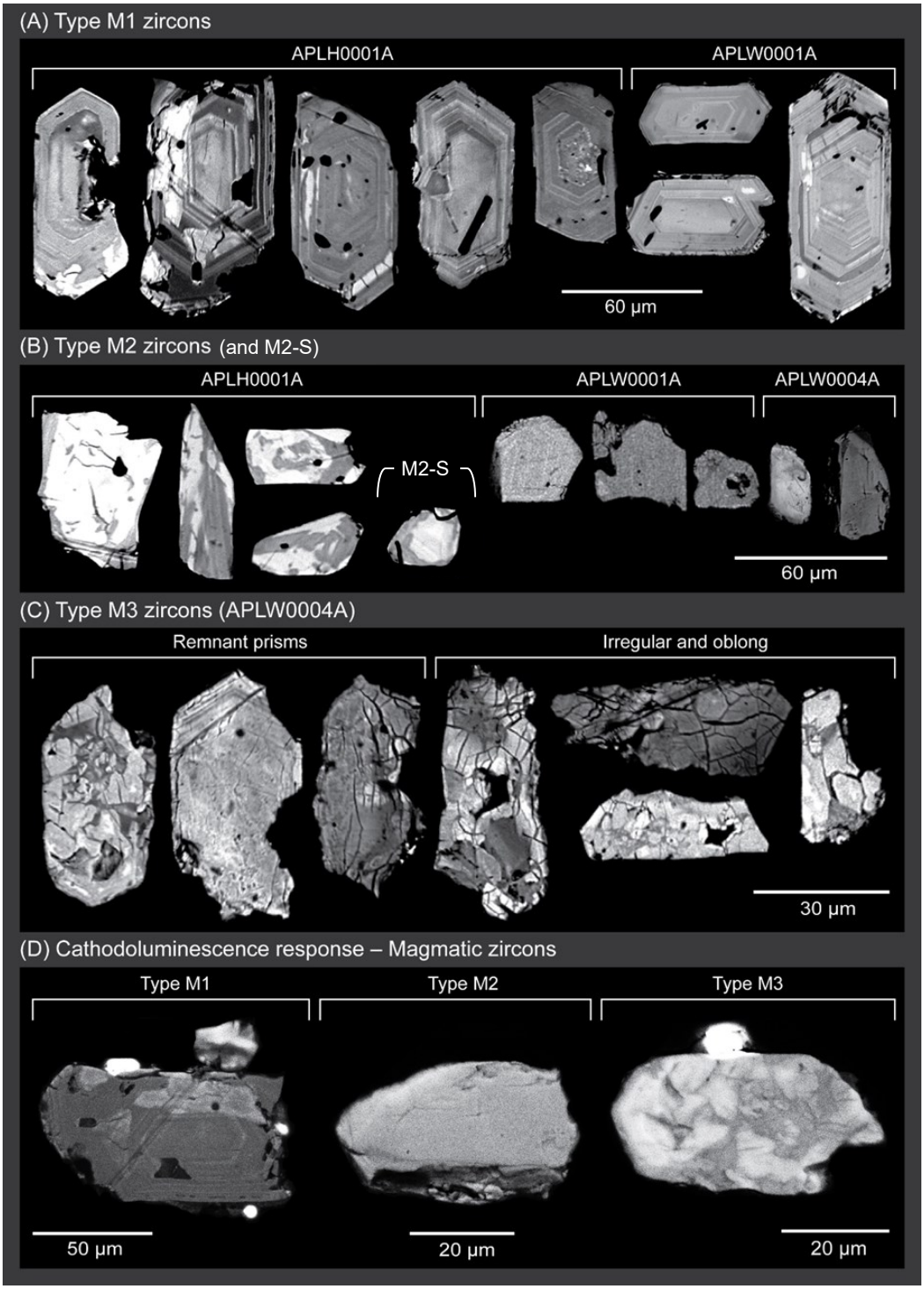

Fig. 11. Examples of representative granite-hosted zircons (Type M) for the three respective localities. 11a: Type M1 zircons, having typical prismatic shapes and internally has oscillatory zonations, due note the high degree of inclusions, fractures and bright BSE areas. 11b: Type M2 and M2-S (in APLH0001A only). Inclusions are lesser compared to M1, interior texture are ambiguous and patchy to featureless. 11c: Type M3 zircons are heavily altered/reworked with high degrees of fractures, inclusions and spongey textures. Their shape is either quasi-prismatic (remnant prisms) or irregularly oblong. 11d: Representative cathodoluminescence response for Type M zircons.

APLH0001A, APLW0001A and APLW0004A was performed on mineral separates only, thus disregarding any petrological context. Thick-section studies performed on zircons hosted within garnet-pyroxene skarn (samples 8B1, APW1A, APW1A1) have documented the petrological context in addition to zircon morphology. From the six granite and skarn samples, five different zircon types have been identified based on variation of morphology and geochemistry. Four types are of magmatic origin (granite-hosted), denoted here as *type M*. Based on morphology and internal textures further sub-divisions of type M zircons have been

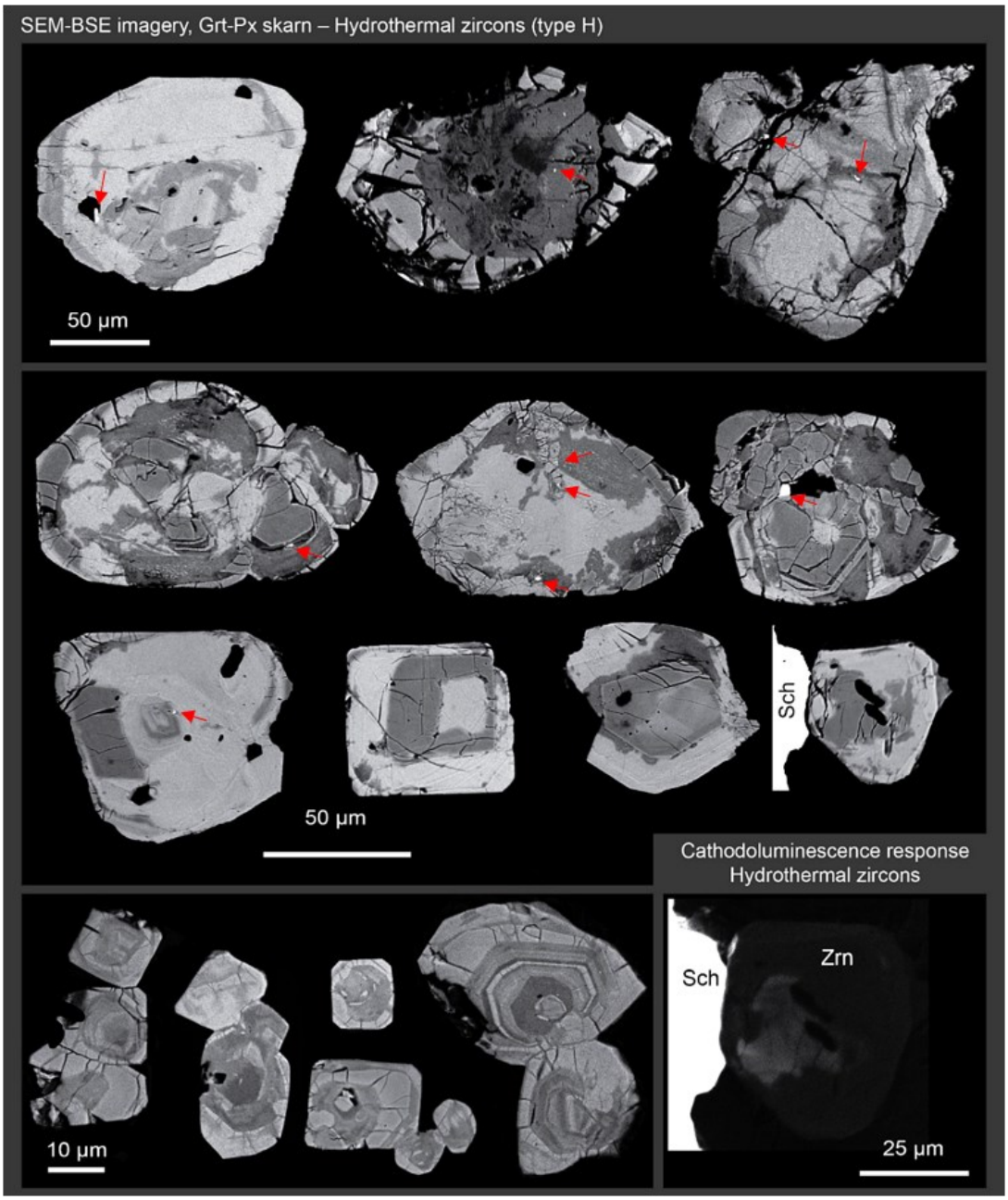

Fig. 12. Examples of representative garnet-pyroxene skarn-hosted zircons (Type H). Note that the grains have mainly a patchy interior of mottled and dark areas to brighter areas, radiant fractures are common, inclusions are mainly garnet (dark inclusions) and sulfides (red arrows). Some zircons from clusters (Fig. 9a, 9c, 9d) consists of bead zircons (crystals stacked onto another) and can have zonation pattern. Note the faint cathodoluminescence response.

made, denoted as types *M1*, *M2*, *M2-S* and *M3* (see below). The fifth zircon type, denoted as *type H*, are interpreted to be of hydrothermal origin. Further discussion of zircons respective origin is presented in the discussion chapter (chapter 5).

4.2.1 Type M1 – granite-hosted zircon (APLH0001A, APLW0001A)

Type M1 zircons range from 25 to 120 µm (60–100 µm are the common range) along the c-axis, and have an aspect ratio (length/width) of ~1.5:1 to 3:1 (Fig. 11a). In general, they are grey, pale brown and pale yellow with a cloudy- and almost opaque interior, however a minority of the population is colourless with a semi-clear interior. A distinguishable feature of type M1 zircons is their elongated euhedral to subhedral prismatic form (Fig. 11a), which typically give a bright cathodoluminescence response (Fig. 10d). Internally, M1 zircons display well developed core- and rim domains with the cores displaying dark to medium grey responses in BSE images. Rim domains comprise densely stacked consecutive oscillatory zoning from core to rim (Fig. 11a). In rare occasions, oscillatory zoning is disrupted by internal boundaries which ter-

minate the zonation pattern and leaving a homogenous broad BSE area (Fig. 11a). Indication of alteration and dissolution are apparent, as bright BSE patches (<20 µm) are irregularly dispersed and/or occur along grain boundaries. Fractures and inclusions (<30 µm, e.g. apatite) occur frequently and occasionally associates with local micro-scale recrystallization within rim domains (Fig. 11a). A minority of M1 zircons display bright BSE widely-spaced rims, which from the core are fractured in a radiant manner (Fig. 11a).

4.2.2 Type M2 and M2-S – granite-hosted zircon (APLH0001A, APLW0001A and APLW0004A)

Type M2 and M2-S zircons range between 20 and 70 µm along their longest axis with aspect ratios of ~1:1 to 2.5:1 (Fig. 11b). Crystal morphologies vary from elongated, ovoid, spherical to fragmental-like. Internally, rim- and core domains are indistinguishable (Fig. 11b). The grains either produce BSE dark contrast (Fig. 11b; sample APLW0001A, APLW0004A) or contrasting bright white and dark BSE patches (Fig. 11b; sample APLH0001A). For the latter, the bright BSE patches dominate, occupying up to 95% of the grains interior and are irregularly dispersed (Fig. 11b). All grains have brighter cathodoluminescence responses (Fig. 11d). Relative to type M1 zircons, fractures and inclusions are less common. A sub-set of M2 zircons, denoted as type M2-S, are recognized in sample APLH0001A have a more spherical crystal form (Fig. 11b). These grains constitute the smallest fraction of the sample i.e. 20–30 µm and display generally display ovoid morphologies (Fig. 11b). Internally, M2-S zircons are similar to M2 zircons and show either contrasting dark to light patches or are dark in BSE images. However, fractures are common which can crosscut the entire crystal (Fig. 11b), and further variation include geochemistry (chapter 4.3, 4.4.).

4.2.3 Type M3 – granite-hosted zircons (APLW0004A)

Type M3 zircons are brown, dark grey to opaque with a murky interior. They range in size from 20 to 60 µm, have aspect ratios of ~1:1 to 2.5:1 and are elongated prismatic or irregular crystals (Fig. 11c). Five grains display remnant prismatic morphologies comparable with type M1 zircons (Fig. 11c). Cathodoluminescence responses are varying but similar to type M1 and type M2 zircons (Fig. 11d). The interior textures of M3 zircons are somewhat ambiguous, lacking coherent core- rim domains, and consists of chaotic mosaic aggregates of contrasting BSE-patches (Fig. 11c). A minority of grains gave a homogenous, dark BSE response with both faint and small bright BSE-patches. Fractures, inclusions, cavities, micro-pores and spongy -textures are common (Fig. 11c).

4.2.4 Type H – Skarn-hosted zircons (8B1, APLW1A, APLW1A1)

Type H zircons are highly complex with variations in size, morphology and internal textures (Fig. 12). Commonly, they lack a distinct prismatic form and range from anhedral to subhedral with irregular, oblong, ovoid, rectangular to skeletal morphologies, and occur as isolated grains or as clusters in or in contact with quartz and/or calcite and/or fluorite. Crystal size ranges from 10 to 200 µm and their aspect ratios range from ~1:1 to 4:1. The CL response is weak to none (Fig. 12). Main features of Type H zircons share similarities with Type M3: irregularly shaped crystals, and interiors comprising aggregates of contrasting BSE signals. Other zircon variation exists and have dark BSE cores with faint-, broad- or patchy zonings, followed by a homogenous concentric zone of zircon outgrowth with bright BSE-intensity, which accommodates faint parallel zonings (Fig. 12). Boundary zones are generally fractured in a radiating manner (Fig. 12). Dark BSE areas are common features and generally propagate inwards from grain boundaries and/or are frequently associated with fractures and/or inclusions. These dark areas are defined by their mottled appearances with dendritic-like textures. Micropores and spongey textures are common and exist in both dark and bright BSE-domains. Skarn prograde minerals (e.g. garnet) and retrograde stage mineralogy (e.g. quartz, calcite, fluorite, sulfides) are present as inclusions in all grains and are erratically dispersed (e.g. Fig. 9e, 9f).

4.3 Zircon REE geochemistry

The results of zircon REE analyses are presented in table 2 (appendix 3). Zircon REE abundances with anomalously high or low values are considered to represent analytical artefacts thus rejected. Three analyses from APLH0001A and one analyses from APLW0004A have been omitted due to these factors but are presented in table 2 (appendix 3).

CI-chondrite normalized plots for Type M zircons show characteristic patterns for magmatic zircons (Fig. 13a–13c) such as inclined positive slopes due to HREE enrichment relative to LREE, positive Ce and negative Eu anomalies (e.g. Hinton & Upton 1991; Hoskin & Schaltegger 2003). Individual analyses of all samples exhibit parallel to sub-parallel patterns (Fig. 13a–13c), whereas ΣREE abundances vary and range between 686–14625 ppm, and Ce and Eu anomalies range between 1.066–16.68 and 0.08–0.61, respectively (table 2 in appendix 3). C1-chondrite normalized plots for Type H zircon have convex patterns with varying positive to negative Ce and Eu anomalies, and are relatively depleted of LREE and HREE (Fig. 13d–13f). The ΣREE varies largely and range between 122–33229 ppm, and Ce and Eu anomalies

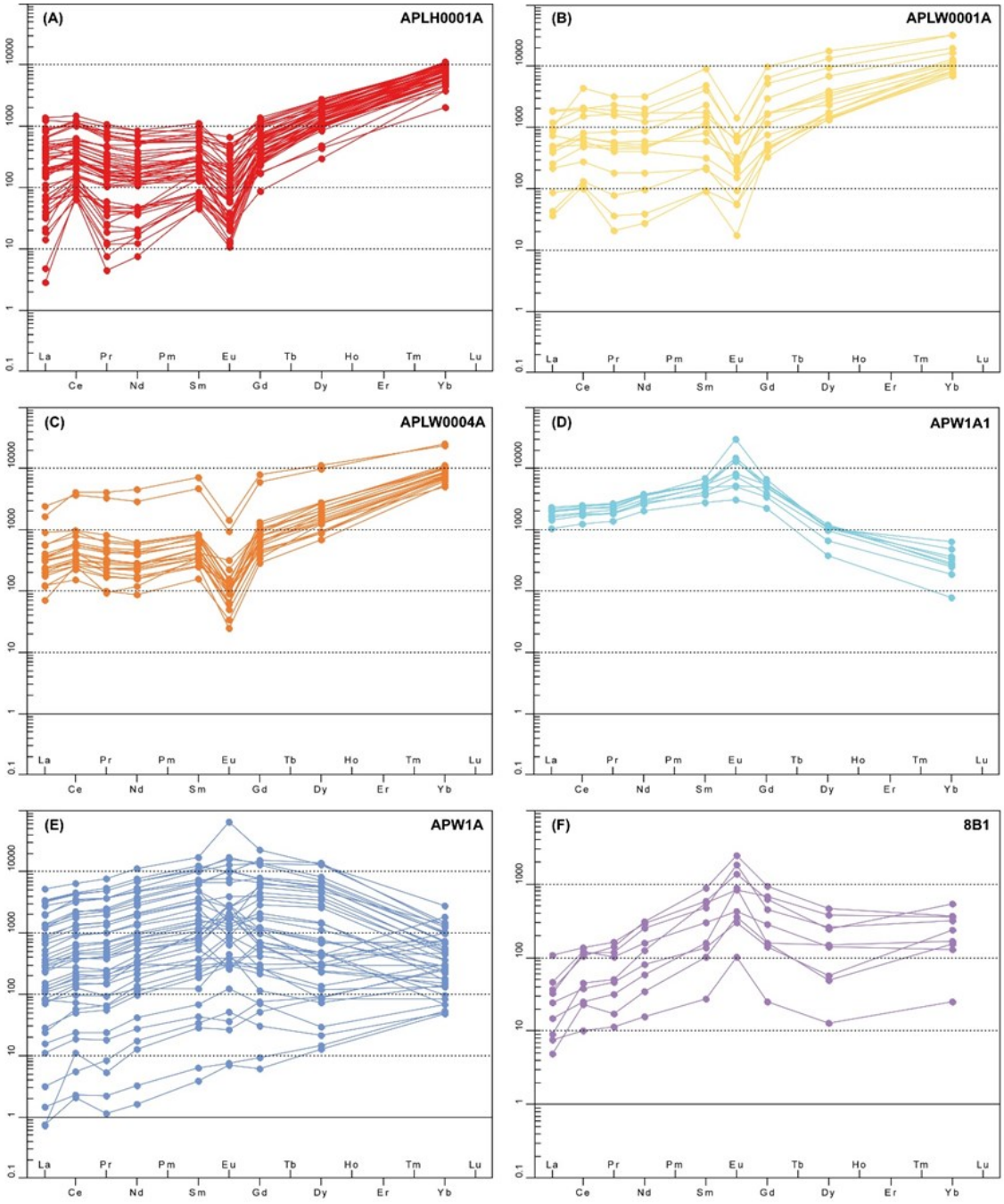

Fig. 13. C1-chondrite normalized spidergrams for each locality. 13a–13c: Type M zircons. 13d–13f: Type H zircons. Note the main differences between Type M and Type H zircons, Type M have convex pattern and distinct negative Ce and positive Eu spikes, Type H have convex patterns with, mainly, flatter negative Ce and positive Eu spikes.

range between 1.01–5.64 and 0.26–5.51, respectively (table 2 in appendix 3). The degree of REE fractionations and oxygen fugacity differ between the granite-hosted and the skarn-hosted zircons (Fig. 14a–14e) and further distinguish the two zircon populations (Type M and Type H) apart. For Type M zircons REE fractionation ratios range from: $(La/Yb)_n$:0.0004–0.2262, $(Sm/La)_n$: 0.2726–28.7877, $(Gd/Yb)_n$: 0-0226–0.3854, and for Type H zircons the ratios range from: $(La/Yb)_n$: 0.0027–13.2155, $(Sm/La)_n$: 1.0598–61.1005, $(Gd/Yb)_n$: 0.1248–28.764 (table 2 in appendix 3, Fig. 15a–15d).

4.4 Zircon U-Pb geochronology

U-Pb zircon data are listed in table 3 (appendix 4). The geochronology results (Concordia plots) are here presented as separate free regressions of uncorrected data and common lead corrected (PbC) for each locality (Fig. 15–18). Analyses that are between 95–105% concordant at the upper intercept have been used to calculate a weighted mean age.

4.4.1 Granite hosted zircons

4.4.1.1 Högberget granite (sample APLH0001A)

A total of 45 LA-ICPMS analyses on 33 zircon grains

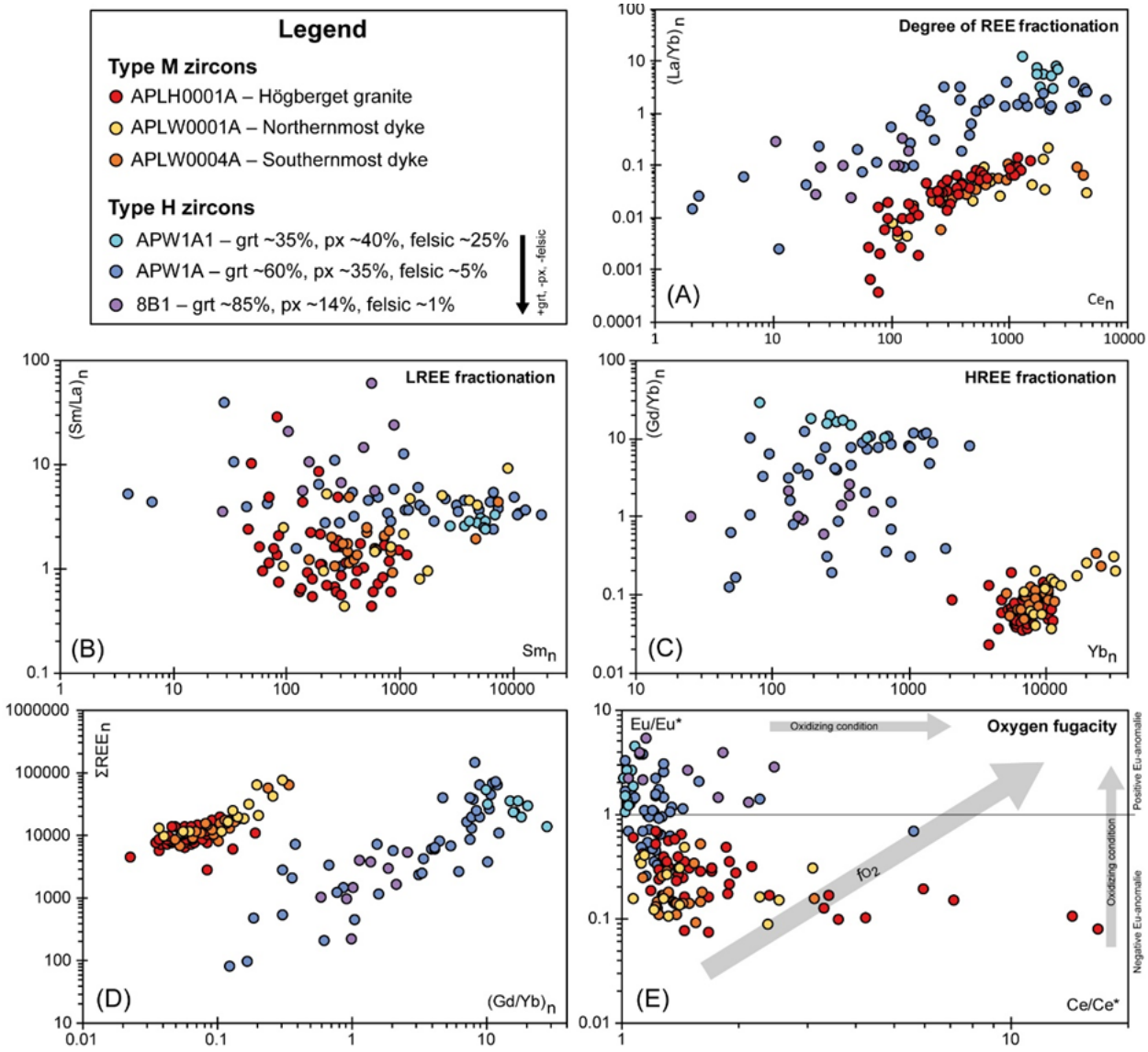

Fig. 14. Selection of bivariate diagrams plots for Type M and Type H zircons, note that the respective zircon type deviates from each other. Subscript of "n" indicate C1-normalized values, respective ratios are listed in table 2 (appendix 3). 14a–14c: degree of REE, LREE and HREE fractionation. 14d: total REE fractionation against HREE fractionation. 14e: Oxygen fugacity diagram, Eu/Eu* and Ce/Ce* ratios are listed in table 2 (appendix 3).

from Högberget granite were performed. 22 are of Type M1, six are of Type M2 and the remaining five are of Type M2-S zircons. Overall, the analytical spots yielded high Pb, U and Th contents ranging from 86 to 2460 ppm (avg. = 560 ppm), 234 to 11 520 ppm (avg. = 5810 ppm) and from 96 to 7290 ppm (avg. = 3023 ppm), respectively (table 3 in appendix 4). Th/U ratios vary from 0.125 to 0.837 (avg. = 0.509; table 3 in appendix 4). For the PbC signatures, $^{206}Pb/^{204}Pb$ ratios range from 197 to 16412 (avg. = 6785) and ^{204}Pb counts per seconds (CPS) range from 66 to 5880 (avg. = 704; table 3 in appendix 4). Type M2 zircon have the lowest U and Th content, and range between: U: 234–3000 ppm and Th: 96–1900 ppm (table 3 in appendix 4), while Type M1 zircons range between: U: 3260–11520 ppm and Th: 1460–7000 ppm (table 3 in appendix 4). Type M2-S zircons have a U and Th range similar to Type M1; U: 1660–11200 ppm and Th: 890–6310 ppm (table 3 in appendix 4).

On the Concordia diagrams (Fig. 15a, 15b), two analyses plot concordant, H2-1 and H2-13 (Type M2 zircons) with $^{207}Pb/^{206}Pb$ uncorrected ages of 1864±35 Ma and 1854±13Ma respectively, and has $^{207}Pb/^{206}Pb$ PbC-corrected ages of 1804±69 Ma and 1835±19 Ma, respectively (table 3 in appendix 4). Uncorrected data yields upper and lower intercept ages of 1829±57 Ma and 366±47 Ma (MSWD 63.0, n = 45), respectively (Fig. 15a), with an age distribution from 633±30 Ma to 2202±67 Ma (table 3 in appendix 4). PbC-corrected data yields an upper intercept of 1778±22 Ma and a lower intercept age of 414±17 Ma (MSWD 10.2, n = 45), respectively (Fig. 15b), with an age distribution from 518±42 Ma to 1835±19 Ma (table 3 in appendix 4). The two concordant analyses produce an uncorrec-

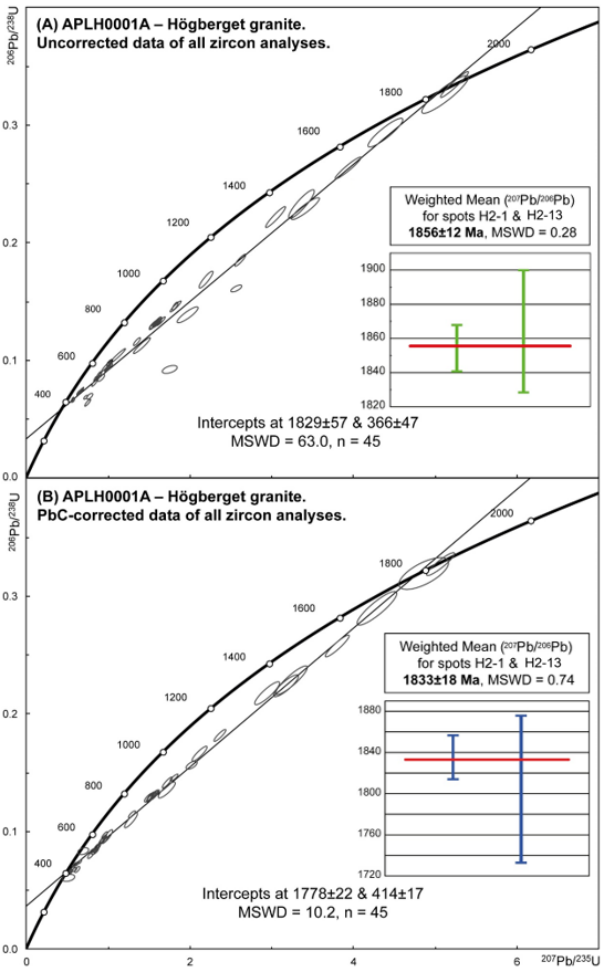

Fig. 15. a: Concordia diagram, uncorrected data. b: Concordia diagram, PbC-corrected data. The weighted mean age consists of the two concordant (95–105% concordant) analyses.

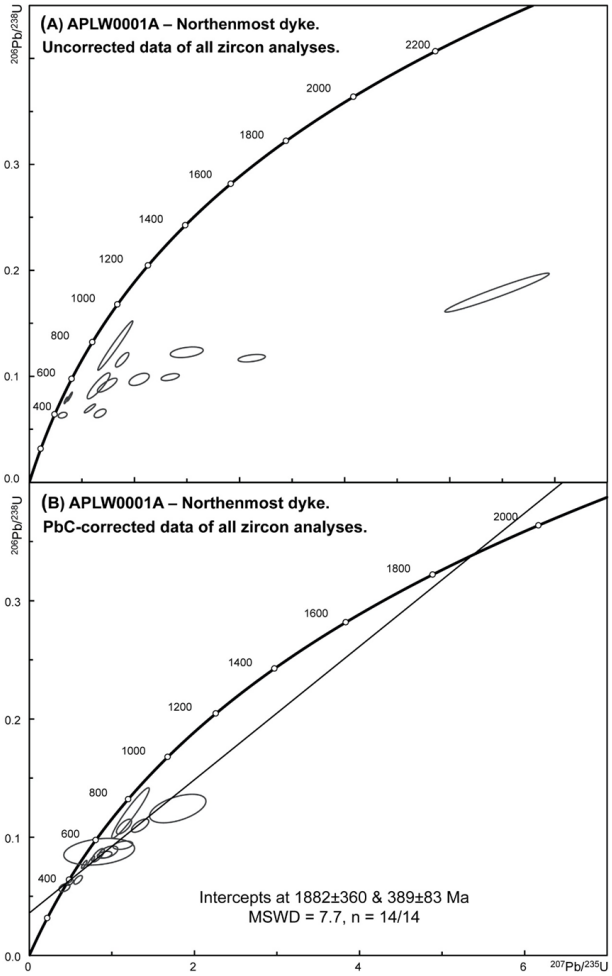

Fig. 16. a: Concordia diagram, uncorrected data. b: Concordia diagram, PbC-corrected data.

ted weighted mean age of 1856±12 (MSWD 0.28, Fig. 15a) and PbC-corrected data yields a weighted mean age of 1833±18 Ma (MSWD 0.74, Fig. 15a).

4.4.1.2 Northern microgranite dyke (sample APLW0001A)

A total of 13 zircon grains yielded 14 LA-ICPMS analyses from the northernmost dyke. 11 of these zircons are of Type M1 and the remaining 3 are of Type M2. Overall, the analytical spots yielded exceedingly high Pb, U and Th concentrations ranging from 355 to 1996 ppm (avg. = 1050 ppm), 3580 to 16 360 ppm (avg. = 8751 ppm) and from 2920 to 8520 ppm (avg. = 4694 ppm), respectively (table 3 in appendix 4). Th/U ratios range from 0.339 to 1.036 (avg. = 0.568; table 3 in appendix 4). For the PbC signatures, $^{206}Pb/^{204}Pb$ ratios range from 54 to 18 899 (avg. = 1856) and the ^{204}Pb CPS range from 139 to 43 100 (avg. = 13919; table 3 in appendix 4).

Data plot extremely discordantly for both uncorrected- and PbC-corrected data (Fig. 16a, 16b). Ages based upon uncorrected data obtain a variety of implausible ages ranging from 784±42 to 3752±35 Ma (table 3 in appendix 4). The age distribution for PbC-corrected data are more geologically realistic and range from 367±263 to 1714±245 Ma (table 3 in appendix 4). Isoplot was unable to produce calculated intercept ages for the uncorrected data due to the severe scatter (Fig. 16a). However, in PbC-corrected data, intercepts were obtained, yielding upper- and lower intercept ages of 1882±360 Ma and 389±83 Ma, respectively (MSWD = 7.7, n = 14; Fig. 16b). As the analyses are far from the upper intercept (severely discordant) the upper intercept age should be treated with caution.

4.4.1.3 Southern microgranite dyke (sample APLW0004A)

A total of 22 LA-ICPMS analyses on 21 zircon grains from the southernmost microgranite dyke was performed. Two of these zircons are of type M2 and the remaining 20 are of type M3. Zircon U and Th concentrations are approximately within the same range as sample APLH0001A with U ranging from 381 to 11110 ppm (avg. = 4399 ppm) and Th ranging from 184 to 8280 ppm (avg. = 2101 ppm; table 3 in appen-

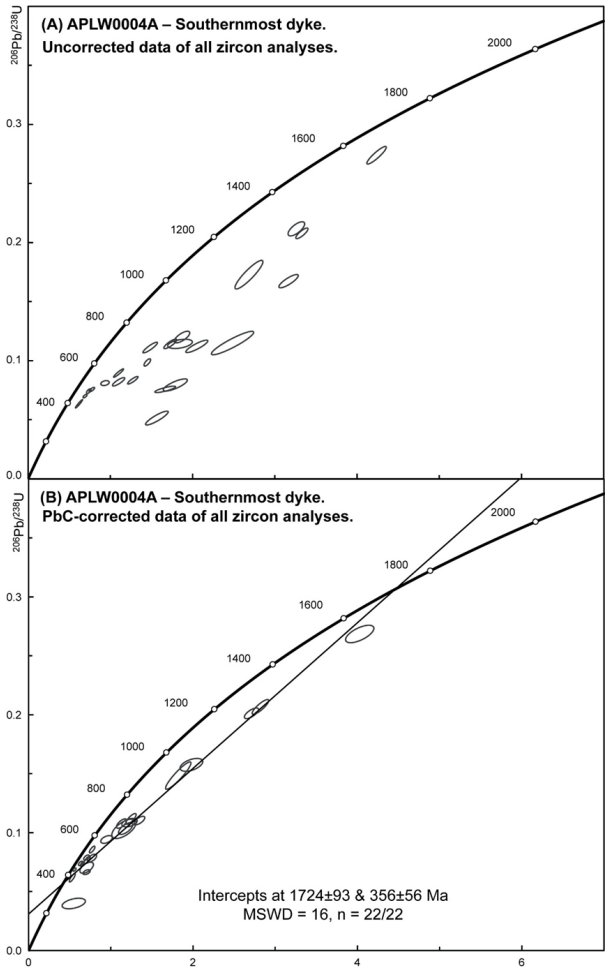

Fig. 17. a: Concordia diagram, uncorrected data. b: Concordia diagram, PbC-corrected data.

dix 4). Pb concentrations are relatively low and range from 117 to 873 ppm (avg. = 444 ppm). Corresponding zircon Th/U ratios vary from 0.080 to 1.308 (avg. = 0.459 ppm; table 3 in appendix 4). For the PbC signatures, $^{206}Pb/^{204}Pb$ ratios range from 151 to 5042 (avg. = 901) and the ^{204}Pb CPS range from 71 to 9740 (avg. = 2851; table 3 in appendix 4).

As with sample APLW0001A, the zircon population for APLW0004A are severely discordant on a Wetherill Concordia plot for both uncorrected- and PbC-corrected data (Fig. 17a, 17b) with intercept ages ranging from 949±38 to 2492±69 Ma and from 571±48 to 1779 Ma, respectively. For the uncorrected data, Isoplot was unable to produce intercepts and calculate ages due to the severe analytical scattered (Fig. 17a). The scatter becomes lesser in PbC-corrected data, but mainly clustering towards the lower intercept, but with a few ellipses closer towards the upper intercept (Fig. 17b). The regression line produces upper- and lower intercept age of 1724±93 Ma and 356±56 Ma (MSWD = 16, n = 22), respectively (Fig. 17b). Similar to APLW0001A U-Pb analyses, the analyses plot far from the upper intercept, and thus the upper intercept age should also be treated with caution.

4.4.2 Skarn hosted zircons (Samples APW1A1, APW1A and 8B1)

In total, 31 Type H zircon analyses were made on the three skarn samples, these comprised one analysis from APW1A1, 22 analyses from APW1A and 8 analyses from 8B1. Compared to Type M zircons, analyses of the Type H zircons yielded relatively low Pb, U and Th concentrations ranging from 23 to 1119 (avg. = 324 ppm), 146 to 6170 ppm (avg. = 1402 ppm) and from 2 to 1500 ppm (avg. = 85 ppm), respectively (table 3 in appendix 4). Th/U ratios varies from 0.003 to 0.303 (avg. = 0.038 ppm, table 3 in appendix 4). For the PbC signatures, $^{206}Pb/^{204}Pb$ ratios spans from 93 to 38 700 000 (avg. = 3 092 043) and the ^{204}Pb CPS are below the detection limit (b.d) to 2360 (avg. = 212; table 3 in appendix 4).

For the uncorrected data, ages ranging from 1331±36 to 3259±41 Ma (table 3 in appendix 4; spot 8B1-2 (~3.2 Ga) were excluded from figure 18a and from age calculation in figure 18b due to the large error limits) and produced upper and lower intercept ages of 1724±49 Ma and 359±150 Ma, respectively (MSWD = 94.0, n = *31*; Fig. 18a). Seven analyses are concordant (table 3 in appendix 4; Fig. 19a) at the upper intercept (Fig. 18b), these analyses achieve a weighted mean age of 1771±31 Ma (MSWD 13.0), a lower MSWD (2.0) and a weighted mean age of 1795±20 Ma is achieved by selecting analyses with the four oldest ages (table 3 in appendix 4). For the PbC-corrected data, ages range from 1202±47 to 1864±206 Ma (table 3 in appendix 4) and they yielded upper and lower intercept ages of 1709±54 Ma and 403±150 Ma (MSWD = 39.0, n = 31), respectively (Fig. 18b). Six analyses are concordant (table 3 in appendix 4) at the upper intercept (Fig. 18b), these analyses achieve a weighted mean age of 1762±35 Ma (MSWD 10.8), a lower MSWD (0.62) and a weighted mean age of 1784±10 Ma is achieved for the same four analyses as above (table 3 in appendix 4; Fig. 18b).

5 Discussion

5.1 Timing of intrusion, skarn mineralization and Pb loss

The age constrains in this study yields relatively poor results with low statistically robustness due to high degree of discordance and few concordant analyses. For example, Analyses from the granitic dykes (samples APLW0001A and APLW0004A; table 3 in appendix 4, Fig. 16a–17b) show a severe degree of discordance and mainly plots around to the lower intercept. In uncorrected data for the 2 dykes (Fig. 16a, 17a) age calculations were unattainable due to lacking concordant analyses and the severe analytical spread. In PbC-corrected data, ages were attained (Fig. 16b,

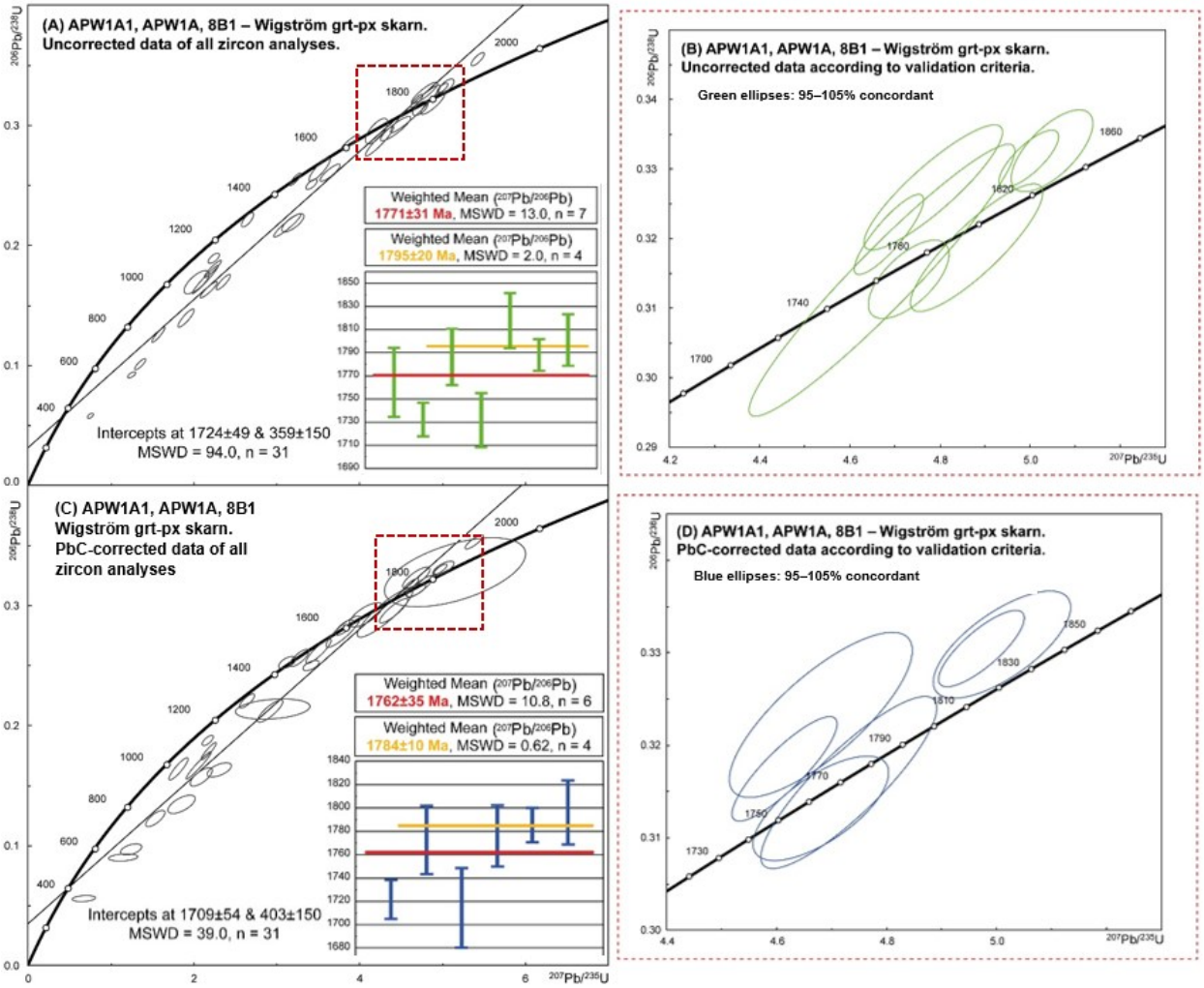

Fig. 18. a: Concordia diagram, uncorrected data. b: Seven analyses that are 95–105 concordant (uncorrected data) and are included in the weighted mean age calculation (inset in Fig. 18a). c: Concordia diagram, PbC-corrected data. d: Six analyses that are 95–105 concordant and are included in the weighted mean age calculation (inset in Fig. 18c).

17b), but the upper intercepts are considerate to be imprecise due to the low degree of concordance which makes precise constrains harder for upper intercepts (Fig. 16b, 17b). Thus the geochronological results from the dykes are interpreted to present no geological meaning regarding their emplacement age (i.e. upper intercepts). The high degree of discordance present within the dykes are regarded to be the result of metamictization, as many of the zircons in this study are highly enriched in U and Th (table 3 in appendix 4). In zircon U-Pb geochronology, metamictization via self irradiation is the resultant of internal α-decay bombardment during the natural decay chain of U and Th to Pb (Krogh & Davis 1975). With time, the deterioration will alter or damage the crystal structure causing cell-swelling and eventual fracturing the crystal in a radiating manor. These fractures likely provides structural pathways for Pb leaching, inducing episodic Pb-loss which typically cause isotopic disturbances, and in return can give high degrees of discordance in zircon U-Pb analyses (e.g. Mezger & Krogstad 1997). Further, this effect will be elevated for U-enriched zircons, as bombardment from α-particles are amplified (Silver 1991; Horie et al. 2006). As seen within all raw discordias (Fig. 15a–18b), metamictization is present for many of the analyses as they fall below the concordia, and therefore demonstrates that Pb loss have occurred (at various degrees) within the Wigström-Högberget area.

Although a precise emplacement age of the dykes is unattainable from the data, the lower intercept of the dykes can provide geological significant, as these intercepts can indicate a time of a geological event that promoted initial Pb-loss. In Bergslagen, Larson and Tullborg (1998) argued that Pb-mobilization could have been induced in the upper Paleozoic via extensional erosion covers (~3 km thick) derived from the Caledonides erosion front. Högdahl et al. (2001) study also suggest that the Caledonian orogeny could have induced extensive fluid flow causing Pb mobility at ~385 Ma, and also concluded that Pb-loss would be more apparent in metamict, high U and Th Paleoproterozoic zircons within the Fennoscandian shield. These remarks coincide with

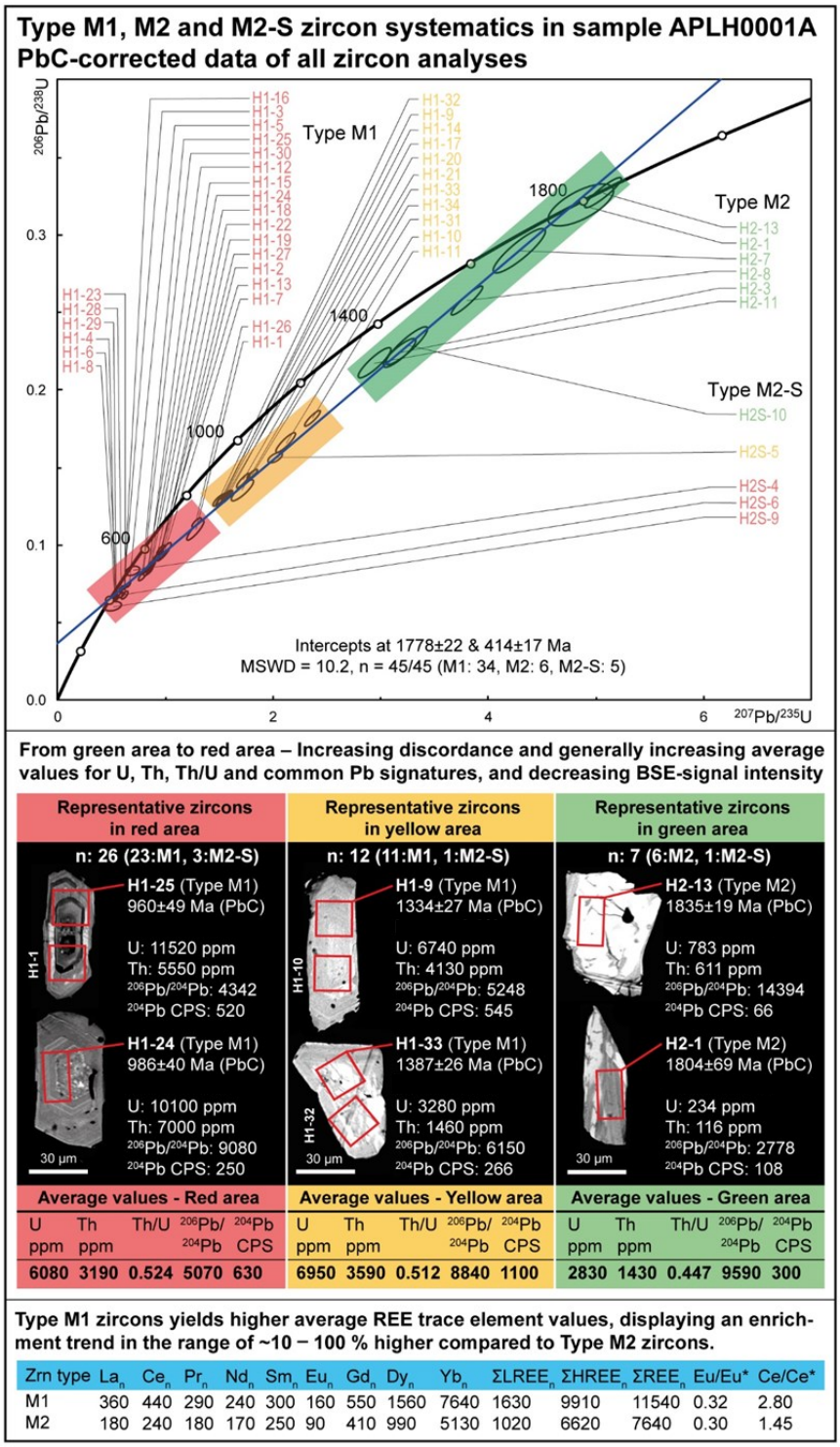

Zrn type	La_n	Ce_n	Pr_n	Nd_n	Sm_n	Eu_n	Gd_n	Dy_n	Yb_n	ΣLREE$_n$	ΣHREE$_n$	ΣREE$_n$	Eu/Eu*	Ce/Ce*
M1	360	440	290	240	300	160	550	1560	7640	1630	9910	11540	0.32	2.80
M2	180	240	180	170	250	90	410	990	5130	1020	6620	7640	0.30	1.45

Fig. 19. Zircon systematic of the Högberget granite. Emphasising the correlation between discordance and larger trends for U, Th, Th/U, PbC signatures and REE. Discordance and these trends also correlates with zircon sub-classes i.e. Type M1 and M2-S zircons plots further down the discordia (red and yellow group) compared to Type M2 zircons (green group). Enrichment trends

the lower intercepts of the dykes: 389±83 Ma for and 356±56 Ma, and thus supports Pb mobility and loss around the upper Paleozoic within the Bergslagen region.

Zircon U-Pb data for the Högberget granite yields two concordant analyses (Fig. 15), where the weighted mean ages are regarded as the best interpretation for the emplacement age (Fig. 15b). For the Högberget granite, PbC-corrected data align spots closer to the discordia (Fig 15b compared to 15a), demonstrating that PbC correction in this case is favoured over uncorrected data. Therefore, the weighted mean age of 1833±14 Ma is regarded as the best constrain for the emplacement age of the Högberget

granite.

Regarding Pb loss for the Högberget granite. As previously discussed, Bergslagen zircons with high U and Th has presumably experienced Pb loss as the result of metamictization, whereas Pb mobilisation occurred at ~380 Ma. Within the Högberget granite three sub-classes of zircons have been assign: Type M1, M2-S and M2 (chapter 4.2). These sub-classes share a systematic in correlation with U, Th, Th/U ratio, common Pb signatures, Ce/Ce*, Eu/Eu* and REE enrichments against the degree of discordancy (i.e. metamictization; table 2 in appendix 3 and table 3 in appendix 4). Type M1 magmatic zircons in the Högberget granite represent the highest degree of discordance (table 3 in appendix 4, Fig. 15), and have the largest enrichments of U, Th and common Pb signatures (table 3 in appendix 4), and generally incorporate more REEs compared to least discordant zircon sub-class, Type M2 (table 2 in appendix 3). Within the Concordia space the coincidence is clear, as analyses with elevated U, Th, Th/U values, common Pb signatures, REE enrichments and oxygen fugacity (Ce/Ce* and Eu/Eu*) are placed further down along the Discordia (see Fig. 19 and inset tables). Based on these systematic arrangements, analyses can be divided into three groups: green-, yellow- and red group (Fig. 19). The red group consists of ~95% Type M1 zircons (n = 23) and ~5% Type M2-S zircons (n = 3) which together show the highest degree of discordancy (Fig. 19), with radiogenic element ranges (table 3 in appendix 4, Fig. 19) between: U: 1660–11520 ppm (avg. = 6080 ppm), Th: 890–7000 ppm (avg. = 3190 ppm), $^{206}Pb/^{204}Pb$ ratio: 197–11039 (avg. = 5070) and ^{204}Pb CPS: 115–5880 (avg. = 630 CPS). The yellow area consists of ~95% Type M1 zircons (n = 11) and ~5% Type M2-S (n = 1) zircons, yielding slightly less discordance (Fig. 19). For data in the yellow array, the elemental and isotopic ratio values (table 3 in appendix 4, Fig. 19) are similar to those of the red group: U: from 3280–10650 ppm (avg. = 6950 ppm), Th: 1460–7290 ppm (avg. = 3590 ppm), $^{206}Pb/^{204}Pb$ ratio: 636–36412 (avg. = 8840) and ^{204}Pb CPS: 105–4870 (avg. = 1100 CPS). The least discordant analyses are found in the green area (Fig. 19), consisting of ~85% Type M2 zircons (n = 6) and ~15% Type M2-S (n = 1). The elemental and isotopic ratio values (table 3 in appendix 4, Fig. 19) ranges from: U: 234–11200 ppm (avg. = 2830 ppm), Th: 96–6310 ppm (avg. = 1430 ppm), $^{206}Pb/^{204}Pb$ ratio: 3399–17065 (avg. = 9590) and ^{204}Pb CPS: 66–1150 CPS (avg. = 300 CPS). Noteworthy, the high values in the green area belongs to H2S-10, a Type M2-S zircon (table 3 in appendix 4, Fig. 19). Overall, Type M1 zircons yield an average REE enrichment of ~10–100%, compared Type M2 (Fig. 19 inset table). As for timing of Pb loss, by plotting the Type M sub-classes as separate sets—variable free regression upper intercept ages are achieved: 1659±31 Ma (Type M1), 1752±140 Ma (Type M2-S) and 1823±50 Ma (Type M2) (Fig. 20). The resultant of these intercept variances is however not an indication of a diverse zircon population, but are an outcome of difficulties to constrain linearity i.e. making intercepts more imprecise the further away the least discordant spots is from the concordia intersect (e.g. Demirer 2012), similar to the Högberget dykes (as discussed). Consequentially, highly discordant analyses (i.e. red and light green discordia in Fig. 21) provides better constrains for the lower intercept, i.e. initial Pb-loss (e.g. Schoene 2014), as seen with Type M1 (384±13 Ma) and Type M2-S (386±97 Ma) (Fig. 20), which shares similar lower intercepts as the two dykes (Fig. 16a, 17b) and supports the argument of Pb mobilisation in Bergslagen during the upper Paleozoic (Larson & Tullborg 1998; Högdahl et al. 2001). The Type M2 constrains the upper intercept better (Fig. 20) compare to Type M2 and M2-S, but with a deviating constrain for the lower intercept (609±200 Ma). As demonstrated, Pb loss (lower intercepts) are interpreted to have occurred around ~380 Ma for the Högberget granite as well.

Zircons from the Wigström garnet-pyroxene skarn (samples APW1A1, APW1A and 8B1) yields similar weighted mean ages for both datasets (Fig. 18a, 18b), 1795±20 (MSWD 2.0, uncorrected data) and 1784±10 Ma (MSWD 0.62, PbC-corrected data), and the MSWD values are both around 1 (statistically robust). This could be a consequence of relatively lower degree of metamictization and Pb loss for the skarn hosted zircons compared to the granite hosted zircons. Type H zircon also has severely lower U, Th, Th/U ratio and PbC signatures compared to Type M1 and M2-S zircons (table 3 in appendix 4) and in return could therefore have experienced minor metamictization relative to Type M1 and M2-S zircons. Therefore, the uncorrected data are favoured as PbC corrections, in this case, could lead to analytical overcompensation. The age with an MSWD close to 1 are in favour (i.e. weighted mean age of the four oldest ages). Thus, an age of 1795±20 Ma is regarded as the best interpretation for the Wigström deposit. Regardless which dataset that are favoured, within the error limits both datasets points towards an age of ~1790 Ma for the Wigström deposit.

The age of the Högberget granite are constrained from two analyses and can therefore be considered to lack statistical robustness. However, the age of the granite and the mineralization overlaps within the error, i.e. 1833±14 Ma for the granite and 1795±20 Ma for the mineralization. Overall, the granite age constrains in this study points toward and older emplacement age of the Högberget granite then the previous study: 1750±10 Ma (Bergman et al. 1995), and the mineralization achieves an age similar to previous studies,

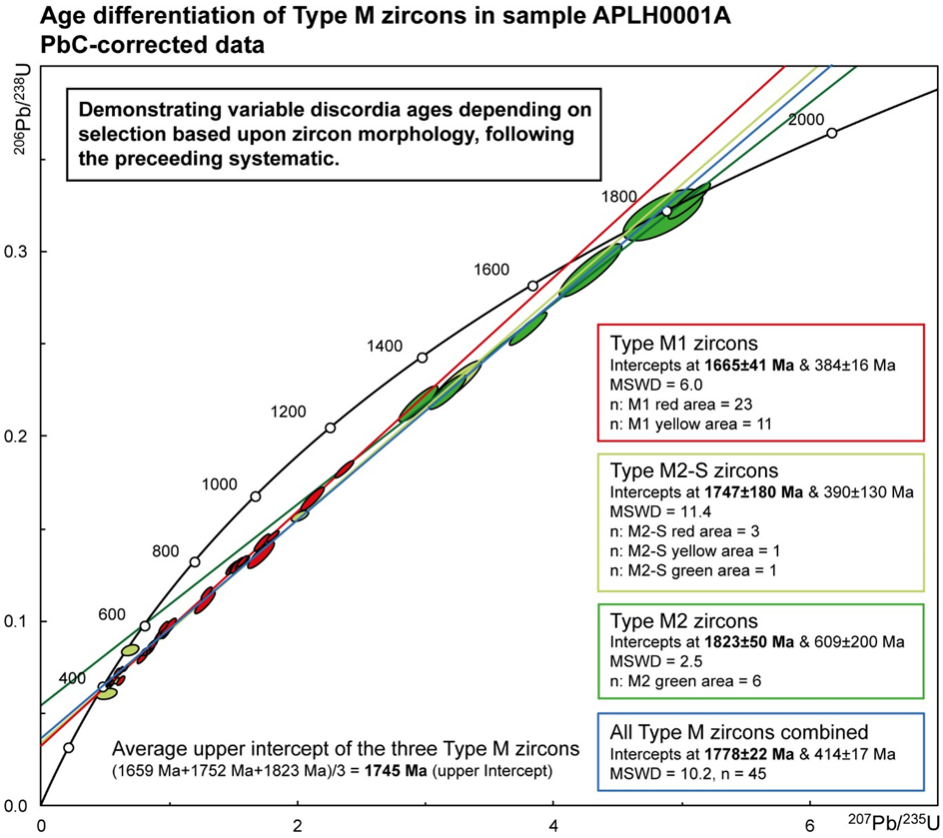

Fig. 20. Demonstrating variable ages given by free regression of the different Type M zircon sub-classes. The result of lower and upper intercept along the concordia varies and are the result of difficulty in linear constraints i.e. analyses closer (Type M1 (red line and box) and M2-S (light green line and box)) to the lower intercepts constrains the lower intercept (i.e. timing of Pb-loss) more precise compared to the upper intercept (i.e. emplacement age). The upper intercepts are best constrained with concordant analyses (Type M2 zircons, dark green line and box) but constrain the lower intercept imprecise.

~1.8 Ga (Stein et al. 1996; Sundblad et al. 1996). Generally, this further supports a ~1.8 Ga age for the Bergslagen W-Mo metallogenesis (e.g. Romer & Öhlander 1994; Stein et al. 1996; Sundblad et al. 1996; Lynch et al. 2019).

5.1.1 Age constrain by forced regression

In other geochronological studies (e.g. French & Heaman 2010; Demirer 2012), anchoring of the lower intercept to a known geological events (e.g. tectonothermal, hydrothermal) responsible for Pb loss has proven useful for better age constrains of discordant data. Forcing regression thru lower intercepts can accordingly circumvent errors represented by discordant data, and therefore in the Högberget case can produce a compliment age from more analyses compare to the weighted mean age (constrained by two analysis). As indicated by results from the lower intercept from the Högberget granite (384±13 Ma Type M1, 386±97 Ma Type M2-S), the two dykes (389±83, 356±56 Ma) and the Wigström deposit (359±150 Ma) (chapter 4.2), Pb loss seems to have occurred around 380 Ma within the Wigström-Högberget area (chapter 5.1), and these results are in agreement with other studies e.g. Larson & Tullborg (1998) and Högdahl (2001; lower intercept = 384±15 Ma) around the Fennoscandian shield. Further, the most recent geochronological study on W-Mo granites in Bergslagen by Lynch et al. (2019) also yield a similar lower intercepts: 387±23 Ma. This further supports Pb loss at ~380 Ma within Bergslagen. A calculated average lower intercept age of 381±62 Ma is achieved from the of previously mentioned studies and from this study (see above). Anchoring the lower intercept to 381±62 Ma and forcing regression thru the least discordant analyses of the Högberget granite: H2-1, H2-10, H2-11, H2-13, H2-3, H2-7and H2-8 (assigned to the green group in the zircon systematic, Fig. 19) yields an upper intercept of 1796±47 Ma (MSWD = 7.3) for the Högberget granite. This age coincides with the age achieved for the Wigström deposit (1795±20 Ma). However, analytical overdispersion are here larger (MSWD = 7.3) compared to the weighted mean age, MSWD (0.74), of the granite, but this further fortifies relations between the granite and the mineralization, and thus strengthen the W-Mo metal logenesis to ~1.8 Ga in Bergslagen, as previously discussed.

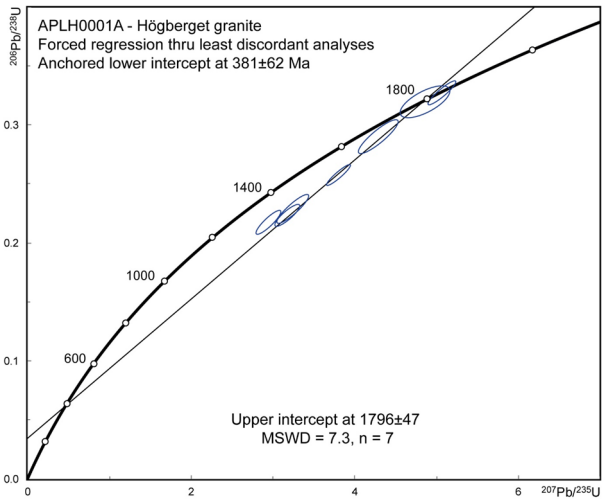

Fig. 21. Redefined age of Högberget granite, when forcing regression thru the least discordant analyses (green group Fig. 19) and anchoring the lower intercept to 381 Ma (time of initial Pb loss, average age as calculated).

5.2 Zircon genesis and the controlling factors of zircon geochemistry at the Wigström-Högberget area

Zircon grains from the Wigström skarn (Type H) and Högberget granite (Type M, with their respective subclasses) are distinguishable based on their geological settings (chapter 2.2 and 2.3) and respective petrographical and geochemical properties (chapter 4.3), and discrepancies further includes morphology, interior texture and features (chapter 4.2), cathodoluminescence response (chapter 4.2), paragenetic relationship (Type H only; chapter 4.1) and isotopic signatures (chapter 4.4). These variances points towards different origin. Plotting average C1-normalized REE of all samples on a spidergram the main-classes (Type M & H) revels their distinct differences geochemically (Fig. 22)—concave pattern for Type H zircons and convex pattern for Type M zircons. Further, Eu-anomalies and HREE fractionation also vary, Type H are depleted with a negative dip (Fig. 22 and high Gd/Yb ratio, Fig. 14c, 14d) compared to type M which are heavily enriched with a rising dip (Fig. 22 and low Gd/Yb ratio, Fig. 14c, 14d). Type M zircons have HREE patterns typical of unaltered magmatic zircons, which generally have a range between 10^3x and 10^4x chondrite (Hoskin & Schaltegger 2003). In contrast, the Type H zircons show declining HREE patterns (Fig. 22) which could possibly be a result of the "garnet effect". This effect can cause preferential partitioning of HREE into garnets (Rubatto 2002; Chen et al. 2010; Rubatto 2017), hence sequestering the limited REE budget within the skarn assemblages leading to HREE-depleted zircons. This suggests HREE were initially consumed by garnet during a skarn prograde-stage, and zircon that formed at a later stage (retrograde, Type H) consumed the remaining amounts of HREE—leading to depletion.

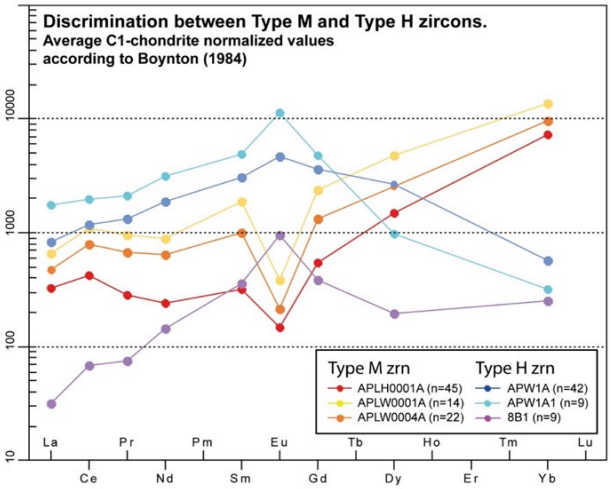

Fig. 22. Average C1-normalized spidergram plots of Type M and Type H zircons

In unaltered magmatic zircons, a positive Ce-anomaly and a negative Eu-anomaly is expected, which is the case for Type M zircons, and are commonly attributed to oxygen fugacity (Hoskin & Schaltegger 2003 and the reference therein). However, Eu-anomalies may also be attributed to the presence of feldspars (e.g. plagioclase) which can consume large amount of Eu, resulting in typical negative Eu-depletions for granitic hosted zircons (Hoskin & Schaltegger 2003 and the reference therein). The positive Eu-anomaly of the Type H zircons could therefore be a function of both oxygen fugacity and the absence of feldspar within the garnet-pyroxene skarn assemblage—or together, the result as a function of proximity to a local growth media (e.g. plagioclase) during zircon nucleation, e.g. proximal zircon to feldspar achieves Eu-depletion and proximal zircon to garnet achieves HREE depletion.

The Type M zircon population from the Högberget granite generally display typical traits and geochemical characteristics (Fig. 22) of magmatic zircons (e.g. Hoskin & Schaltegger 2003 and the references therein): e.g. average size along the c-axis is ~70 µm and range from subhedral to euhedral prisms with pyramidal terminations, a crystal aspect ratio (L/W) of 2:1–3:1, oscillatory zonation predominate the interior texture (Fig. 11), REE signatures includes e.g. inclination from LREE to HREE in spidergrams ((La<<Yb and $(Gd/Yb)_n$ <1Fig 13a–13c, 21) and in addition a positive Ce-anomaly (Ce/Ce* >1) and a sharp negative Eu-anomaly (Eu/Eu* <1) (Fig. 13a–13c and 22) and an average Th/U ratio of ~0.5 (Fig. 19). These signatures undoubtedly support that Type M zircons are of magmatic origin. However, compared to "typical" magmatic zircons in litterature (e.g. Hoskin & Schaltegger 2003), Type M zircons have about ten-times more LREEs then avrage granite-hosted zircons and also have lagre amouts of U and Th (Fig. 19). As

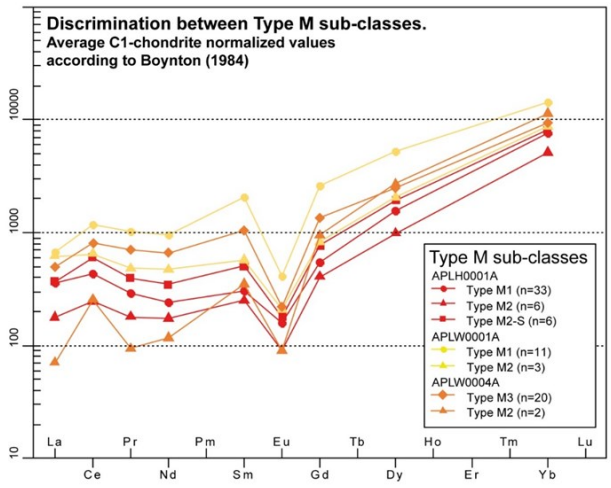

Fig. 23. Highlighting the relative REE enrichments of Type M zircon sub-classes. Type M2 have lower values compared to Type M1, M2-S and M3 zircons. These REE trends correlates with high U, Th, Th/U and PbC signature according to the zircon systematic (Fig. 19)

previously discussed, U, Th, REE and especially LREE enrichments are a typical feature of GP suite-related granites (Stephens et al. 2009). Previous work has also shown that metamict zircons can become enriched in REE and especially LREE (Mathieu et al. 2001; Geisler et al. 2003) compared to non-metamict zircon. These REE incorporations have been interpret to be the result of a complex substitution chains during Pb-loss induces by metamictization (Horie et al. 2006), whereas non-formula element (Ca, Mn, Al and Fe) substituted for Zr and Si and in return REE could then substitute with Ca and Mn. This complex series of substitutions could perhaps explain the REE enrichment of the Högberget granite, as the preceding zircon systematic correlates with REE enrichments, discordancy and high U and Th values (Fig. 19). The systematic of REE enrichment and zircon sub-classes (Type M1, M2-S, M2 and M3), which further correlates with U and Th enrichments are also valid for all three granite localities (APLH0001A, ALPW0001A, APLW0004A, table 2 in appendix 3 and table 3 in appendix 4). By plotting REE average values for the different Type M zircon sub-classes from all samples reveal relatively similar systematic regarding REE enrichment for the high U and Th zircon sub-classes (Type M1, M2-S and M3; Fig. 23). Overall, Type M zircons have here similar normalized REE patterns over each of the three samples, although Type M1 and M2-S zircons have higher ΣREE abundances compared to Type M2 variants. These trends may reflect the result of metamictization as previously discussed—where progressive deterioration of the zircon crystal structures could have promoted alteration (e.g. Pidgeon et al. 1966) and the incorporation of REEs, preferentially LREEs, and other non-formula elements (e.g. Ca) into the crystal lattice during annealing (e.g. Mathieu et al. 2001; Geisler et al. 2003; Horie et al. 2006). Whereas U-enriched zircons (Type M1, M2-S and M3) that experienced severer metamictization resulted in heavily intake of REE during annealing compared to low U-bearing zircons (Type M2), which only has suffered minor metamictization and in return gained a lower REE intake.

A hydrothermal origin is regarded for Type H zircon and are here discussed. Zirconium has long been regarded as an immobile element, but numerous report during the past three decades contains zircons interpreted as of hydrothermal origin (e.g. e.g. Rubin et al. 1989; Kerrich & King 1993; Hoskin 2005; Yang et al. 2013). As demonstrated by Rubin et al. (1993), Zr and other incompatible elements (e.g U, Th, REE, Mo) can be mobilized in hydrothermal system, allowing precipitation of hydrothermal zircons and ore-minerals in equilibrium. This relationship between hydrothermal zircons and ore depositions has been utilized to date timing of mineralization in both W (Wang et al. 2016), Fe (Xiaodong et al. 2015) and Au deposits (Bao et al. 2014).

To address the origin of Type H zircons, three potential sources are proposed: (i) zircons inherited from Svecofennian supracrustal units, (ii) transportation of magmatic zircons via ore-bearing fluid exsolution, and (iii) Zr was mobile and able to be precipitated as zircon from ore-carrying hydrothermal fluids i.e. implying a hydrothermal origin.

(i) In terms of their textures and morphologies, Type H zircons displays chaotic, dendritic and patchy textures (Fig. 11) suggesting relatively intense fluid-mitigated alteration. Inherited grains from the supracrustal unit, such as xenocrystic cores, would indicate U-Pb ages between 1.91–1.88 Ga, however the geochronological data lacks such ages >1.88 Ga (table 3). This suggests zircon inheritance from the supracrustal units likely has not occured.

(ii) If the Type H zircons were magmatic in origin, REE patterns similar to Type M zircons may be expected (Fig. 21). The different average C1-normalized values for Type M and Type H zircons suggest their mode of crystallization varied. For example, Type M zircons typically show concave patterns with positive Ce-anomalies, moderate negative Eu-anomalies and high degrees of HREE enrichment (Fig. 21). In contrast, Type H zircons have convex patterns with flat to faintly positive Ce-anomalies, distinct positive Eu-anomalies and a high degree of HREE fractionation (Fig. 21). Bivariate plots also distinguish the two different populationsapart (Fig. 14a–14e). Further, the internal textures of Type H zircons (Fig. 11) are broadly contradictory to archetypal granite-hosted zircons, such as oscillatory zonation patterns and Th/U >0.5 (Hoskin & Schaltegger 2003).

(iii) A hydrothermal origin for Type H zircons is favoured based on the following considerations. As part of the Wigström skarn assemblage has textural relationships suggesting that Zr acted as a mobile agent. Specifically, Type H zircons are intergrown with or are included by hydrothermal quartz, calcium and/or fluorite i.e. retrograde phase (Fig. 9a–9f, 10c). Scheelite, sphalerite, chalcopyrite, pyrite, molybdenite also share the same paragenesis with the quartz-calcite-fluorite-zircon assemblage (Fig. 9–10). The faint cathodoluminescence response for Type H zircons can also be a result of hydrothermal association, as previous studies suggest this to be the case (c.f. Kozlik et al. 2016; Wang et al. 2016). Also, the paragenetic association of Type H zircons with hydrothermal quartz, calcite and fluorite, and their incorporation of hydrothermal mineral inclusions such as garnet and sulfides (Fig. 9–10) further emphasises their inferred hydrothermal origin (c.f. Schaltegger 2007). The same paragenesis is also shared with scheelite and sphalerite, as scheelite and zircon can occur as intergrown (Fig. 9b, 10c) and together with sphalerite (Fig. 9c), and scheelite also associates with the retrograde phase similar to zircon (Fig. 10). This paragenisis suggest that Type H zircons and scheelite crystallised concurrently, presumably shortly the after skarn formation at a retrograde stage, as suggested by the presence of garnet (from a prograde stage) inclusions (Fig. 9–10) within both zircon and scheelite. Furthermore, it seems plausible that the zircons and scheelite precipitated at a last stage (retrograde) in the skarn evolution (c.f. Meinert et al. 2005), since these phases usually occur as open-space precipitates or are enclosed by paragenetically late hydrothermal quartz-calcite-fluorite veinlets which crosscuts the skarn assemblage. However, the original source of the Zr cannot be quantified. Zirconium could have either derived from hydrothermal fluids of the Högberget and/or by interactions between hydrothermal fluids and the wall rocks, where Zr leached and saturated the fluids. But regardless of the Zr source(s) the Type H zircon is undoubtedly the result of hydrothermal precipitates and thus of hydrothermal origin.

In the literature, several attempts have been made to distinguish magmatic and hydrothermal zircons using geochemistry. Hoskin (2005) created discrimination diagrams for magmatic and hydrothermal zircons based on LREE abundances and the degree of Ce-anomalies: $(Sm/La)_n$ vs. La (ppm) and Ce/Ce* vs. $(Sm/La)_n$, which has been widely used in other studies since then. However, a new study of Zhong et al. (2018) concludes that elevated positive Ce-anomalies and LREE enrichments in zircons can be the results of unintentional and undetected analysis of REE-bearing inclusions such as apatite, titanite, allanite, monazite and xenotime (c.f. Bindeman et al. 2014). As demonstrated by Zhong et al. (2018), such analysed inclusions can severely affect Ce-anomalies and LREE patterns, with nm-scale inclusions (<1 μm) and as little as 0.05 vol % sufficient to affect zircon REE analyses. Thus, Zhong et al. (2018) dispute the validity of zircon source discrimination diagrams (i.e. Hoskins diagrams) as such minute contaminations can be hard to constrain and presumably be undetected in SEM-imagery prior to ablation. In this study, SEM imaging revealed numerous μm-sized inclusions in both Type M1, Type M2-S (e.g. apatite, chapter 4.2) and Type H zircons (e.g. garnet) (Fig. 9–10). These inclusions were carefully avoided during LA-ICPMS analyses. However, the depth of the ablation pit reached ~20 μm, which may have resulted in the inadvertent analysis of nano- to micrometer inclusion with depth. When plotting Type M and Type H data onto Hoskins (2005) discrimination diagrams (Fig. 24), all analyses congregate in and around the hydrothermal field—indicative of high LREE-enrichments and faint Ce-anomalies i.e. implying a hydrothermal origin for both Type M and H. As concluded from the SEM-imagery and isotopic chemistry, Type M zircons are indeed of magmatic origin (chapter 5.2), however in Hoskins discrimination diagram they plot as of hydrothermal origin (Fig. 24), obviously inaccurately. Evidently these observations supports Zhong et al. (2018) remarks. However, REE analyses from other studies of GP suits granites have reached similar results, these REE enrichments trends can therefore be related to the actual chemistry and not to be a result of inadvertent inclusion analyses. Whichever may be the case, the "Hoskins" diagram should be used with cation when dealing with heterogeneous and inclusion-rich zircon populations hosted by Bergslagen GP-suite intrusions, and petrographic contexts may be more useful.

5.3 Episodical zircon formation at the Wigström-Högberget area

The Bergslagen GP-type magmatism peaked during Late Orosirian (~1.8 Ga), and intruded into the ~1.9 Ga metasupracrustal succession. The GP-intrusions occur during two distinct phases: from 1861 to 1830 Ma and from 1825 to 1740 Ma (Stephens et al. 2009 and the references therein), whereas the W-Mo metallogenesis is generally constrained to ~1800 Ma (e.g. Romer & Öhlander 1994; Stein et al. 1996; Sundblad et al. 1996; Lynch et al. 2019). The Type M1 zircons from the Högberget granite crystallised around 1.8 Ga, with large prismatic habits displaying oscillatory zonation (chapter 4.2). Low Zr content (Stephens et al. 2009) within the felsic parental magma likely promoted U and Th incorporation into zircon via Zr substitution, leading to formation of U and Th enriched zircon (Type M1 and M2-S) e.g. up to ~11000 ppm U and ~7000 ppm Th (table 3 in appendix 4). With time,

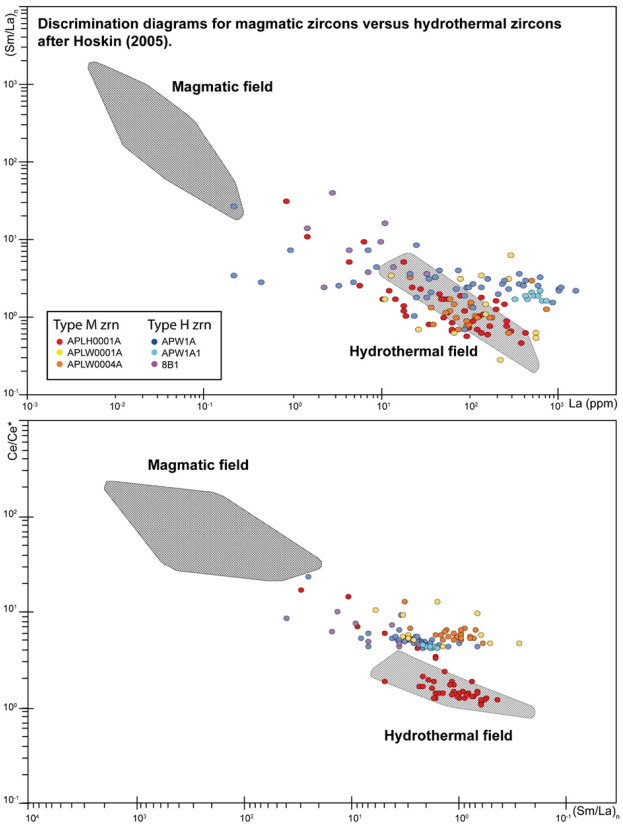

Fig. 23. REE analyses plotted onto the "Hoskin" hydrothermal versus magmatic discrimination diagram (Hoskin 2005). All analyses in this study plots in or around the hydrothermal field. Highlights that caution must be made when using these diagrams to make distinctions between magmatic and hydrothermal zircons.

magmatic differentiation processes would have facilitated the formation of residual melt and fluids within the Högberget magma chamber. Late-stage residual magmatic fluids can mobilize incompatible elements such as REE, U, Th, and Zr, (Rubin et al. 1993; Aja et al. 1995; Yang et al. 2013), particularly if the fluid is saturated with volatiles such as F (Dietrich 1968; Rubin et al. 1989; Keppler 1993; Kovalenko et al. 1995; Salvi & Williams-Jones 2006). As F is also incompatible, the content will thus accumulate with time and partly supress zircon nucleation (Keppler 1993) and thus promote Zr mobility (Dietrich 1968). This together with low Zr content could further explain the zircon scarcity within the Högberget granite. Keiths and Westras (1981) study concludes that F-complexes also aids the enhancement of Mo-concentration within the magma. In Bergslagens this is supported by Baker (1985), which argued that enrichments of W and Mo amongst other incompatible elements are dependent on F-concentration (Baker & Hellingwerf 1988), and Ohlsson (1979) also suggests a correlation between F and W in Bergslagen. From field- (chapter 2.3, 4.1) and drill core (appendix 2) observations and SEM imagery (e.g. Fig. 9), this is as well the case for the Wigström mineralization, as hydrothermal fluorite, quartz and calcite is associated with scheelite (W, Mo), zircon and sphalerite and other sulfides within the skarn assemblage (Fig. 9). As indicated by oxygen fugacity diagram (Fig. 14e) and by the presence of ilmenite (Bergman 1995), the Högberget granite developed under relatively reduced oxidation conditions (c.f. Wei 2018). This could have promoted W and Mo to fractionate into the residual fluids rather than nucleate intragranitic.

Subsequently and during continuing fractionalization, the enriched segregated volatiles would ascent towards the magma chambers apical. The ascending volatile would build up enough pressure towards the cupola to breached the system, discharging off-shoot pegmatites and aplites from the body into the surrounding rocks, conveying associated ore-forming components and Zr. The volatiles would have migrated through the countryrock via pre-existing fabrics (e.g. tectonic foliations and beddings), and eventually forming the cross-cutting dykes at the Wigström deposit, and on smaller scale appearing as infillings within the skarn assemblages i.e. retrograde phase were scheelite and hydrothermal zircon (Type H) precipitated.

The origin of Type M2 zircon can be explained by their shared isotopic and geochemical signature resemblances with the Type H population, i.e. relatively low U, Th, Th/U ratios, and ΣREE (chapter 4.3, 4.4)—this perhaps implies a related origin? The highly evolved nature of the Högberget granite suggests that the rock could represent a late-stage magmatic transition-phase to a hydrothermal system (e.g. Yang et al. 2013). As discussed, granitic derived hydrothermal fluids from the Högberget intrusion are responsible for the Wigström mineralization and as well the origin of the Type H population. Prior to metasomatism and mass-transfer towards the skarn assemblage, these fluids circulated within the magmatic system during a late magmatic stage, and discharge of granitic fluids initialised metasomatism. Perhaps, shortly before and/or during the late stage some portion of the escaping fluids was injected into available pore-space within the granite, whereas zircon nucleation occurred and formed the Type M2 population. This explains the irregular, un-prismatic zircon morphologies of Type M2 (chapter 4.2), which zircon forming in a late magmatic stage tend to obtain (Hoskin & Schaltegger 2003), and also the low U, Th, and ΣREE (especially LREE) concentration (Schaltegger 2007) and low Th/U ratios (chapter 4.3, 4.4), which also acquired for late-stage magmatic zircons (Hoskin & Schaltegger 2003), and could explain these trends. The relative trend of low concentrations of U, Th, and ΣREE is also given by the Type H (chapter 4.3, 4.4), and presumably reflects progressive depletions during fluid- and system transition from a late-stage magmatic system into a

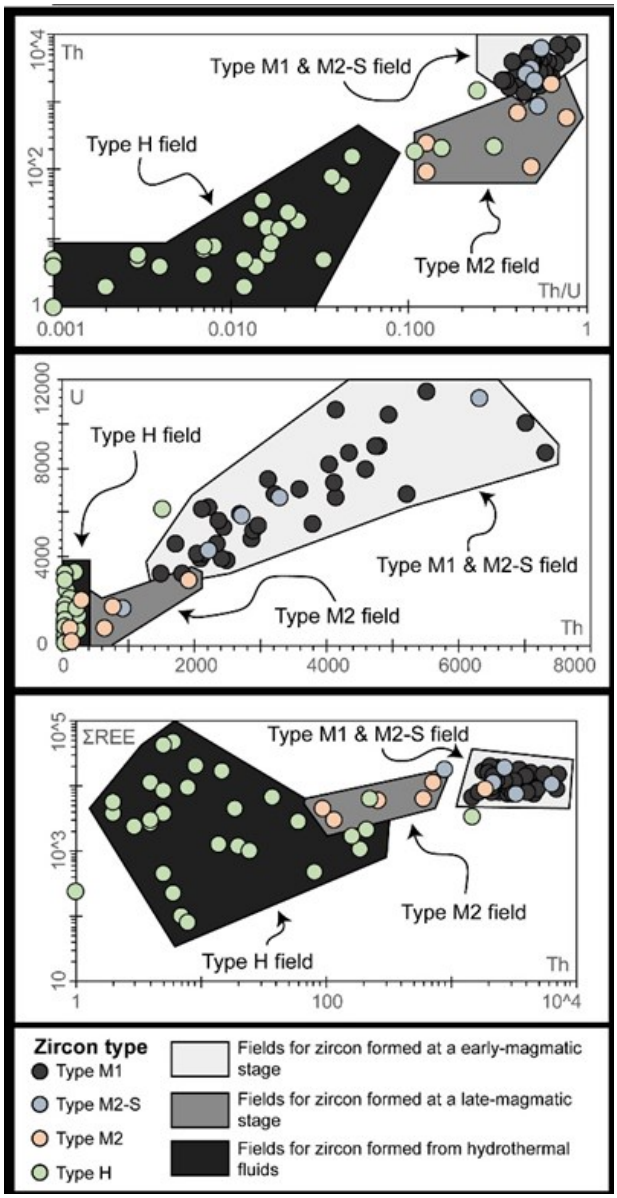

Fig. 24. Discrimination diagram and relative U, Th, Th/U and REE trends for Type M1, M2-S, M2 and H zircons.

hydrothermal system. By plotting Th, U and ΣREE content and lower Th/U ratios onto bivariate diagrams (Fig. 25) further distinguish respective zircon populations (M1, M2-S, M2 and H) apart. These trends are interpreted to corresponds to the fluid evolution responsible for the formation of respective zircon subclasses: fluids from the early-magmatic stages formed Type M1 and M2-S zircons and consumed large portion U, Th and REE (Fig. 24), and residual fluids at a late magmatic-stage are thus relatively depleted of these elements and formed Type M2 zircons (Fig. 24). Further depletion of these trends occurred during mass -transfer onto the Wigström skarn, at the hydrothermal stage. the fluids were severely depleted of U and Th, and formed low U and Th bearing zircons as characterized by the Type H population (Fig. 24, chapter 4.4).

6 Conclusions

To summarize, Type M zircons are of magmatic origin and Type H zircons are of hydrothermal origin. Type M1 zircons formed during an early magmatic stage and Type M2-S represent highly altered and metamict M1 zircons. Type M2 zircons formed during a late magmatic stage prior to hydrothermal system development. Skarn-hosted hydrothermal Type H zircons formed when late-stage granitic fluids transitioned into a hydrothermal system. The obtained ages from Type M and Type H zircons represent the emplacement age of the Högberget granite and to tungsten mineralization within the Wigström skarn, respectively. The revised age of ~1.8 Ga for the Högberget granite further supports a temporally and spatially focused ~1.8 Ga W-F-Mo metallogenic epoch for western Bergslagen.

- Zircon U-Pb LA-ICPMS dating of Type M and Type H zircon populations at the Wigström-Högberget area yields a granitic emplacement age and a mineralization age around 1.8 Ga. Notwithstanding the relatively large age uncertainties (~at the 2σ-level). These two ages together support a ~1.8 Ga for the W-Mo metallogenesis in Bergslagen.
- Magmatic zircons from the Högberget granite and hydrothermal zircons from the Wigström skarn have different REE signatures, distinguishable in REE-normalized spidergrams and bivariate plots. Type M population displays typical patterns for magmatic zircons, apart from high LREE enrichments, while Type H population have a convex pattern with positive Eu-spikes and high degree of LREE and HREE fractionations.
- High contents of U, Th, PbC and REE correlates with U-Pb isotopic discordancy, as apparent from the zircon systematic for the Högberget granite. Two zircon populations of the Högberget granite, Type M1 and Type M2-S compared to M2, have suffered severe metamictization as the result of high U and Th contents, which over time resulted in great α-particle bombardment during radiogenic decay, and rendering the populations discordant. Structural lattice-weaknesses probably introduced pathways for Pb-leaching and as well intake of REE (preferentially LREE) during annealing.
- Within U-Th-enriched areas in Bergslagen, the "Hoskins discrimination diagrams" should be used with caution when evaluating if zircons are of hydrothermal origin. Petrographic context and Th/U ratios may be more useful.
- The evolution of the magmatic system into late-stage magmatic system and later into a hydrot-

hermal system follows a systematically trend by lower Th, U and (generally) REE contents in zircon, and can be distinguishable in bivariate plots.

- The Högberget granite and the Wigström skarn system evolved under relatively reduced conditions, as indicated by oxygen fugacity plot, but also by the presence of ilmenite (Bergman et al. 1995) in the former.
- In the Wigström deposit, W-Mo enrichment have a strong relationship with F enrichment, as suggested from field work, drill core loggings and SEM-images.
- The Wigström skarn evolved during similar processes describe in literature (e.g. Meinert et al. 2005) i.e. prograde to retrograde stages, and were typical proximal garnet and distal pyroxene zonation was observed in the field and prograde typically relates to skarnification (e.g. garnet and pyroxene), while the retrograde stages relates to hydrothermal qz-cal-fl veins to veinlets that associates with accessory minerals such as sch, mo, zrn and sulfides.

7 Future studies

- Further zircon U-Pb analyses are required in order to fortify statistical data regarding the emplacement age of the Högberget granite.
- To verify and strengthen the achieved age of the Wigström skarn, an age constrain with another geochronometer could be useful: e.g. U-Pb on skarn-hosted titanite or wolframite, Re-Os on skarn-hosted molybdenum and Rb-Sr on skarn-hosted sphalerite.
- For the skarn-hosted retrograde phase, fluid inclusion studies with laser Raman could provide insight of homogenization temperatures and fluid salinity. Also, Sulphur isotope studies on e.g. pyrite, chalcopyrite can be of interest. Both of these could be utilized as a comparable proxy to other skarn mineralization, and the former could relate temperature to the origin of Zr for hydrothermal zircon (e.g. granite, wall rocks).
- Hydrogen and oxygen isotopes studies could be utilized to trace the Zr source of the Type H zircon (e.g. wall rocks).

8 Acknowledgment

I would like to thank my supervisors Ulf Söderlund from the Department of Geology at Lund University and Edward Lynch from the Swedish Geological Survey (SGU) for all practical and technical support and as well for all fruitful discussions during all of the different stages within this project. The big support from Tomas Næraa from the Department of Geology at Lund's University is highly recognized, such as laboratory work i.e. grinding, polishing, SEM- and LA-ICPMS-analyses and for all the analytical help and discussions. Humble thanks to SGU for support in form of project funding and logistics within Sweden. I like to send thanks to all of the people at SGU Uppsala and Malå for their kind support and help. Lastly, I would like to thank all friends, colleges and family for the support during this time.

9 References

Aja, S. U., Wood, S. A. & Williams-Jones, A. E., 1995: The aqueous geochemistry of Zr and the solubility of some Zr-bearing minerals. *Applied Geochemistry 10*, 603-620. doi: https://doi.org/10.1016/0883-2927(95)00026-7.

Allen, R., Lundström, I., Ripa, M. & Christofferson, H., 1996: Facies analysis of a 1.9 Ga, continental margin, back-arc, felsic caldera province with diverse Zn-Pb-Ag-(Cu-Au) sulfide and Fe oxide deposits, Bergslagen Region, Sweden. *Economic Geology Vol. 91*, 1996, pp. 979-1008.

Allen, R. L., Bull, S., Ripa, M. & Jonsson, R., 2003: Regional Stratigraphy, Basin Evolution, and the Setting of Stratabound Zn-Pb-Cu-Ag-Au Deposits in Bergslagen, Sweden. Final report to the Geological Survey of Sweden (SGU) and Boliden Mineral AB; SGU-FoU project 03-1203/99. 80pp.

Artemieva, I., Thybo, H., Jakobsen, K., Sørensen, N. & S.K. Nielsen, L., 2017: Heat production in granitic rocks: Global analysis based on a new data compilation GRANITE2017. *Earth-Science Reviews.* 172. 10.1016/ j.earscirev.2017.07.003.

Baker, H. J. & Hellingwerf, R., 1988: Rare earth element geochemistry of W-Mo-(Au) skarns and granites from Western Bergslagen, central Sweden: *Mineralogy and Petrology Vol. 39*. 231-244.

Bao, Z., Sun, W., Li, C. & Zhao, Z., 2014: U–Pb dating of hydrothermal zircon from the Dongping gold deposit in North China: Constraints on the mineralization processes: *Ore Geology Reviews 61*, 107-119. doi: https:// doi.org/10.1016/j.oregeorev.2014.02.006.

Bergman, T., Schöberg, H. & Sundblad, K., 1995: Geochemistry, age, and origin of the Högberget granite, western Bergslagen, Sweden: *GFF 117*, 87-95. doi: 0.1080/11035899509546205.

Beunk, F. F. & Kuipers, G., 2012: The Bergslagen ore province, Sweden: Review and update of an accreted orocline, 1.9–1.8 Ga BP: *Precambrian Research*. 216–219.

Billström, K., 1990: Origin of the Yxsjöberg W-Cu skarn deposit, Bergslagen, south-central Sweden: Oxygen isotope evidence: *Geologiska Föreningen i Stockholm Förhandlingar 112*, 175-176. doi: 10.1080/11035899009453181.

Billström, K., Aberg, G. & Ohlander, B., 1988: Isotopic and geochemical data of the Pingstaberg Mo-bearing granite in Bergslagen, south central Sweden: *Geologie en Mijnbouw 67*. 255-263.

Bindeman, I. N., Palandri, J., Serebryakov, N. S., Schmitt, A. K., Vazquez, J. A., Guan, Y., Astafiev, B. Y., Azimov, P. Y. & Dobrzhinetskaya, L., 2014: Field and microanalytical isotopic investigation of ultradepleted in 18O Paleoproterozoic "Slushball Earth" rocks from Karelia, Russia: *Geosphere 10*, 308-339. doi: 10.1130/GES00952.1.

Chaves, A. D. O., Ernst, R. E., Söderlund, U., Wang, X. & Naeraa, T., 2019: The 920–900 Ma Bahia-Gangila LIP of the São Francisco and Congo cratons and link with Dashigou-Chulan LIP of North China craton: New insights from U-Pb geochronology and geochemistry: *Precambrian Research 329*, 124-137. doi: https://doi.org/10.1016/j.precamres.2018.08.023.

Chen, R.-X., Zheng, Y.-F. & Xie, L., 2010: Metamorphic growth and recrystallization of zircon: Distinction by simultaneous in-situ analyses of trace elements, U–Th–Pb and Lu–Hf isotopes in zircons from eclogite-facies rocks in the Sulu orogen: *Lithos 114*, 132-154. doi: https://doi.org/10.1016/j.lithos.2009.08.006.

Degryse, P. 2012: Isotopic Analysis: Fundamentals and Applications Using ICP-MS. Wiley VCH Verlag & Co. KGaA, Weinheim, Germany, 373-390. doi: 10.1002/9783527650484.ch13.

Demirer, K., 2012: U-Pb baddeleyite ages from mafic dyke swarms in Dharwar craton, India – links to an ancient supercontinent. In: L. U. Master's thesis, Lund, Sweden. Published thesis (red.).

Dietrich, R. V., 1968: Behavior of zirconium in certain artificial magmas under diverse P-T conditions: *Lithos 1*, 20-29. doi: https://doi.org/10.1016/S0024-4937(68)80032-5

Eilu, P., 2012: Eilu, P. (ed.) 2012. Mineral deposits and metallogeny of Fennoscandia. Geological Survey of Finland, Special Paper 53, 401 pp.

French, J. & Heaman, L., 2010: Precise U-Pb dating of Paleoproterozoic mafic dyke swarms of the Dharwar craton, India: Implications for the existence of the Neoarchean supercraton Sclavia: *Precambrian Research 183*, 416-441. doi: 10.1016/j.precamres.2010.05.003

Geijer, P. & Magnusson, N. H., 1944: *De mellansvenska järnmalmernas geologi*. *Sveriges geologiska undersökning 35*, 654 pp.

Geisler, T., Tomaschek, F., Rashwan, A. A., Rahn, M. K. W., Poller, U., Zwingmann, H., Pidgeon, R. T. & Schleicher, H., 2003: Low-temperature hydrothermal alteration of natural metamict zircons from the Eastern Desert, Egypt. *Mineralogical Magazine 67*, 485-508. doi: 10.1180/0026461036730112

Hegeman, J. B. J. W., De Hosson, J. T. M. & De With, G., 2001: Grinding of WC–Co hardmetals: *Wear 248*, 187-196. doi: https://doi.org/10.1016/S0043-1648(00)00561-5

Hellingwerf, R. H., Baker, J. H. & Van Raaphorst, J. G., 1987: Sulphur isotope data of Proterozoic molybdenites from western Bergslagen, Sweden: *Geologiska Föreningen i Stockholm Förhandlingar 109*, 33-38. doi: 10.1080/11035898709454737

Hinton, R. W. & Upton, B. G. J., 1991: The chemistry of zircon: Variations within and between large crystals from syenite and alkali basalt xenoliths: *Geochimica et Cosmochimica Acta 55*, 3287-3302. doi: https://doi.org/10.1016/0016-7037(91)90489-R

Högdahl, K., Peter Gromet, L. & Broman, C., 2001: Low P - T Caledonian resetting of U-rich Paleoproterozoic zircons, central Sweden: *American Mineralogist 86*. 534-546. doi: 10.2138/am-2001-0416.

Horie, K., Hidaka, H. & Gauthier-Lafaye, F., 2006: Elemental distribution in zircon: Alteration and radiation-damage effects: *Physics and Chemistry of the Earth, Parts A/B/C 31*, 587-592. doi: https://doi.org/10.1016/j.pce.2006.01.001

Hoskin, P. W. O., 2005: Trace-element composition of hydrothermal zircon and the alteration of Hadean zircon from the Jack Hills, Australia: *Geochimica et Cosmochimica Acta 69*, 637-648. doi: https://doi.org/10.1016/j.gca.2004.07.006

Hoskin, P. W. O. & Schaltegger, U., 2003: *The composition of zircon and igneous and metamorphic petrogenesis*.: Reviews *in Mineralogy & Geochemistry - REV MINERAL GEOCHEM. 53*. 27-62. 10.2113/0530027.

Hsu, L. C. & Galli, P. E., 1973: Origin of the Scheelite -Powellite Series of Minerals: *Economic Geology 68*, 681-696. doi: 10.2113/gsecongeo.68.5.681

Jifu, S., Lijun, L. I. U., Denghong, W., Zhenghui, C., Lijuan, Y., Fan, H., Jiahuan, W. & Le, Z., 2015: A Preliminary Review of Metallogenic Regularity of Tungsten Deposits in China: *Acta Geologica Sinica (English Edition) 89*, 1359-1374. doi: 10.1111/1755-6724.12533

Johansson, Å., 2019: A refined U-Pb age for the Stockholm granite at Frescati, east-central Sweden: *GFF 141*, 40-47. doi: 10.1080/11035897.2018.1555186

Keith, S. B. & Westra, G., 1981: Classification and genesis of stockwork molybdenum deposits: *Economic Geology 76*, 844-873. doi: 10.2113/gsecongeo.76.4.844

Keppler, H., 1993: Influence of fluorine on the enrichment of high field strength trace elements in granitic rocks: *Contributions to Mineralogy and Petrology 114*, 479-488. doi: 10.1007/BF00321752.

Kerrich, R. & King, R., 1993: *Hydrothermal zircon and baddeleyite in Vald'Or Archean meso-*

thermal gold deposits: Characteristics, compositions, and fluid-Inclusion properties, with implications for timing of primary gold mineralization. 2334-2351 sid.

Košler, J., 2007: Laser ablation ICP—MS — a new dating tool in Earth science: *Proceedings of the Geologists' Association 118*, 19-24. doi: https://doi.org/10.1016/S0016-7878(07)80043-5

Kovalenko, V. I., Goreglyad, A. V., Farmer, G. L., Tsaryeva, G. M., Hervig, R. L., Troitsky, V. A. & Yarmolyuk, V. V., 1995: The peralkaline granite-related Khaldzan-Buregtey rare metal (Zr, Nb, REE) deposit, western Mongolia: *Economic Geology 90*, 530-547. doi: 10.2113/gsecongeo.90.3.530

Kozlik, M., Raith, J. G. & Gerdes, A., 2016: U–Pb, Lu–Hf and trace element characteristics of zircon from the Felbertal scheelite deposit (Austria): New constraints on timing and source of W mineralization: *Chemical Geology 421*, 112-126. doi: https://doi.org/10.1016/j.chemgeo.2015.11.018

Krogh, T. E., 1973: A low-contamination method for hydrothermal decomposition of zircon and extraction of U and Pb for isotopic age determinations: *Geochimica et Cosmochimica Acta 37*, 485-494. doi: https://doi.org/10.1016/0016-7037(73)90213-5

Krogh, T. E. & Davis, G. L., 1975: Alteration in zircons and differential dissolution of altered and metamict zircon: *Carnegie Institution of Washington Yearbook 74*, 619-623.

Larson, S., ÅKe & Tullborg, E.-L., 1998: Why Baltic Shield zircons yield late Paleozoic, lower-intercept ages on U-Pb concordia: *Geology 26*, 919-922. doi: 10.1130/0091-7613(1998)026<0919:WBSZYL>2.3.CO;2

Lassner, E. & Schubert, W.-D., 1999: Tungsten: Properties, Chemistry, Technology of the Element, Alloys and Chemical Compounds. Kluwer Academic/Plenum Publ. New York, 422 pp.

Li, H., Watanabe, K. & Yonezu, K., 2014: Zircon morphology, geochronology and trace element geochemistry of the granites from the Huangshaping polymetallic deposit, South China: Implications for the magmatic evolution and mineralization processes: *Ore Geology Reviews 60*, 14-35. doi: https://doi.org/10.1016/j.oregeorev.2013.12.009

Lindroth, G. T., 1922: Studier över Yxsjöfältets geologi och petrografi: *Geologiska Föreningens i Stockholm Förhandlingar 44*, 20-123.

Lundström, I., 1987: Lateral variations in supracrustal geology within the swedish part of the southern svecokarelian volcanic belt: *Precambrian Research 35*, 353-365. doi: https://doi.org/10.1016/0301-9268(87)90063-5

Lundström, I., Allen, R. L., Persson, P.-O. & Ripa, M., 1998: Stratigraphies and depositional ages of Svecofennian, Palaeoproterozoic metavolcanic rocks in E. Svealand and Bergslagen, south central Sweden: *GFF 120*, 315-320. doi: 10.1080/11035899809453225

Lynch, P. E., Ripa, M., Selby, D. & Lundin, A. I., 2019: Mo mineralization in western Bergslagen, Sweden, marks pre- and late-collisional tectonothermal events during Svecokarelian orogenesis. *15th Biennial Meeting of the Society for Geology Applied to Mineral Deposits.* Glasgow, England.

Magnusson, N. H., 1940: Ljusnarsbergs malmtrakt, berggrund och malmfyndigheter: *Sveriges Geologiska Undersökning Ca 30*, 1-188.

Manhes, G., Minster, J. F. & Allègre, C. J., 1978: Comparative uranium-thorium-lead and rubidium-strontium study of the Saint Severin amphoterite - Consequences for early solar system chronology. *Earth Planet. Sci. Lett. 39*. 14-24.

Mathieu, R., Zetterström, L., Cuney, M., Gauthier-Lafaye, F. & Hidaka, H., 2001: Alteration of monazite and zircon and lead migration as geochemical tracers of fluid paleocirculations around the Oklo–Okélobondo and Bangombé natural nuclear reaction zones (Franceville basin, Gabon): *Chemical Geology 171*, 147-171. doi: https://doi.org/10.1016/S0009-2541(00)00245-X

Meinert, L., Dipple, G. & Nicolescu, S. 2005: World Skarn Deposits. *I*, 299–336,

Mezger, K. & Krogstad, E. J., 1997: Interpretation of discordant U-Pb zircon ages: An evaluation: *Journal of Metamorphic Geology 15*, 127-140. doi: 10.1111/j.1525-1314.1997.00008.x

Oen, I.S., Helmers, H., Verschure, R.H. & Wiklander, U., 1982: Ore deposition in a Proterozoic incipient rift zone environment: A tentative model for the Filipstad-Grythyttan- Hjulsjö region, Bergslagen, Sweden. *Geologische Rundschau 71*, 182–194.

Ohlsson, L. G., 1979: Tungsten occurrences in central Sweden: *Economic Geology Vol. 74*, 1012-1034.

Patchett, P. J., Todt, W. & Gorbatschev, R., 1987: Origin of continental crust of 1.9-1.7 ga age: nd isotopes in the svecofennian orogenic terrains of sweden: *Precambrian Research 35*, 145-160. doi: https://doi.org/10.1016/0301-9268(87)90050-7

Pidgeon, R., O'neil, J. & T. Silver, L., 1966: Uranium and Lead Isotopic Stability in a Metamict Zircon under Experimental Hydrothermal Conditions. *Science Vol. 154*, Issue 3756. 1538-1540 DOI: 10.1126/science.154.3756.1538

Pitfeld, P., Brown, T., Gunn, G. & Rayner, D., 2011: Tungsten. *In:* T. d. o. a. s.-s. mineralization's (red.) Keyworth, Nottingham, United Kingdoms. 1-34.

Romer, R., L & Öhlander, B., 1994: *U-Pb age of the Yxsjöberg Tungsten-Skarn deposit, Sweden*. *GFF* 116, 161-166.

Rubatto, D., 2002: Zircon trace element geochemistry: partitioning with garnet and the link between U–Pb ages and metamorphism: *Chemical Geology 184*, 123-138. doi: https://doi.org/10.1016/S0009-2541(01)00355-2

Rubatto, D., 2017: Zircon: The Metamorphic Mineral: *Reviews in Mineralogy and Geochemistry 83*, 261-295. doi: 10.2138/rmg.2017.83.9

Rubin, J., Henry, C. & Price, J., 1989: Hydrothermal zircons and zircon overgrowths, Sierra Blanca Peaks, Texas. Texas. *American Mineralogist 74*. 865.

Rubin, J. N., Henry, C. D. & Price, J. G., 1993: The mobility of zirconium and other "immobile" elements during hydrothermal alteration: *Chemical Geology 110*, 29-47. doi: https://doi.org/10.1016/0009-2541(93)90246-F

Salvi, S. & Williams-Jones, A. E., 2006: Alteration, HFSE mineralisation and hydrocarbon formation in peralkaline igneous systems: Insights from the Strange Lake Pluton, Canada: *Lithos 91*, 19-34. doi: https://doi.org/10.1016/j.lithos.2006.03.040

Schaltegger, U., 2007: *Hydrothermal Zircon*: Elements, 51-79.

Schoene, B., 2014: 4.10 – U–Th–Pb geochronology. *Elsevier, Oxford*, 341-378.

Söderlund, U., 1996: Conventional U-Pb dating versus single-grain Pb evaporation dating of complex zircons from a pegmatite in the high-grade gneisses of southwestern Sweden: *Lithos 38*, 93-105. doi: https://doi.org/10.1016/0024-4937(95)00042-9

Söderlund, U. & Johansson, L., 2002: *A simple way to extract baddeleyite (ZrO2)*: Geochemistry Geophysics Geosystems - GEOCHEM GEOPHYS GEOSYST. 3.

Stein, H. J., Sundblad, K., Markey, R. J. & Morgan, J. W., 1996: New Tools, New Interpretations: A Re-Os Revelation at the Skarn Deposits of Pitkäranta, Russia. *goldschmidt conf. 594.*

Stephens, M., Ripa, M., Lundström, I., Persson, L., Bergman, T., Ahl, M., Wahlgren, C.-H., Persson, P. O. & Wickström, L., 2009: Synthesis of bedrock geology in the Bergslagen region, Fennoscandian Shield, south-central Sweden. *SGU Ba 58*, 1-259.

Sundblad, K., Stein, H., Markey, R. J., Morgan, J. W. & Bergman, T., 1996: Re-Os age and geochemistry of highly evolved granites associated with Mo and W ore deposits in Bergslagen, Sweden. : *7th International Symposium on Rapakivi Granites and Related Rocks, abstract volume 73−74*.

T., S. L., 1991: Daughter-parent isotope systematics in U-Th-bearing igneous accessory mineral assemblages as potential indices of metamorphic history: A discussion of the concept.: Stable Isotope Geochemistry: A Tribute to Samuel Epstein (ed. H. P. Taylor, et al.), *Geochem. Soc. Spec. Publ. 3*, 391–407.

Wang, X., Chen, J. & Ren, M., 2016: Hydrothermal zircon geochronology: Age constraint on Nanling Range tungsten mineralization (Southeast China): *Ore Geology Reviews 74*, 63-75. doi: https://doi.org/10.1016/j.oregeorev.2015.10.034

Webster, J., Thomas, R., Rhede, D., Förster, H. J. & Seltmann, R., 1997: *Melt inclusions in quartz from an evolved peraluminous pegmatite: geochemical evidence for strong tin enrichment in fluorine-rich and phosphorus-rich residual liquids*. *Geochimica et Cosmochimica Acta. 61.* 10.1016/S0016-7037(97)00123-3.

Wei, W.-F., Shen, N.-P., Yan, B., Lai, C.-K., Yang, J.-H., Gao, W. & Liang, F., 2018: Petrogenesis of ore-forming granites with implications for W-mineralization in the super-large Shimensi tungsten-dominated polymetallic deposit in northern Jiangxi Province, South China: *Ore Geology Reviews 95*, 1123-1139. doi: https://doi.org/10.1016/j.oregeorev.2017.12.022

Wilson, M. R. & Åkerblom, G. V., 1982: Geological Setting and Geochemistry of Uranium-rich Granites in the Proterozoic of Sweden. *Mineral. Mag. 46*, 233-245.

Woodward, J., Sundblad, K. & Schöberg, H., 2009: Disturbance of U-Pb in zircons by Mo-W-mineralising magmatic fluids in the late Svecofennian Bipsbergs Klack granite, Sweden: *GSA Annual Meeting, Portland Program and abstracts,* 158-9.

Xiaodong, D., Li, J.-W. & Wen, G., 2015: U-Pb Geochronology of Hydrothermal Zircons from the Early Cretaceous Iron Skarn Deposits in the Handan-Xingtai District, North China Craton. *Economic Geology. 110.* 2159-2180. 10.2113/econgeo.110.8.2159.

Yang, W., Niu, H., Shan, Q., Sun, W., Zhang, H., Li, N.-B., Jiang, Y. & Yu, X.-Y., 2013: Geochemistry of magmatic and hydrothermal zircon from the highly evolved Baerzhe alkaline granite: Implications for Zr-REE-Nb mineralization. *Mineralium Deposita. 49.* 10.1007/s00126-013-0504-1.

Zhao, Z., Liu, C., Guo, N.-X., Zhao, W. W., Wang, P.-A. & Chen, Z.-H., 2018: Temporal and spatial relationships of granitic magmatism and W mineralization: Insights from the Xingguo orefield, South China: *Ore Geology Reviews 95*, 945-973. doi: https://doi.org/10.1016/j.oregeorev.2018.03.022

Zhong, S., Feng, C., Seltmann, R., Li, D. & Qu, H., 2018: Can magmatic zircon be distinguished from hydrothermal zircon by trace element composition? The effect of mineral inclusions on zircon trace element composition: *Lithos 314-315*, 646-657. doi: https://doi.org/10.1016/j.lithos.2018.06.029

Appendix 1 – Analytical techniques

Zircon imaging and skarn petrography

Imaging of zircon and skarn was performed at the Department of Geology, Lund University using a Tescan Mira3 High Resolution Schottky Field Emission (FE)-scanning electron microscope (SEM) equipped with Oxford backscattered electrons (BSE), cathodoluminescence (CL) and energy-dispersive X-ray spectroscopy (EDS) detectors. Prior to imaging, the samples coated with c. 18 nm carbon and then mounted on a sample holder. Sample boarders were clad in aluminium tape and silver paint in order to avoid electrical charging during beam-time. The SEM was operated in BSE-, CL- and EDS modes under high vacuum with the electron beam voltage set to 15 keV and a working distance of c. 15 mm. The main purpose was to document internal zircon textures in order to secure suitable target area for LA-ICPMS analyses i.e. domains free from heterogeneities (e.g. inclusions, fractures). Data collected from EDS were mainly utilized to identify different mineral inclusions in zircons but also to classify the skarn mineralogy in the thick sections e.g. zircon, scheelite, garnet, sphalerite, pyroxene, quartz, calcite, fluorite etc.

Zircon U-Pb LA-ICPMS geochronology and REE geochemistry

The analyses involved ablation of both zircon crystals cast in epoxy-pucks (granitic separates) and in-situ embedded (skarn thick sections). Samples were mounted into an HelEx 2-volume sample cell equipped with an eQC in-situ energy detector. The sample chamber is incorporated in a Teledyne Photon Machines G2 excimer laser of 193 nm wavelength, delivering ultra-short-pulses <4 ns. The ablated aerosols were transferred from the sample cell via 2 mm ID PFTE tubing with insert "squid" by a carrier gas-mix consisting of helium (0.8 l/min) and nitrogen (6.5 ml/min), and with argon injected down-stream before entering the plasma torch. ICP-MS instrument consists of a Bruker Aurora Elite Quadrupole ICP-MS with a DDEM (discrete dynode electron multiplier) single collector, operating at c. 1300 W, and with argon (0.95 l/min) as the make-up gas. Prior to zircon analyses, instrument tuning was performed, utilizing NIST SRM 612 reference glass, with aims of achieving high and stable signal counts on lead and other relevant isotopes, on low oxide production (<0.5 % monitoring $^{238}U/^{238}U^{16}O$ and $^{232}Th/^{232}Th^{16}O$) and on Th/U ratios around 1. Generally, the ablated spot size was set to 20x20 µm but depending on the zircons proportions and desired ablation area, various sizes (e.g. 20x20 µm, 15x27 µm and 14x29 µm). Aspect ratios between 1:1 and 1:2 were utilized, but the ablated area was always kept close to 400 μm^2. Analytical session was setup to run automatically with standard-sample-standard bracketing, approximately with 10 analyses between each standard block. In order to monitor instrument stability, the natural reference zircon GJ-1 and certified NIST SRM 610 reference glass were used as standard materials for geochronology and trace element analyses, respectively. Repeated analyses on natural reference zircon 91500 (Wiedenbeck et al. 1995) and certified NIST SRM 612 reference glass were analysed as unknowns for quality check. ^{90}Zr was used as internal standard for trace element analyses. Zircon REE abundances were determined from the same spots as the U-Th-Pb analyses.

The samples were analysed in four sequences, three of these were done with 270 shots at 9 Hz and one sequence was done with 12 Hz and 360 shots, constraining a fluency of 2.5 J/cm^2 on zircons and 3.5 J/cm^2 on the NIST glass, in all four sequences. Each analysis incorporated a background acquirement of 30 seconds (gas blank) before each measurement, and subtraction was done with a step-forward approach. Common Pb was monitored by measuring ^{202}Hg and mass 204 ($^{204}Hg+^{204}Pb$), baseline levels on mass 204 was around 750 counts per seconds (CPS) with a standard error (SE) around 20 CPS (c. 2-3 %).

Data reduction was done using the Iolite software extension within the Wavemetrics IgorPro software; for geochronological data the X_U_Pb_Gerchron4 data reduction scheme (DRS) was used (Paton et al. 2010; Paton et al. 2011). Common Pb correction was done using the VizualAge DRS by Petrus and Kamer (2012) and for trace elements the X_Trace_Elements_IC DRS was used assuming a Zr concentration of 43.14 wt. % for the analysed zircon grains. The acquired data was gathered in Microsoft Excel spreadsheets, whereas geochronological isotopic ratios was processed with ISOPLOT. Interpreted geochronological ages are based on $^{207}Pb/^{206}Pb$ isotopic ratio, which is a commonly applied for zircons exceeding 1.0 Ga (e.g. Allen & Campbell 2012).

C1-normalized data according to Boynton (1984) are recognized by subscript of letter "n" e.g. La_n. REE C1-normailized spiderplots was produced with R language package (R_Console 3.4.3) in GCDkit 5.0 (Janousek et al. 2006). Bivariate trace element diagrams were plotted in Microsoft Excel. Europium and Cerium geometric means was calculated from: $Eu/Eu^* = (Eu)_n/\sqrt{(Sm \times Gd)_n}$ and $Ce/Ce^* = (Ce)_n/\sqrt{(La \times Pr)_n}$, respetivly.

Reference in appendix 1

Allen, C. M. & Campbell, I. H., 2012: Identification and elimination of a matrix-induced systematic error in LA–ICP–MS 206Pb/238U dating of zircon: *Chemical Geology 332-333*, 157-

165. doi: https://doi.org/10.1016/j.chemgeo.2012.09.038
Boynton, W. V. 1984: Chapter 3 - Cosmochemistry of the Rare Earth Elements: Meteorite Studies. *I* P. Henderson (red.): *Developments in Geochemistry*, 63-114. Elsevier,
Janousek, V., M. Farrow, C. & Erban, V., 2006: Interpretation of Whole-rock Geochemical Data in Igneous Geochemistry: Introducing Geochemical Data Toolkit (GCDkit). 1255-1259 sid.
Paton, C., Hellstrom, J., Paul, B., Woodhead, J. & Hergt, J., 2011: Iolite: Freeware for the visualisation and processing of mass spectrometric data: *Journal of Analytical Atomic Spectrometry*. doi: doi:10.1039/c1ja10172b
Paton, C., Woodhead, J. D., Hellstrom, J. C., Hergt, J. M., Greig, A. & Maas, R., 2010: Improved laser ablation U-Pb zircon geochronology through robust downhole fractionation correction: *Geochemistry, Geophysics, Geosystems 11*. doi: 10.1029/2009GC002618
Petrus, J. A. & Kamber, B. S., 2012: VizualAge: A Novel Approach to Laser Ablation ICP-MS U -Pb Geochronology Data Reduction: *Geostandards and Geoanalytical Research 36*, 247-270. doi: 10.1111/j.1751-908X.2012.00158.x
Wiedenbeck, M., Allé, P., Corfu, F., Griffin, W. L., Meier, M., Oberli, F., Quadt, A. V., Roddick, J. C. & Spiegel, W., 1995: THREE NATURAL ZIRCON STANDARDS FOR U-TH-PB, LU-HF, TRACE ELEMENT AND REE ANALYSES: *Geostandards Newsletter 19*, 1-23. doi: 10.1111/j.1751-908X.1995.tb00147.x

Appendix 2 – Drill core logging results

Northern pit drill holes

WD-12 (1.50–34.60 m; Fig. 9a)
The upper part of the core consists of pure and massive quartz which has a yellowish fluorescence under UV-light. This is followed by a package of skarn-altered pegmatite (~4.5 m), interpreted as endoskarn, which includes a thin (~1m) pyroxene-scapolite skarn horizon. This assemblage yields no response under UV -C light and contains disseminated fluorite, molybdenite and sulfides. From 7.8 m a mix of wollastonite skarn and country rock follows, barren of ore-minerals. The main skarn horizon begins at c. 12 m and continues to c. 17 m and mainly consists of pyroxene-scapolite skarn (at the top) and massive quartz enclosing skarn alterations and ends with a c. 1 m-thick garnet-pyroxene skarn horizon. Different degree of altered country rock with minor sulfides follows the rest of the core (34.6 m), minor areas of skarn occurs were sulphide mineralization is more prominent.

WD-1 (0–39.83 m; Fig. 9b)
The uppermost part consists of granite with thin (<2 cm) cross-cutting pegmatitic veinlets, whereas the bottom vein act as a transition boundary towards the skarn horizon. The skarn assemblage consists of mainly different degrees of altered country rock (exoskarn) with minor sulphides, equal amounts of pyroxene-scapolite and garnet-pyroxene skarn rich in fluorite and with subordinate wollastonite skarn. About 8 m of the core towards the end is missing. About 9 m of extensive altered country rock occurs at the end of the core, from 28.76 m to 39.83 m.

WD-3 (0.20–24.96 m; Fig. 9c)
About 50 % (~13 m) of the core consists of granite with minor sulphides erratically scattered, merger cross-cutting pegmatitic veinlets are as well present. The rest of the core (13.80–24.96 m) consists of skarn. The uppermost part a c. 1.5 m endoskarn followed by a barren (~1 m) horizon of wollastonite skarn. An assemblage of garnet-pyroxene skarn horizon rich in fluorite with subordinate pyroxene-scapolite skarn neighbours the wollastonite and continues to c. 22 m were endoskarn, rich in sulphides. Molybdenite begins and follows until core-end at 24.96 m.

Main pit drill holes

DBH-5 (0.70–124.20 m; Fig. 9d)
The upper part of the core comprises 88 m of granite with cross-cutting pegmatitic veins (<5 cm). The granite becomes gradually coarser towards the contact with the country rock (88.07 m). The contact between granite and country rock is intensely skarn-altered and contains molybdenite, pyrite and chalcopyrite (down to 91.24 m), interpreted to be a endoskarn horizon, followed by country rock. At c. 101 m the country rock becomes skarn-altered and enriched with fluorite, followed by increased alteration forming endoskarn similar to the alteration at the country rock contact. The endoskarn has a strong UV-response and also abundant sulphide-networks. This endoskarn horizon develops into pyroxene-scapolite skarn between 105.50 and106.07 m. The main skarn horizon begins at c. 108.2 m and continuous for the following c. 8 m. This horizon comprises garnet-pyroxene- and pyroxene-scapolite skarn in equal amounts and are relatively enriched in fluorite and scheelite. The remaining c. 10 m consist of various degrees of skarn-altered country rock, until the core-end at 124.20 m.

DBH-1 (2.97–125.85 m; Fig. 9e)
The upper part consists of an 80.03 m granitic package with a high distribution of cross-cutting quartz-rich pegmatite (<10 cm). Towards the country rock contact, quartz becomes more abundant and foliated. The contact zone between the granite and the country rock has a mixture of endoskarn with little UV-response and altered country rock. The haphazard distribution of

endoskarn, pegmatite and alteration continuous until 108.03 m were the main skarn horizon begins. The skarn consists of an even mixture of garnet-pyroxene- and pyroxene-scapolite skarn, along with small horizons of weathered and porous skarn that ends at 122.20 m. Fluorite is present throughout the entire skarn package and is associated with the minor scheelite, pyrite and molybdenite. Noteworthy, areas with molybdenite networks/grains lack UV-response i.e. at 111.42 m and 113.83 m. Skarn-altered country rock and core-loss follows, until the core ends at 125.85 m.

WD-16 (0.45–103.08 m; Fig. 9f)
The top c. 29 m consist of granite with cross-cutting pegmatitic veins (<10 cm). At 3.51 m, inspection with a UV lamp yields a green response which may represent uranyl ions. The main core-volume consists of various degrees of skarn-altered country rock (~29.5–82 m) with subordinate endoskarn horizons and cross-cutting pegmatitic veinlets. The skarn-altered horizons within the country rock have UV-responses, indicative of scheelite, and occasionally contains pyrite. The main skarn horizon begins at c. 82 m and ends at a weathered assemblage of country rock, with subordinate skarn altered horizons. Pyroxene-scapolite skarn is the main skarn-type, with subordinate garnet-pyroxene skarn. This assemblage contains disseminated scheelite grains (<0.5 cm) which has a strong response under UV-light, and are also rich in fluorite, with a networks of sulfides between c. 84.7 m. The uppermost pyroxene-scapolite assemblage contains minor amounts of molybdenite.

WD-8 (8.95–42.85 m; Fig. 9g)
The uppermost part of the core (8.95–24.35 m) has endured extensive weathering and consists of a mix between skarn-altered country rock and pegmatite, whereas the pegmatite has a yellowish UV-response, indicative of powellite. The skarn horizon begins at 24.35 m with a c. 1 m skarn which is porous with a "sugary" texture, probably as a result of weathering. Followed by fluorite-rich pyroxene-scapolite assemblage with subordinate garnet-pyroxene skarn, both with a strong UV- response (c. 24.3–37.5 m). Four meters of skarn altered country rock occurs towards the end of the hole (42.85 m).

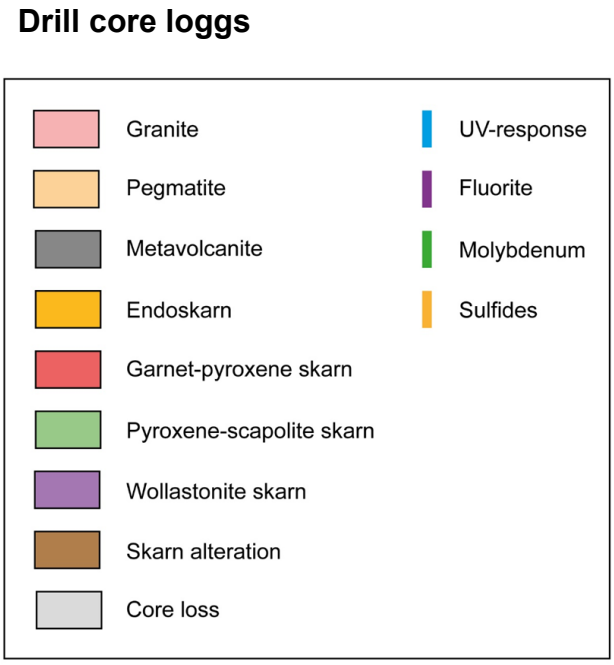

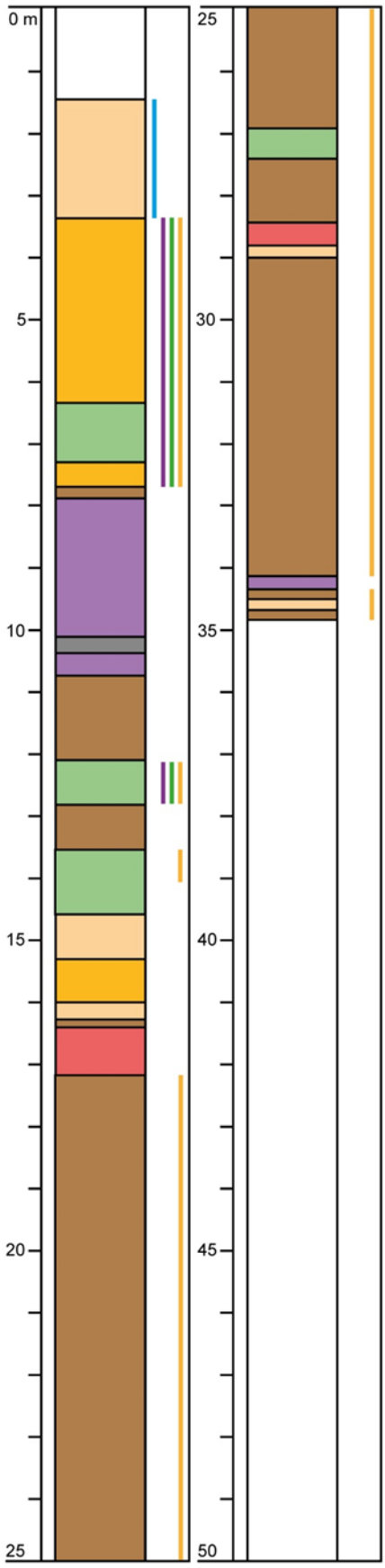

Drill core: WD-12, Northern –pit

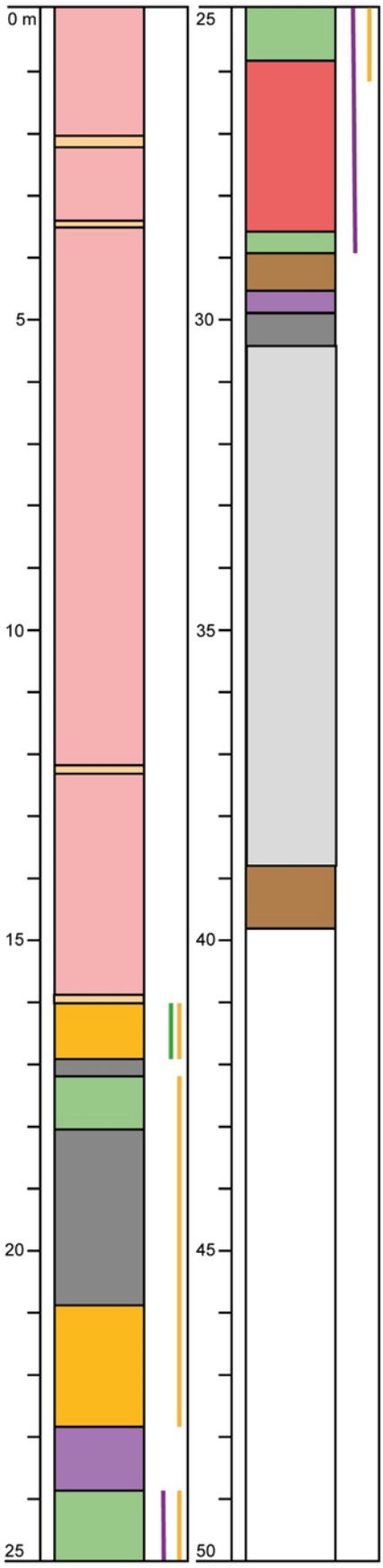

Drill core: WD-1, Northern –pit

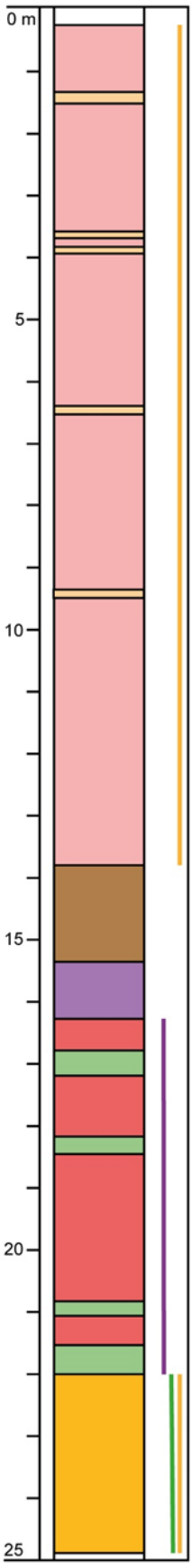

Drill core: WD-3, Northern –pit

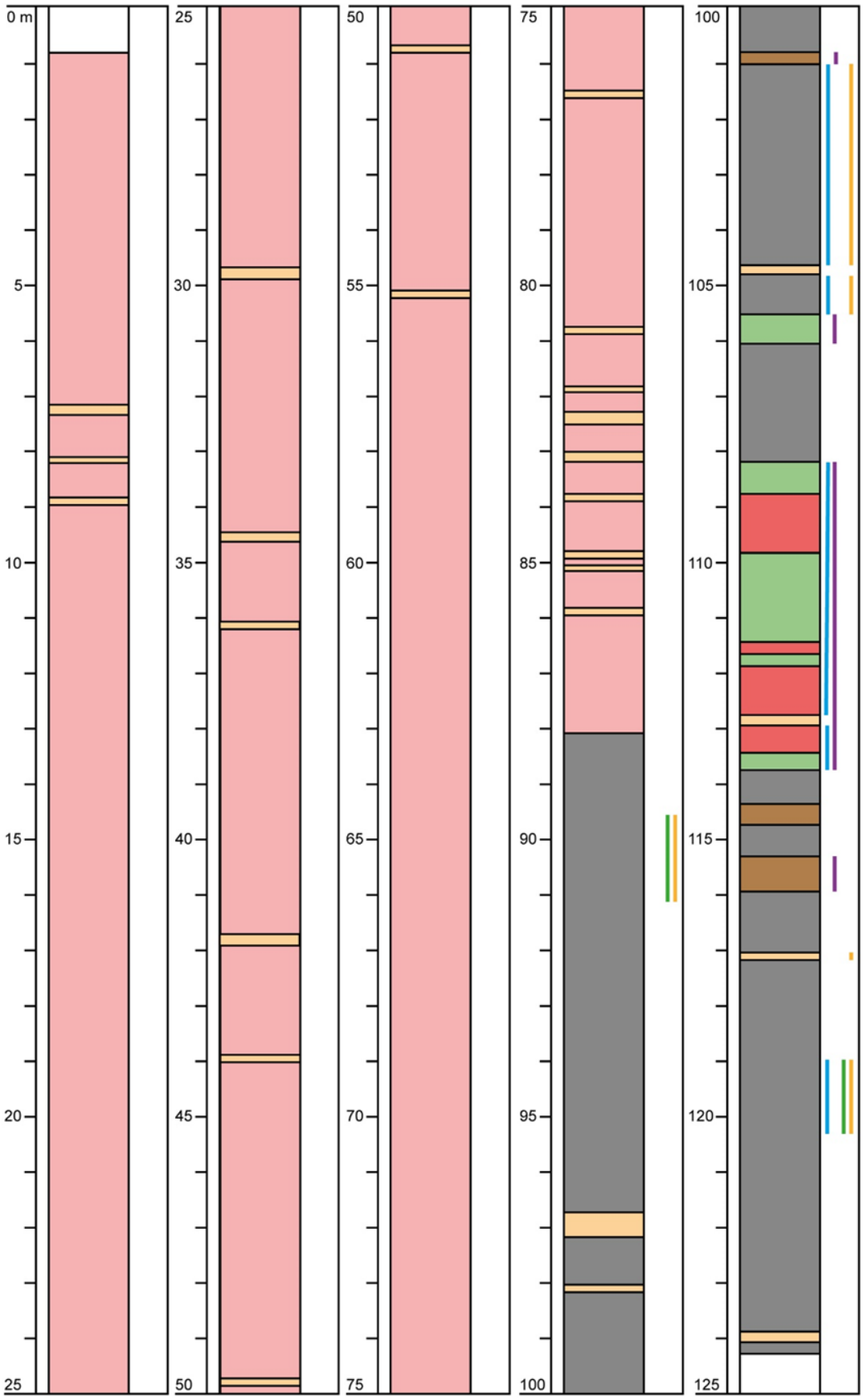

Drill core: DBH-5, Main-pit

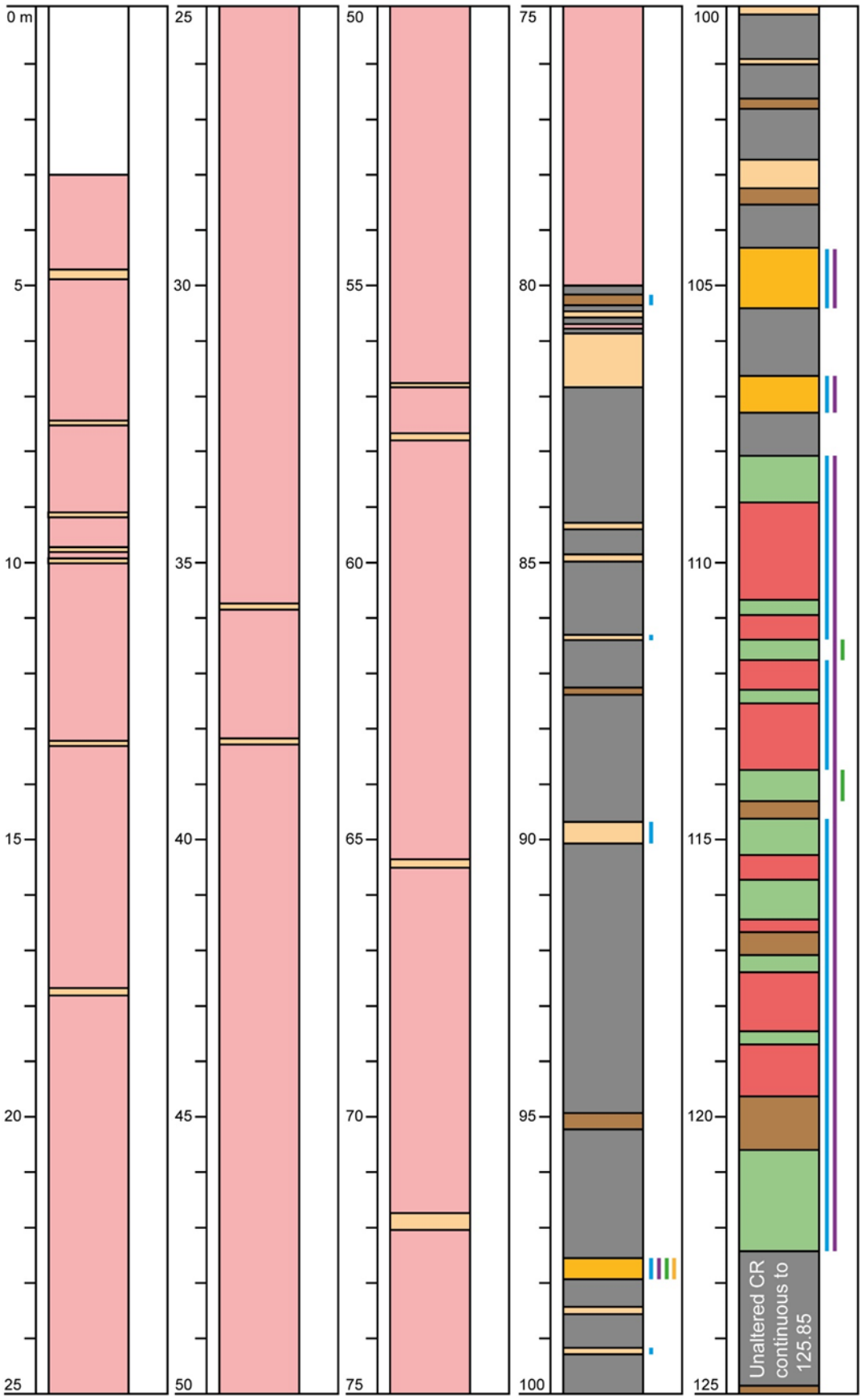

Drill core: DBH-1, Main-pit

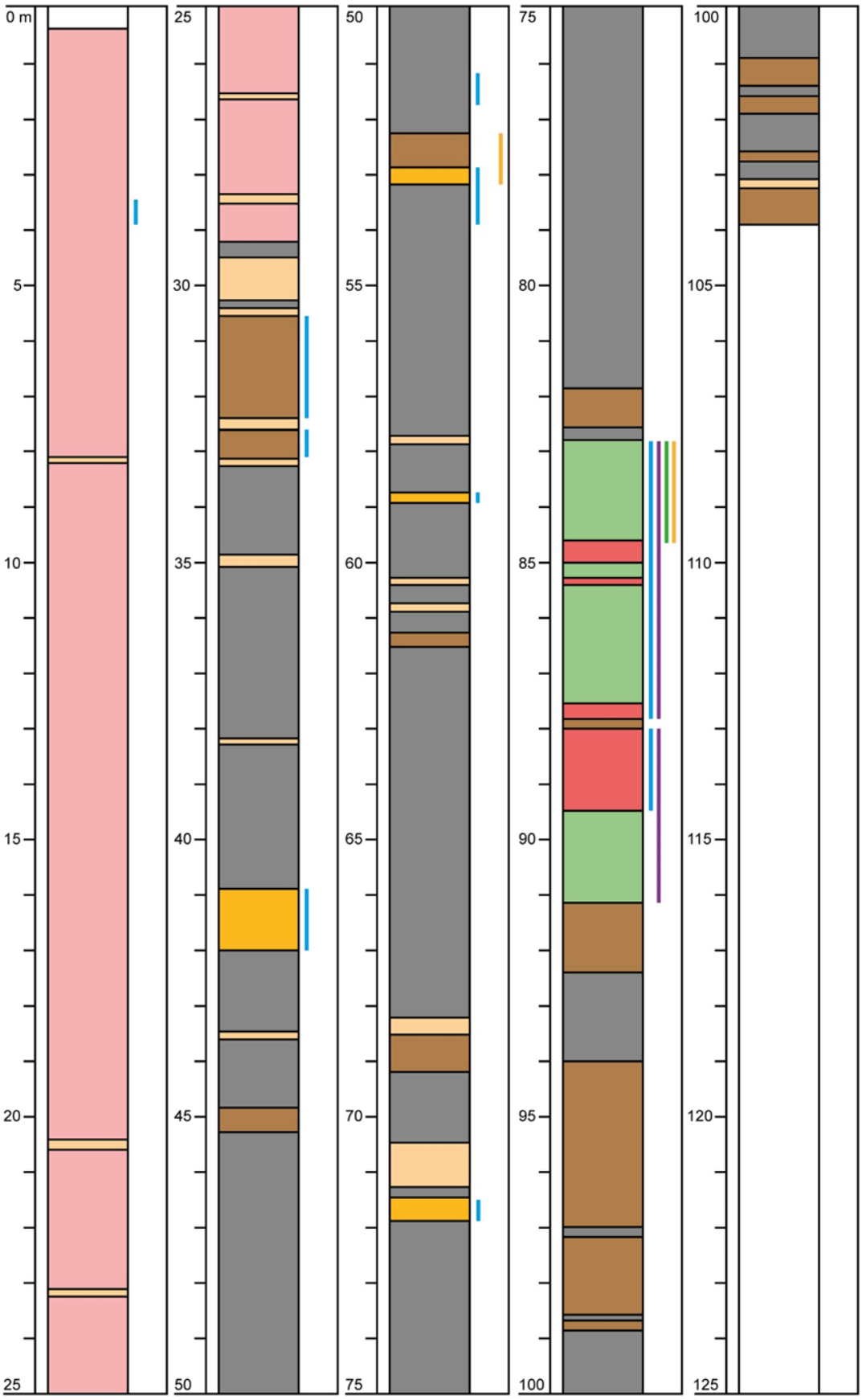

Drill core: WD-16, Main-pit

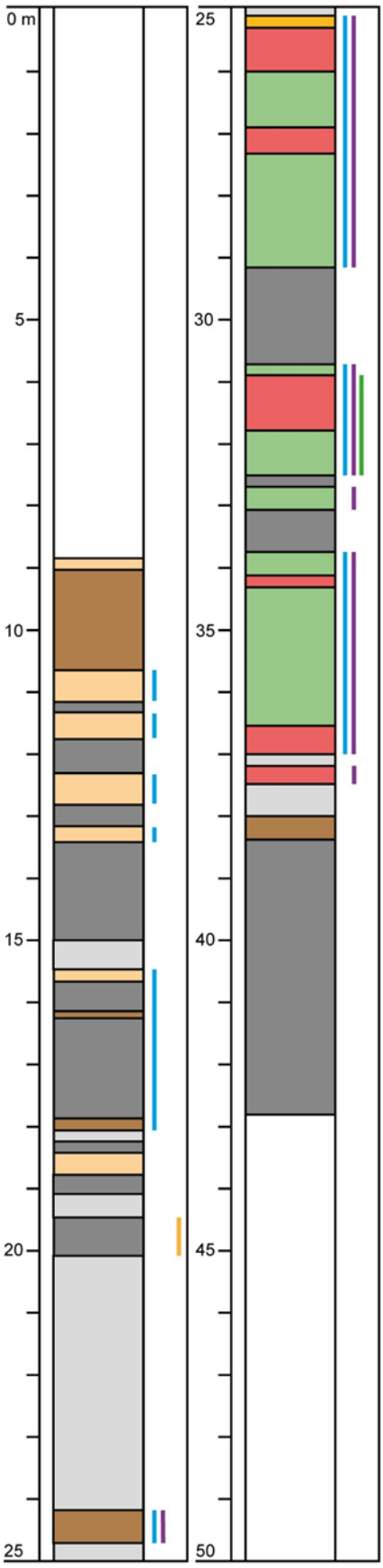

Drill core: WD-8, Main-pit

Appendix 3 (table 2) – Zircon REE LA-ICPMS data

Zircon REE trace element LA-ICPMS data

		Data in PPM												C1-normalized data[4]				
Ana. spot	Zrn type	La	Ce	Pr	Nd	Sm	Eu	Gd	Dy	Yb	ΣLREE[1]	ΣHREE[2]	ΣREE[3]	La/ Yb[4]	Sm/ La[4]	Gd/ Yb[4]	Eu/ Eu*[5]	Ce/ Ce*[6]
Sample APLH0001A – Högberget granite																		
H1-1	M1	130.60	441.00	44.20	181.00	79.70	9.90	164.00	535.00	1589.00	876.50	2297.90	3174.40	0.0554	0.9702	0.0833	0.2648	1.397
H1-2	M1	45.50	239.00	19.10	84.20	53.90	8.51	156.70	665.00	2184.00	441.70	3014.21	3455.91	0.014	1.8832	0.0579	0.2831	1.9513
H1-3	M1	65.20	198.00	17.10	74.00	32.60	4.68	102.10	400.00	1365.00	386.90	1871.78	2258.68	0.0322	0.7949	0.0604	0.248	1.4272
H1-4	M1	268.80	847.00	89.70	345.00	123.00	31.40	234.00	672.00	1861.00	1673.50	2798.40	4471.90	0.0974	0.7274	0.1015	0.5659	1.3129
H1-5	M1	266.00	925.00	100.10	411.00	138.30	37.10	262.00	716.00	1897.00	1840.40	2912.10	4752.50	0.0945	0.8265	0.1115	0.5959	1.3644
H1-6	M1	291.40	802.00	84.70	328.30	111.90	36.20	243.80	769.00	2140.00	1618.30	3189.00	4807.30	0.0918	0.6105	0.0919	0.6701	1.2287
H1-7	M1	422.00	1195.00	130.60	503.00	161.30	48.70	286.00	814.00	2176.00	2411.90	3324.70	5736.60	0.1307	0.6076	0.1061	0.6933	1.2252
H1-8	M1	164.00	380.00	36.10	139.00	58.80	6.05	162.00	574.00	1782.00	777.90	2524.05	3301.95	0.062	0.57	0.0734	0.1895	1.1887
H1-9	M1	4.43	64.00	1.52	9.90	13.50	2.08	78.20	382.00	1385.00	93.35	1847.28	1940.63	0.0022	4.8446	0.0456	0.1957	5.9362
H1-10	M1	6.70	134.00	3.07	25.60	36.70	4.18	188.00	761.00	2310.00	206.07	3263.18	3469.25	0.002	8.708	0.0657	0.1539	7.1113
H1-11	M1	1.48	53.00	0.53	4.52	9.52	0.90	70.80	387.00	1509.00	69.05	1967.70	2036.75	0.0007	10.2259	0.0379	0.1066	14.3491
H1-12	M1	18.60	75.40	5.02	22.10	13.44	2.03	60.60	303.00	1254.00	134.56	1619.63	1754.19	0.01	1.1487	0.039	0.2175	1.8781
H1-13	M1	34.60	112.90	6.16	26.80	16.40	1.97	73.50	341.40	1265.00	196.86	1681.87	1878.73	0.0184	0.7535	0.0469	0.1735	1.8613
H1-14	M1	95.00	235.00	22.20	87.00	32.10	2.17	83.30	323.00	1171.00	471.30	1579.47	2050.77	0.0547	0.5372	0.0574	0.1283	1.2316
H1-15	M1	91.00	292.00	28.70	118.00	65.00	7.20	134.00	503.00	2170.00	594.71	2814.20	3408.90	0.0283	1.1355	0.0498	0.2359	1.3752
H1-16	M1	100.00	284.00	26.90	103.00	44.10	7.95	130.30	518.00	1775.00	558.00	2431.25	2989.26	0.038	0.7011	0.0592	0.3207	1.3179
H1-17	M1	55.40	214.00	22.70	98.30	38.40	6.61	85.50	310.00	1177.00	428.80	1579.11	2007.91	0.0317	1.1019	0.0586	0.3527	1.4524
H1-18	M1	50.00	252.00	20.50	103.00	51.90	10.90	168.00	592.00	1799.00	477.40	2569.90	3047.30	0.0187	1.6502	0.0754	0.3569	1.8945
H1-19	M1	121.40	416.00	41.30	165.20	50.90	15.64	105.60	308.70	994.00	794.80	1423.94	2218.74	0.0823	0.6665	0.0857	0.6523	1.414
H1-20	M1	51.20	200.00	21.80	115.00	52.60	2.10	133.00	462.00	1586.00	440.60	2183.10	2623.70	0.0218	1.6332	0.0677	0.0768	1.4408
H1-21	M1	5.78	50.40	1.44	7.30	8.77	0.78	61.40	343.00	1395.00	73.70	1800.18	1873.88	0.0028	2.4121	0.0355	0.1032	4.2047
H1-22	M1	10.90	70.50	2.31	11.90	11.06	1.49	64.90	325.00	1222.00	106.67	1613.39	1720.06	0.006	1.6131	0.0429	0.17	3.3816
H1-23	M1	390.00	940.00	88.00	319.00	107.00	25.00	195.00	614.00	1780.00	1844.00	2614.00	4458.01	0.1477	0.4362	0.0884	0.5292	1.2212
H1-24	M1	0.87	61.90	0.92	9.70	15.70	0.98	89.70	417.00	1490.00	89.09	1997.68	2086.77	0.0004	28.7877	0.0486	0.0803	16.6816

H1-25	M1	171.30	521.00	54.30	215.00	78.90	14.20	182.00	633.00	2020.00	1040.50	2849.20	3889.70	0.0572	0.7322	0.0727	0.3623	1.3002
H1-26	M1	138.00	282.00	29.40	129.00	52.10	17.60	149.00	504.00	1406.00	630.50	2076.60	2707.10	0.0662	0.6002	0.0855	0.6108	1.0656
H1-27	M1	51.70	173.00	15.90	75.40	29.60	2.75	88.20	335.00	1109.00	345.60	1534.95	1880.55	0.0314	0.9102	0.0642	0.1646	1.4523
H1-28	M1	108.10	311.10	32.00	127.60	58.00	12.50	155.40	560.00	1696.00	636.80	2423.90	3060.70	0.043	0.853	0.0739	0.4026	1.2731
H1-29	M1	142.90	488.00	57.60	232.50	92.00	15.11	176.00	532.00	1459.00	1013.00	2182.11	3195.11	0.066	1.0235	0.0973	0.3631	1.2946
H1-30	M1	200.90	823.00	100.90	423.00	190.00	32.50	323.00	906.00	2070.00	1737.80	3331.50	5069.29	0.0654	1.5035	0.1259	0.4011	1.3913
H1-31	M1	28.60	134.00	13.00	69.00	38.30	1.66	115.40	431.90	1655.00	282.90	2203.96	2486.86	0.0117	2.1289	0.0563	0.0763	1.6726
H2S-4	M2-S	79.20	363.00	37.90	162.30	87.40	11.80	174.50	560.00	1436.00	729.80	2182.30	2912.10	0.0372	1.7543	0.0981	0.2922	1.5947
H2S-5	M2-S	18.80	97.60	5.12	24.20	15.90	1.81	66.90	320.00	1264.00	161.62	1652.71	1814.33	0.01	1.3445	0.0427	0.1697	2.3943
H2S-6	M2-S	253.00	1011.00	119.50	510.00	221.00	29.00	362.00	878.00	1971.00	2114.50	3240.00	5354.50	0.0865	1.3887	0.1482	0.3135	1.3994
H2S-9	M2-S	206.00	880.00	75.70	337.00	152.80	21.50	301.00	874.00	2102.00	1651.50	3298.50	4950.01	0.0661	1.1792	0.1156	0.3065	1.6961
H2S-10	M2-S	14.80	89.70	2.87	12.50	14.74	1.55	93.00	474.00	1712.00	134.60	2280.55	2415.15	0.0058	1.5833	0.0438	0.128	3.3126
H2-1	M2	12.60	74.40	5.53	28.40	16.60	2.89	45.50	139.00	427.00	137.53	614.39	751.92	0.0199	2.0944	0.086	0.3215	2.1452
H2-2	M2	22.50	117.00	12.60	64.00	31.80	2.71	81.00	302.00	1518.00	247.90	1903.71	2151.61	0.01	2.2468	0.0431	0.1633	1.6725
H2-3	M2	135.00	459.00	59.00	297.00	142.00	15.90	276.00	610.00	1161.00	1092.00	2062.90	3154.90	0.0784	1.6722	0.1918	0.2456	1.2379
H2-7	M2	19.60	62.00	7.30	28.90	11.80	1.58	22.50	96.00	802.00	129.60	922.08	1051.68	0.0165	0.9571	0.0226	0.2965	1.2475
H2-8	M2	58.00	205.20	26.20	125.90	58.60	4.69	118.50	389.00	1227.00	473.90	1739.19	2213.09	0.0319	1.6062	0.0779	0.1721	1.267
H2-11	M2	65.00	157.00	17.10	69.00	25.00	4.67	44.40	155.00	944.00	333.10	1148.07	1481.18	0.0464	0.6114	0.038	0.4286	1.1334
H2-12	M2	58.20	239.00	19.80	88.70	39.90	5.81	98.20	354.00	1159.00	445.60	1617.01	2062.61	0.0339	1.0899	0.0684	0.2838	1.6945
H2-13	M2	18.30	121.20	13.61	84.40	55.40	13.50	128.30	363.00	790.00	292.91	1294.80	1587.71	0.0156	4.8127	0.1311	0.4896	1.8484
H2-14	M2	63.70	217.00	19.20	77.90	26.10	4.39	71.00	272.70	982.00	403.89	1330.09	1733.98	0.0437	0.6514	0.0583	0.3118	1.4934
Sample APW0001A – Northernmost dyke																		
W1-1	M1	27.00	211.91	1.00	31.36	11.20	0.30	89.40	582.72	1543.90	282.46	2216.32	2498.78	0.0079	0.6593	0.0467	0.0293	9.8367
W1-2	M1	11.40	237.19	1.73	45.68	11.32	0.95	72.10	457.03	1165.68	307.32	1695.76	2003.08	0.0044	1.5789	0.0499	0.1015	12.8488
W1-3	M1	276.00	3260.67	78.71	1875.49	502.60	12.66	1119.55	3199.22	2784.42	5993.46	7115.85	13109.31	0.0451	2.8949	0.3245	0.0516	5.3246
W1-4	M1	80.50	1013.91	21.65	526.45	148.45	3.35	361.76	1307.74	1624.81	1790.96	3297.65	5088.61	0.0225	2.9317	0.1797	0.0442	5.8462
W1-5	M1	302.50	9383.22	152.70	3683.23	1103.32	25.06	2134.66	5931.03	4469.90	14624.97	12560.66	27185.63	0.0308	5.7983	0.3854	0.0499	10.5081
W1-6	M1	140.60	1709.83	40.06	1002.58	284.95	4.96	636.64	2305.94	2366.42	3178.03	5313.95	8491.98	0.027	3.2219	0.2171	0.0356	5.4832
W1-7	M1	564.00	4066.07	75.56	1453.55	178.65	11.24	370.96	1065.72	1813.58	6337.82	3261.49	9599.31	0.1414	0.5035	0.1651	0.1335	4.7406

W1-8	M2	226.00	1277.17	19.60	476.13	38.75	2.63	103.60	450.80	1080.73	2037.64	1637.76	3675.41	0.0951	0.2726	0.0774	0.127	4.6188
W1-9	M1	67.20	586.45	8.74	207.10	25.35	1.64	98.42	492.35	1146.80	894.84	1739.21	2634.04	0.0266	0.5997	0.0693	0.1001	5.8253
W1-10	M1	578.00	4404.90	90.12	1954.84	217.02	10.48	368.45	768.65	1161.63	7244.88	2309.21	9554.08	0.2262	0.5969	0.2559	0.1133	4.6452
W1-11	M2	13.60	282.27	3.82	112.84	27.80	1.01	116.13	595.18	1324.79	440.33	2037.11	2477.45	0.0047	3.25	0.0707	0.0543	9.4292
W1-12	M2	157.00	1451.79	26.56	611.61	101.90	4.65	253.99	934.84	1368.61	2348.87	2562.09	4910.96	0.0521	1.0318	0.1498	0.0883	5.4107
W1-13	M1	150.00	1102.53	24.01	570.97	130.84	3.73	372.63	1174.78	1530.42	1978.34	3081.56	5059.90	0.0446	1.3867	0.1965	0.0517	4.4221
W1-14	M1	123.00	1464.82	27.90	694.84	72.28	5.64	163.76	474.69	968.14	2382.84	1612.23	3995.07	0.0577	0.9341	0.1365	0.1586	6.0181
Sample APW0004A – Southernmost dyke																		
W4-1	M3	69.70	259.10	36.10	165.70	97.60	4.75	172.80	444.00	1467.00	628.20	2088.55	2716.75	0.032	2.2261	0.0951	0.1118	1.2432
W4-2	M3	173.70	762.00	76.60	332.00	160.00	10.77	309.00	863.00	2177.00	1504.30	3359.77	4864.07	0.0538	1.4644	0.1145	0.1481	1.59
W4-3	M2	95.50	318.60	38.61	171.40	69.00	7.61	114.40	305.20	1384.00	693.11	1811.21	2504.33	0.0465	1.1486	0.0667	0.2619	1.2628
W4-4	M2	72.00	231.00	28.50	141.00	67.00	4.59	137.00	410.00	1060.00	539.50	1611.59	2151.09	0.0458	1.4793	0.1043	0.1465	1.2274
W4-5	M3	123.90	464.00	53.90	238.90	118.00	7.30	205.00	475.00	1515.00	998.70	2202.30	3201.01	0.0551	1.514	0.1092	0.1435	1.3666
W4-6	M3	176.60	636.00	80.90	360.00	162.20	11.70	268.00	649.00	2028.00	1415.70	2956.70	4372.40	0.0587	1.4601	0.1066	0.1716	1.2807
W4-7	M3	99.00	338.00	39.70	166.00	76.00	8.90	119.00	278.00	1654.00	718.70	2059.90	2778.60	0.0404	1.2204	0.0581	0.2861	1.2976
W4-8	M3	106.40	422.00	51.00	252.00	154.00	8.30	349.00	883.00	2080.00	985.40	3320.30	4305.70	0.0345	2.3009	0.1354	0.1095	1.3788
W4-9	M3	740.00	3000.00	410.00	1740.00	906.00	70.30	1550.00	3130.00	5240.00	6796.00	9990.30	16786.30	0.0952	1.9464	0.2387	0.1814	1.3109
W4-10	M3	0.91	47.70	0.98	8.72	10.06	2.69	41.30	139.00	435.00	68.37	617.99	686.36	0.0014	17.4976	0.0766	0.4035	12.1059
W4-11	M3	21.90	206.00	11.52	70.50	68.20	6.65	245.00	874.00	2380.00	378.12	3505.65	3883.77	0.0062	4.9507	0.0831	0.1573	3.1215
W4-12	M3	503.00	3330.00	497.00	2740.00	1403.00	103.50	2090.00	3660.00	4930.00	8473.00	10783.50	19256.50	0.0688	4.4342	0.3421	0.1848	1.603
W4-13	M3	115.00	447.00	57.70	250.00	114.00	8.10	169.00	416.00	1431.00	983.71	2024.10	3007.81	0.0542	1.5759	0.0953	0.1784	1.3207
W4-14	M3	280.00	789.00	100.60	370.00	164.20	16.70	255.00	659.00	1745.00	1703.81	2675.70	4379.51	0.1082	0.9323	0.1179	0.2495	1.1315
W4-15	M3	94.00	343.00	28.50	144.00	81.00	23.10	227.00	756.00	2144.00	690.50	3150.10	3840.60	0.0296	1.3699	0.0854	0.5209	1.595
W4-16	M3	38.90	123.70	12.40	52.10	30.40	2.50	88.60	400.20	1448.00	257.49	1939.30	2196.79	0.0181	1.2424	0.0494	0.1473	1.3556
W4-17	M3	55.10	206.00	21.70	96.00	60.70	4.54	159.00	586.00	1821.00	439.50	2570.54	3010.04	0.0204	1.7513	0.0705	0.1413	1.4339
W4-18	M3	61.50	258.00	33.10	153.50	98.00	6.63	202.50	582.00	1759.00	604.10	2550.13	3154.23	0.0236	2.5332	0.0929	0.1439	1.3763
W4-19	M3	75.20	273.00	24.40	103.60	50.60	9.85	147.60	535.00	1562.00	526.80	2254.45	2781.25	0.0325	1.0697	0.0763	0.3485	1.5339
W4-20	M3	60.30	211.00	28.70	128.00	67.10	3.63	105.00	285.00	1286.00	495.10	1679.63	2174.73	0.0316	1.769	0.0659	0.1322	1.2208

W4-21	M3	37.30	177.80	20.71	94.50	47.90	1.81	75.10	219.50	1119.00	378.21	1415.41	1793.62	0.0225	2.0415	0.0542	0.0923	1.5397
W4-22	M3	106.40	500.00	61.50	277.00	139.40	8.79	248.00	649.00	1604.00	1084.30	2509.79	3594.09	0.0447	2.0828	0.1248	0.1445	1.4877
Sample APW1A – Garnet-Pyroxene skarn from the Main-pit																		
APW1A-1	H	877.00	2780.00	446.00	2840.00	1308.00	751.00	1980.00	1820.00	146.00	8250.99	4697.00	12947.99	4.0498	2.371	10.9436	1.4269	1.0699
APW1A-2	H	207.20	750.00	124.20	796.00	381.00	103.30	544.00	485.00	35.10	2258.41	1167.40	3425.81	3.9799	2.9232	12.5066	0.6938	1.1253
APW1A-3	H	433.00	1801.00	290.00	2145.00	1195.00	781.00	1968.00	1855.00	210.00	5864.00	4814.00	10678.00	1.3901	4.3874	7.5623	1.5572	1.2233
APW1A-4	H	236.00	952.00	163.00	1140.00	606.00	132.10	927.00	914.00	103.10	3097.00	2076.20	5173.20	1.5433	4.0821	7.2555	0.5389	1.1683
APW1A-5	H	25.90	116.10	18.60	196.00	209.00	211.00	298.00	95.80	61.10	565.60	665.90	1231.50	0.2858	12.8284	3.9357	2.5851	1.2731
APW1A-6	H	74.80	376.00	61.40	489.00	281.00	136.20	435.00	360.00	77.50	1282.20	1008.70	2290.90	0.6507	5.9722	4.5293	1.1911	1.3354
APW1A-7	H	101.90	411.00	69.70	485.00	232.30	84.50	303.00	234.00	58.90	1299.89	680.40	1980.29	1.1664	3.6241	4.1512	0.9738	1.1738
APW1A-8	H	70.70	300.00	51.00	321.00	152.50	19.58	183.80	156.60	14.30	895.20	374.28	1269.48	3.3333	3.4291	10.3718	0.3576	1.2025
APW1A-9	H	21.50	102.70	11.37	103.50	74.30	66.70	129.00	134.40	152.40	313.37	482.50	795.87	0.0951	5.4939	0.683	2.0831	1.581
APW1A-10	H	33.30	122.00	17.70	131.00	57.20	23.80	80.30	101.80	212.00	361.20	417.90	779.10	0.1059	2.7307	0.3057	1.0737	1.2095
APW1A-11	H	40.50	169.40	24.88	211.70	123.10	143.20	159.70	78.10	37.60	569.58	418.60	988.18	0.7262	4.832	3.4274	3.1228	1.2844
APW1A-12	H	24.80	59.10	7.79	66.30	42.80	29.10	63.60	90.90	141.20	200.79	324.80	525.59	0.1184	2.7436	0.3635	1.7054	1.0234
APW1A-13	H	0.45	1.84	0.27	1.91	1.24	0.54	2.38	4.64	11.24	5.71	18.80	24.51	0.0272	4.342	0.1709	0.9665	1.272
APW1A-14	H	136.00	531.00	87.70	602.00	317.00	90.90	471.00	453.00	49.90	1673.70	1064.80	2738.50	1.8375	3.7055	7.6167	0.7193	1.1702
APW1A-15	H	0.22	8.90	0.65	7.53	5.48	1.93	13.20	28.20	55.70	22.78	99.03	121.81	0.0027	39.4199	0.1912	0.6938	5.6388
APW1A-16	H	37.20	142.00	23.20	152.00	75.00	28.90	107.00	101.00	27.20	429.40	264.10	693.49	0.9221	3.2051	3.1744	0.9864	1.1634
APW1A-17	H	87.00	222.00	30.30	187.00	58.00	57.00	72.00	27.50	17.39	584.30	173.89	758.19	3.3729	1.0598	3.341	2.697	1.0407
APW1A-18	H	8.92	40.70	6.62	58.10	36.70	21.70	55.40	37.70	28.00	151.04	142.80	293.84	0.2148	6.5408	1.5966	1.4715	1.2748
APW1A-19	H	24.40	78.10	11.27	73.60	23.80	33.10	29.30	23.50	29.70	211.17	115.60	326.77	0.5539	1.5507	0.7961	3.8325	1.1336
APW1A-20	H	4.90	19.40	2.88	25.30	13.10	9.00	18.30	9.60	14.08	65.58	50.98	116.56	0.2346	4.2501	1.0488	1.7773	1.243
APW1A-21	H	0.23	1.66	0.14	0.95	0.76	0.51	1.56	4.04	10.09	3.73	16.20	19.93	0.0152	5.2991	0.1248	1.4321	2.2524
APW1A-22	H	0.97	4.40	1.03	10.30	6.60	3.77	8.00	6.90	10.29	23.31	28.96	52.27	0.0636	10.8168	0.6274	1.5864	1.0595
APW1A-23	H	1617.00	5190.00	926.00	6680.00	3410.00	4840.00	5850.00	4140.00	576.00	17823.00	15406.00	33229.00	1.8927	3.3525	8.1956	3.3134	1.0208
APW1A-24	H	1017.00	3510.00	603.00	4160.00	2083.00	1260.00	3310.00	2319.00	221.00	11373.00	7110.00	18483.00	3.1025	3.2561	12.086	1.4672	1.0788
APW1A-25	H	1008.00	3370.00	596.00	4200.00	2210.00	1190.00	3580.00	2660.00	260.00	11384.00	7690.00	19074.00	2.6138	3.4854	11.1111	1.2936	1.0465

APW1A-26	H	35.70	152.00	25.40	182.00	103.00	18.70	154.00	155.00	19.85	498.10	347.55	845.65	1.2125	4.5867	6.2605	0.454	1.2149
APW1A-27	H	1071.00	3640.00	666.00	4590.00	2460.00	722.00	4030.00	4440.00	278.00	12427.00	9470.00	21897.00	2.5973	3.6515	11.6979	0.7011	1.0373
APW1A-28	H	409.00	1559.00	273.00	1850.00	964.00	188.00	1436.00	1468.00	107.90	5055.00	3199.90	8254.90	2.5556	3.747	10.7394	0.4886	1.1229
APW1A-29	H	284.00	1079.00	180.70	1239.00	627.00	290.00	1040.00	1087.00	93.00	3409.70	2510.00	5919.70	2.0588	3.5098	9.024	1.0981	1.1464
APW1A-30	H	255.00	1120.00	180.00	1260.00	726.00	194.00	1180.00	1210.00	122.00	3541.00	2706.00	6247.00	1.4092	4.5261	7.8049	0.6409	1.2582
APW1A-31	H	629.00	2630.00	444.00	3300.00	1962.00	957.00	3450.00	4190.00	312.00	8965.00	8909.00	17874.00	1.3592	4.9588	8.923	1.1247	1.1978
APW1A-32	H	161.00	721.00	124.00	865.00	485.00	65.00	754.00	841.00	77.00	2356.00	1737.00	4093.00	1.4097	4.789	7.9018	0.3287	1.2282
APW1A-33	H	368.00	1432.00	243.00	1657.00	938.00	104.30	1590.00	1830.00	151.60	4638.01	3675.90	8313.91	1.6366	4.0521	8.4634	0.2611	1.1526
APW1A-34	H	373.00	1746.00	305.00	2270.00	1287.00	495.00	2060.00	2130.00	206.00	5981.00	4891.00	10872.00	1.2207	5.4853	8.0695	0.9295	1.2459
APW1A-35	H	610.00	2900.00	454.00	2930.00	1440.00	565.00	1750.00	1570.00	291.00	8334.00	4176.00	12510.00	1.4133	3.7528	4.8528	1.0882	1.3263
APW1A-36	H	112.00	484.00	84.00	568.00	287.00	46.60	317.00	255.00	47.10	1535.00	665.70	2200.70	1.6032	4.0737	5.4311	0.4724	1.201
APW1A-37	H	3.47	15.20	2.20	16.20	8.50	2.64	19.90	28.80	51.50	45.57	102.84	148.41	0.0454	3.8942	0.3118	0.6207	1.3241
APW1A-38	H	112.60	314.00	46.10	325.00	140.70	141.00	185.30	141.50	386.00	938.40	853.80	1792.20	0.1967	1.9865	0.3874	2.67	1.049
APW1A-39	H	92.90	363.00	54.80	420.00	212.00	126.00	302.00	223.00	154.80	1142.70	805.80	1948.50	0.4046	3.6278	1.5743	1.5226	1.2245
APW1A-40	H	88.00	304.00	49.50	393.00	160.00	209.00	168.60	74.20	32.20	994.50	484.00	1478.50	1.8425	2.8904	4.2252	3.8908	1.1086
APW1A-41	H	7.36	45.70	8.03	82.20	50.50	22.20	68.70	44.60	63.50	193.79	199.00	392.79	0.0781	10.9079	0.873	1.1524	1.4308
APW1A-42	H	46.80	187.10	29.10	249.00	173.10	153.40	253.00	135.40	98.90	685.10	640.70	1325.80	0.319	5.88	2.0643	2.2413	1.2203
Sample APW1A1 – Garnet-Pyroxene skarn from the Main-pit																		
APW1A1-1	H	448.00	1382.00	234.60	1680.00	719.00	377.00	898.00	216.10	39.40	4463.60	1530.50	5994.10	7.666	2.5514	18.3919	1.4346	1.026
APW1A1-2	H	498.00	1470.00	225.70	1728.00	982.00	986.00	1315.00	360.00	101.70	4903.70	2762.70	7666.40	3.3014	3.1348	10.434	2.653	1.0553
APW1A1-3	H	535.00	1556.00	253.60	1872.00	938.00	384.00	1247.00	358.00	60.80	5154.60	2049.80	7204.40	5.9325	2.7873	16.5504	1.0856	1.0167
APW1A1-4	H	634.00	1850.00	271.00	2110.00	1339.00	2250.00	1700.00	340.00	135.60	6204.00	4425.60	10629.60	3.1522	3.3575	10.1166	4.5598	1.0742
APW1A1-5	H	325.00	1014.00	171.20	1230.00	537.00	230.00	591.00	123.50	16.58	3277.20	961.08	4238.28	13.2155	2.6267	28.764	1.2483	1.0347
APW1A1-6	H	608.00	1790.00	291.00	2110.00	1087.00	1093.00	1435.00	331.00	77.00	5886.01	2936.00	8822.01	5.3235	2.8422	15.0386	2.6758	1.0242
APW1A1-7	H	677.00	1970.00	321.00	2240.00	1060.00	600.00	1380.00	384.00	55.10	6268.00	2419.10	8687.10	8.2836	2.4891	20.2104	1.5168	1.0171
APW1A1-8	H	441.00	1383.00	221.60	1576.00	785.00	542.00	1008.00	314.00	51.50	4406.60	1915.50	6322.10	5.7732	2.8298	15.7943	1.863	1.0648
APW1A1-9	H	725.00	2050.00	329.00	2320.00	1112.00	950.00	1467.00	392.00	68.00	6536.00	2877.00	9413.00	7.1881	2.4383	17.4088	2.2742	1.0103

Sample 8B1 – Garnet-Pyroxene skarn from the Northern-pit

8B1-1	H	2.35	8.30	1.39	9.40	5.30	7.50	6.50	4.11	5.16	26.74	23.27	50.01	0.307	3.5854	1.0165	3.907	1.1053
8B1-2	H	33.00	111.00	20.00	173.00	115.00	99.00	162.00	77.50	112.70	452.00	451.20	903.20	0.1974	5.54	1.1599	2.2177	1.0399
8B1-3	H	7.46	30.52	5.69	47.60	26.34	21.92	36.40	18.35	49.18	117.61	125.85	243.46	0.1023	5.6131	0.5973	2.1645	1.1275
8B1-4	H	14.20	97.10	12.40	93.20	59.10	31.30	72.60	44.60	26.90	276.00	175.40	451.40	0.3559	6.6165	2.1779	1.461	1.7612
8B1-5	H	1.50	18.30	2.12	20.50	19.90	26.40	40.50	47.50	35.00	62.32	149.40	211.72	0.0289	21.0906	0.9338	2.8433	2.4699
8B1-6	H	10.24	91.60	14.40	150.00	92.90	136.00	115.00	84.10	66.90	359.14	402.00	761.14	0.1032	14.4226	1.3871	4.0231	1.8156
8B1-7	H	2.81	36.30	6.12	74.50	108.00	60.50	177.00	121.00	75.20	227.73	433.70	661.44	0.0252	61.1005	1.8993	1.3379	2.1068
8B1-8	H	11.30	85.00	16.90	183.00	170.00	180.00	244.00	148.00	76.00	466.20	648.00	1114.20	0.1002	23.9165	2.5907	2.7023	1.4804
8B1-9	H	4.55	20.20	3.88	35.00	30.90	64.00	40.80	15.90	31.80	94.53	152.50	247.03	0.0965	10.7963	1.0353	5.5113	1.1571

[1] ΣLREE are calculated from *(La+Ce+Pr+Nd+Sm)*

[2] ΣHREE are calculated from *(Eu+Gd+Dy+Yb)*

[3] ΣREE are calculated from *(ΣLREE+ ΣHREE)*

[4] Data has been C1-normalized according to Boynton (1984)

[5] Geometric mean for Eu (Eu/Eu*) are calculated from $Eu_n - \left(\sqrt{(Sm_n \times Gd_n)}\right) \times 100$

[6] Geometric mean for Ce (Ce/Ce*) are calculated from $Ce_n - \left(\sqrt{(La_n \times Pr_n)}\right) \times 100$

Appendix 4 (table 3) – Zircon U-Pb LA-ICPMS data

Zircon U-Pb LA-ICPMS data

							Isotopic ratios									Isotopic ages in Ma			
								Uncorrected data				PbC-corrected data				Uncorrected		PbC-corrected	
Analytical spot	Zrn type	Pb ppm	U ppm	Th ppm	Th/U ppm	^{204}Pb CPS[1]	^{206}Pb/ ^{204}Pb	^{207}Pb/ ^{235}U/	± 2σ err.	^{206}Pb/ ^{238}U	± 2σ err.	^{238}U/ ^{206}Pb	± 2σ err.	^{207}Pb/ ^{206}Pb	± 2σ err.	^{207}Pb/ ^{206}Pb[2]	± 2σ (Ma)	^{207}Pb/ ^{206}Pb[3]	± 2σ (Ma)
Sample APLH0001A – Högberget granite																			
H1-1	M1	504	5350	2420	0.452	980	2186	1.4146	0.085	0.1125	0.005	9.1200	0.420	0.0847	0.002	1451	40	1309	48
H1-2	M1	571	8200	4020	0.490	337	8282	0.9997	0.025	0.0937	0.002	10.7600	0.250	0.0757	0.001	1131	22	1087	24
H1-3	M1	247	5430	2940	0.541	319	4423	0.6673	0.020	0.0740	0.002	13.7400	0.300	0.0618	0.001	787	32	667	42
H1-4	M1	176	4190	2020	0.482	197	5426	0.5653	0.011	0.0674	0.001	14.9900	0.270	0.0577	0.001	633	30	518	42
H1-5	M1	160	3260	1800	0.552	115	7713	0.6799	0.015	0.0751	0.001	13.4500	0.250	0.0642	0.001	796	22	750	30
H1-6	M1	278	7090	3567	0.503	232	6724	0.5740	0.012	0.0664	0.001	15.2000	0.330	0.0602	0.001	698	34	611	50
H1-7	M1	277	3940	2060	0.523	243	5193	1.1106	0.080	0.1038	0.005	10.4100	0.460	0.0746	0.002	1137	54	1058	54
H1-8	M1	221	5510	3770	0.684	227	5564	0.5603	0.016	0.0665	0.002	15.0600	0.460	0.0584	0.001	643	30	545	41
H1-9	M1	730	6740	4130	0.613	545	5248	1.5967	0.043	0.1310	0.003	7.7400	0.170	0.0858	0.001	1391	22	1334	27
H1-10	M1	1280	8710	7290	0.837	610	7639	2.1981	0.069	0.1687	0.006	6.0300	0.190	0.0926	0.002	1518	28	1480	31
H1-11	M1	1903	10470	4910	0.469	3970	1786	2.6160	0.052	0.1851	0.004	5.5000	0.120	0.0945	0.001	1670	18	1518	20
H1-12	M1	454	7520	3100	0.412	302	6861	0.8779	0.017	0.0851	0.002	11.8700	0.240	0.0728	0.001	1064	24	1008	33
H1-13	M1	511	7400	4086	0.552	248	9153	0.9689	0.040	0.0942	0.003	10.7100	0.350	0.0731	0.001	1058	32	1017	33
H1-14	M1	438	4200	2110	0.502	105	15619	1.5980	0.045	0.1330	0.003	7.7300	0.190	0.0851	0.001	1364	21	1318	25
H1-15	M1	386	6250	2190	0.350	560	2664	0.9128	0.034	0.0852	0.002	11.9500	0.330	0.0728	0.002	1139	49	1008	47
H1-16	M1	305	6850	3189	0.466	288	4948	0.6501	0.014	0.0730	0.001	13.7800	0.260	0.0616	0.001	761	28	660	35
H1-17	M1	497	4580	1683	0.367	162	10049	1.5726	0.052	0.1308	0.003	7.7000	0.190	0.0857	0.002	1365	31	1331	34
H1-18	M1	441	6860	5210	0.759	152	11039	0.8965	0.023	0.0875	0.002	11.5200	0.280	0.0730	0.001	1050	24	1014	31
H1-19	M1	336	4820	2840	0.589	149	8268	0.9893	0.030	0.0938	0.002	10.7800	0.280	0.0749	0.002	1108	26	1066	40
H1-20	M1	998	9060	4720	0.521	457	6834	1.6380	0.044	0.1332	0.003	7.6300	0.190	0.0871	0.001	1408	21	1363	24
H1-21	M1	1199	10650	4130	0.388	444	8446	1.6137	0.040	0.1333	0.002	7.5700	0.140	0.0861	0.001	1378	22	1340	22
H1-22	M1	547	7980	4560	0.571	730	2618	1.0070	0.033	0.0940	0.003	10.8500	0.320	0.0723	0.001	1139	26	994	34
H1-23	M1	455	8690	4310	0.496	1420	1083	0.7703	0.030	0.0694	0.002	14.7600	0.450	0.0669	0.002	1209	56	835	62
H1-24	M1	625	10100	7000	0.693	250	9080	0.8855	0.027	0.0875	0.003	11.5500	0.330	0.0720	0.001	1025	39	986	40

H1-25	M1	629	11520	5500	0.477	520	4342	0.8382	0.036	0.0816	0.003	12.4300	0.430	0.0711	0.002	1055	38	960	49
H1-26	M1	452	4610	2320	0.503	392	4847	1.3503	0.033	0.1159	0.003	8.7200	0.190	0.0815	0.001	1304	25	1234	29
H1-27	M1	392	5230	2860	0.547	430	4244	1.0172	0.027	0.0981	0.002	10.3200	0.250	0.0716	0.001	1074	29	975	31
H1-28	M1	273	5980	2680	0.448	400	3740	0.6396	0.017	0.0726	0.002	13.9500	0.370	0.0601	0.001	738	36	607	50
H1-29	M1	224	5670	2334	0.412	290	4766	0.5748	0.010	0.0667	0.001	15.0800	0.210	0.0594	0.002	691	28	582	55
H1-30	M1	235	3910	2390	0.611	189	6608	0.8392	0.018	0.0840	0.002	12.0200	0.270	0.0700	0.001	999	21	928	38
H1-31	M1	1128	9040	4780	0.529	131	36412	1.8211	0.027	0.1463	0.003	6.8600	0.120	0.0898	0.001	1431	20	1422	20
H1-32	M1	688	6220	2100	0.338	460	5850	1.5481	0.041	0.1298	0.003	7.7600	0.180	0.0841	0.001	1349	25	1295	32
H1-33	M1	440	3280	1460	0.445	266	6150	1.8258	0.057	0.1460	0.004	7.0500	0.190	0.0882	0.001	1440	23	1387	26
H1-34	M1	494	3830	2460	0.642	1220	1418	1.9736	0.103	0.1387	0.005	7.3800	0.310	0.0917	0.002	1682	48	1461	48
H2S-4	M2-S	500	4300	2180	0.507	5880	197	1.7562	0.076	0.0923	0.003	11.9700	0.340	0.0605	0.004	2202	67	622	157
H2S-5	M2-S	1146	6670	3280	0.492	4870	636	2.5639	0.052	0.1610	0.003	6.3900	0.110	0.0934	0.002	1888	26	1496	41
H2S-6	M2-S	299	5860	2705	0.462	1010	1187	0.7268	0.018	0.0690	0.001	14.8200	0.310	0.0638	0.002	1106	37	735	56
H2S-9	M2-S	86	1660	890	0.536	510	751	0.7506	0.029	0.0636	0.002	16.5300	0.670	0.0616	0.007	1329	36	660	247
H2S-10	M2-S	2460	11200	6310	0.563	1150	7617	3.3636	0.127	0.2330	0.010	4.3700	0.190	0.1027	0.002	1709	35	1673	40
H2-1	M2	93	234	116	0.494	108	2778	5.1242	0.235	0.3260	0.013	3.1300	0.110	0.1103	0.004	1864	35	1804	69
H2-3	M2	398	1780	730	0.410	356	3399	3.4130	0.140	0.2292	0.007	4.4700	0.150	0.1028	0.002	1766	32	1675	36
H2-7	M2	247	770	96	0.125	77	10649	4.3942	0.176	0.2940	0.010	3.4500	0.140	0.1073	0.002	1773	32	1754	39
H2-8	M2	770	3000	1900	0.633	240	11250	3.9325	0.127	0.2636	0.007	3.8800	0.110	0.1070	0.001	1769	19	1749	21
H2-11	M2	433	2060	261	0.127	92	17065	3.0429	0.100	0.2218	0.007	4.6000	0.170	0.0982	0.002	1615	21	1590	36
H2-13	M2	286	783	611	0.780	66	14394	5.2354	0.136	0.3349	0.009	3.0560	0.076	0.1122	0.001	1854	13	1835	19
Sample APW0001A – Northernmost dyke																			
W1-1	M1	520	12830	5710	0.445	2900	1121	0.6328	0.069	0.0633	0.002	16.1600	0.540	0.0577	0.003	1000	210	518	122
W1-2	M1	355	6960	3420	0.491	420	5786	0.6960	0.028	0.0773	0.003	12.9900	0.460	0.0627	0.001	784	42	698	48
W1-3	M1	1460	5460	3470	0.636	29500	85	4.2302	0.212	0.1171	0.010	10.7300	0.330	0.0882	0.007	3259	72	1387	155
W1-4	M1	696	7230	3580	0.495	7900	317	1.4815	0.153	0.0916	0.004	11.8100	0.650	0.0713	0.004	1915	118	966	103
W1-5	M1	1996	3580	3710	1.036	43100	54	8.8998	0.812	0.1790	0.003	8.0500	0.640	0.1050	0.014	3752	35	1714	245
W1-6	M1	909	6750	4020	0.596	13000	188	2.0886	0.157	0.0971	0.006	11.4300	0.540	0.0794	0.007	2413	109	1182	169
W1-7	M1	1430	16360	8520	0.521	25700	153	1.3461	0.093	0.0650	0.003	17.4400	0.860	0.0539	0.006	2348	101	367	263

W1-8	M2	1180	11190	3790	0.339	6700	787	1.6364	0.272	0.1290	0.003	8.3000	1.200	0.0738	0.003	1467	68	1036	93
W1-9	M1	374	6540	2920	0.446	139	15899	0.7698	0.041	0.0808	0.005	12.5300	0.530	0.0680	0.002	902	39	869	46
W1-10	M1	678	8620	5550	0.644	8100	269	1.1523	0.087	0.0697	0.015	15.6500	0.730	0.0671	0.004	1955	69	841	112
W1-11	M2	1039	12220	6320	0.517	5680	629	1.3174	0.178	0.0910	0.005	11.4000	1.200	0.0700	0.028	1714	114	928	821
W1-12	M2	1580	8180	7400	0.905	20300	159	2.9945	0.256	0.1227	0.003	9.1100	0.380	0.0887	0.004	2625	132	1398	93
W1-13	M1	1562	8860	3910	0.441	23600	122	2.6795	0.141	0.0992	0.019	11.7500	0.330	0.0777	0.006	2792	75	1139	148
W1-14	M1	916	7740	3400	0.439	7830	411	1.7660	0.104	0.1156	0.003	9.1800	0.430	0.0764	0.004	1813	61	1106	92
Sample APW0004A – Southernmost dyke																			
W4-1	M3	242	2299	850	0.370	1850	436	1.4491	0.033	0.0985	0.003	10.6200	0.300	0.0730	0.004	1744	33	1014	108
W4-2	M3	382	4680	2610	0.558	2730	497	1.1003	0.061	0.0821	0.003	13.0500	0.450	0.0673	0.002	1571	60	847	59
W4-3	M2	117	381	264	0.693	71	5042	4.2373	0.097	0.2739	0.006	3.7240	0.084	0.1088	0.003	1835	18	1779	49
W4-4	M2	307	5550	5080	0.915	1150	1238	0.7745	0.028	0.0755	0.002	13.5300	0.280	0.0620	0.002	1052	49	674	55
W4-5	M3	447	3330	870	0.261	5620	151	1.6669	0.103	0.0757	0.002	15.0500	0.380	0.0770	0.003	2452	70	1121	88
W4-6	M3	438	2834	1378	0.486	3750	280	2.0511	0.110	0.1121	0.004	9.6700	0.380	0.0828	0.004	2134	47	1265	87
W4-7	M3	383	3940	2140	0.543	3010	357	1.2730	0.052	0.0834	0.003	12.7500	0.430	0.0714	0.003	1811	36	969	97
W4-8	M3	557	11110	8280	0.745	2080	1152	0.6920	0.020	0.0700	0.001	14.5700	0.240	0.0591	0.001	977	43	571	48
W4-9	M3	569	6680	2588	0.387	3050	620	1.0995	0.049	0.0895	0.003	11.6800	0.320	0.0655	0.002	1406	34	790	48
W4-10	M3	473	6720	2440	0.363	2200	746	0.9348	0.042	0.0810	0.002	12.6900	0.290	0.0648	0.002	1286	84	768	68
W4-11	M3	644	5650	1128	0.200	2770	687	1.4844	0.072	0.1111	0.004	9.2900	0.280	0.0762	0.003	1565	44	1100	66
W4-12	M3	472	8200	5240	0.639	890	2080	0.7376	0.023	0.0742	0.002	13.6200	0.300	0.0645	0.001	989	48	758	43
W4-13	M3	723	2960	457	0.154	1950	914	3.2618	0.082	0.2116	0.005	4.8400	0.120	0.0990	0.002	1829	34	1605	28
W4-14	M3	359	1567	382	0.244	1360	759	3.3293	0.061	0.2078	0.004	4.9690	0.091	0.0977	0.002	1899	19	1581	34
W4-15	M3	327	2600	1030	0.396	2100	474	1.8713	0.077	0.1200	0.004	8.9600	0.300	0.0809	0.002	1850	53	1219	49
W4-16	M3	272	2299	184	0.080	1230	677	1.7289	0.064	0.1142	0.003	9.0700	0.240	0.0887	0.003	1796	36	1398	56
W4-17	M3	287	1650	897	0.544	1105	807	2.6852	0.139	0.1728	0.010	6.7400	0.430	0.0890	0.002	1843	45	1404	52
W4-18	M3	601	2890	3780	1.308	4810	306	3.1671	0.096	0.1673	0.005	6.3500	0.180	0.0912	0.005	2193	29	1451	94
W4-19	M3	293	2460	499	0.203	1890	463	1.8470	0.123	0.1142	0.003	9.2200	0.250	0.0821	0.005	1915	109	1248	110
W4-20	M3	322	8200	1950	0.238	850	1800	0.6190	0.036	0.0635	0.003	16.2200	0.770	0.0625	0.002	949	38	691	65

W4-21	M3	873	5360	2990	0.558	9740	186	2.4857	0.210	0.1149	0.008	9.6900	0.630	0.0815	0.007	2423	59	1234	159
W4-22	M3	681	5420	1180	0.218	8520	160	1.7899	0.120	0.0794	0.004	14.2500	0.780	0.0730	0.006	2492	69	1014	158
Sample APW1A and APW1A1 – Garnet-Pyroxene skarn from the Main-pit																			
APW1A-1	H	23	404	6	0.016	24	3300	0.7472	0.030	0.0584	0.002	17.7700	0.680	0.0860	0.014	1484	63	1338	315
APW1A-2	H	23	252	4	0.014	12	6225	1.2485	0.038	0.0924	0.002	11.0900	0.320	0.0920	0.011	1586	42	1467	227
APW1A-3	H	40	397	5	0.012	32	4175	1.3562	0.055	0.1013	0.004	10.3300	0.400	0.0930	0.007	1569	41	1488	138
APW1A-4	H	103	915	15	0.016	b.d.	>10^6	1.5720	0.066	0.1257	0.005	8.1500	0.360	0.0908	0.004	1440	32	1442	78
APW1A-5	H	119	743	225	0.303	50	7580	2.1791	0.083	0.1631	0.006	6.3600	0.240	0.0962	0.004	1565	29	1552	70
APW1A-6	H	76	423	5	0.012	b.d.	>10^6	2.3572	0.069	0.1696	0.005	6.1200	0.180	0.1023	0.004	1639	28	1666	76
APW1A-7	H	380	2510	37	0.015	160	8182	2.2299	0.084	0.1805	0.006	5.6000	0.180	0.0883	0.001	1417	26	1389	26
APW1A-8	H	34	148	2	0.012	42	2443	3.1930	0.108	0.2193	0.006	4.6700	0.150	0.1000	0.012	1725	42	1624	223
APW1A-9	H	1119	6170	1500	0.243	b.d.	>10^6	2.6472	0.060	0.2217	0.005	4.5300	0.100	0.0869	0.002	1352	31	1358	33
APW1A-10	H	336	1430	60	0.042	13	79385	3.4200	0.055	0.2508	0.004	4.0000	0.057	0.0989	0.002	1603	23	1603	36
APW1A-11	H	187	797	19	0.024	86	7151	3.2223	0.056	0.2553	0.004	3.9600	0.065	0.0897	0.002	1458	17	1419	43
APW1A-12	H	364	1380	213	0.154	b.d.	>10^6	3.5132	0.102	0.2635	0.008	3.8200	0.120	0.0972	0.002	1561	29	1571	31
APW1A-13	H	308	1027	7	0.007	26	36769	3.8882	0.091	0.2860	0.005	3.5450	0.064	0.0980	0.002	1598	19	1586	29
APW1A-14	H	280	1006	8	0.008	130	6685	4.2058	0.109	0.2950	0.009	3.4200	0.100	0.1011	0.003	1686	39	1644	53
APW1A-15	H	650	2166	81	0.037	b.d.	>10^6	4.4312	0.151	0.2973	0.008	3.3830	0.095	0.1082	0.002	1768	29	1769	29
APW1A-16	H	147	434	3	0.007	44	9864	4.6715	0.241	0.3140	0.016	3.4000	0.190	0.1061	0.003	1764	29	1733	54
APW1A-17	H	378	1189	4	0.004	67	15612	4.7308	0.074	0.3142	0.005	3.1930	0.047	0.1084	0.002	1786	23	1773	29
APW1A-18	H	515	1540	20	0.013	65	22738	4.6874	0.063	0.3206	0.005	3.1500	0.046	0.1054	0.001	1732	14	1721	16
APW1A-19	H	252	744	14	0.019	37	19622	4.7850	0.126	0.3274	0.007	3.0930	0.070	0.1050	0.002	1732	23	1714	33
APW1A-20	H	656	1827	5	0.003	3	601667	4.9967	0.054	0.3315	0.003	3.0260	0.031	0.1091	0.001	1788	13	1785	14
APW1A-21	H	418	1069	8	0.007	24	48667	5.0491	0.074	0.3326	0.005	3.0220	0.043	0.1098	0.002	1801	21	1796	27
APW1A-22	H	665	1657	6	0.003	b.d.	>10^6	5.4206	0.063	0.3552	0.005	2.8320	0.039	0.1105	0.001	1811	15	1808	16
APW1A1-1	H	75	538	9	0.017	b.d.	>10^6	1.9025	0.081	0.1398	0.006	7.4300	0.340	0.0995	0.006	1600	40	1615	105

Sample 8B1 – Garnet-Pyroxene skarn from the Northern-pit

8B1-1	H	405	1192	1	0.001	255	5918	4.8820	0.120	0.3187	0.008	3.1650	0.076	0.1086	0.002	1817	23	1776	25
8B1-2	H	141	146	5	0.033	2360	93	14.7444	1.153	0.4080	0.030	3.0500	0.220	0.1140	0.013	3259	41	1864	206
8B1-3	H	431	1730	189	0.109	1070	1663	3.6441	0.101	0.2609	0.006	3.9010	0.089	0.0925	0.002	1648	26	1478	35
8B1-4	H	509	3320	160	0.048	350	7103	2.2368	0.055	0.1893	0.004	5.3200	0.100	0.0836	0.002	1331	36	1283	37
8B1-5	H	242	1180	25	0.021	260	3769	3.1268	0.137	0.2166	0.008	4.7200	0.170	0.1001	0.002	1709	30	1626	43
8B1-6	H	467	3230	5	0.001	210	10286	2.1364	0.130	0.1714	0.010	5.9900	0.340	0.0894	0.001	1434	27	1413	30
8B1-7	H	433	2990	4	0.001	770	2766	2.0356	0.125	0.1697	0.008	6.1000	0.290	0.0802	0.002	1360	82	1202	47
8B1-8	H	267	903	2	0.002	620	1679	4.2381	0.140	0.2870	0.010	3.5900	0.140	0.0991	0.002	1751	22	1607	40

[1] Baseline subtracted (baseline ~750±20 CPS). Analysis with the mark b.d. indicate concentration below detection limit.

[2] Uncorrected ^{207}Pb / ^{206}Pb age.

[3] PbC-corrected ^{207}Pb / ^{206}Pb age.

Tidigare skrifter i serien ”Examensarbeten i Geologi vid Lunds universitet”:

526. Radomski, Jan, 2018: Carbonate sedimentology and carbon isotope stratigraphy of the Tallbacken-1 core, early Wenlock Slite Group, Gotland, Sweden. (45 hp)
527. Pettersson, Johan, 2018: Ultrastructure and biomolecular composition of sea turtle epidermal remains from the Campanian (Upper Cretaceous) North Sulphur River of Texas. (45 hp)
528. Jansson, Robin, 2018: Multidisciplinary perspective on a natural attenuation zone in a PCE contaminated aquifer. (45 hp)
529. Larsson, Alfred, 2018: Rb-Sr sphalerite data and implications for the source and timing of Pb-Zn deposits at the Caledonian margin in Sweden. (45 hp)
530. Balija, Fisnik, 2018: Stratigraphy and pyrite geochemistry of the Lower–Upper Ordovician in the Lerhamn and Fågelsång -3 drill cores, Scania, Sweden. (45 hp)
531. Höglund, Nikolas, 2018: Groundwater chemistry evaluation and a GIS-based approach for determining groundwater potential in Mörbylånga, Sweden. (45 hp)
532. Haag, Vendela, 2018: Studie av mikrostrukturer i karbonatslagkäglor från nedslagsstrukturen Charlevoix, Kanada. (15 hp)
533. Hebrard, Benoit, 2018: Antropocen – vad, när och hur? (15 hp)
534. Jancsak, Nathalie, 2018: Åtgärder mot kusterosion i Skåne, samt en fallstudie av erosionsskydden i Löderup, Ystad kommun. (15 hp)
535. Zachén, Gabriel, 2018: Mesosideriter – redogörelse av bildningsprocesser samt SEM-analys av Vaca Muertameteoriten. (15 hp)
536. Fägersten, Andreas, 2018: Lateral variability in the quantification of calcareous nannofossils in the Upper Triassic, Austria. (15 hp)
537. Hjertman, Anna, 2018: Förutsättningar för djupinfiltration av ytvatten från Ivösjön till Kristianstadbassängen. (15 hp)
538. Lagerstam, Clarence, 2018: Varför svalde svanödlor (Reptilia, Plesiosauria) stenar? (15 hp)
539. Pilser, Hannes, 2018: Mg/Ca i bottenlevande foraminiferer, särskilt med avseende på temperaturer nära 0°C. (15 hp)
540. Christiansen, Emma, 2018: Mikroplast på och i havsbotten - Utbredningen av mikroplaster i marina bottensediment och dess påverkan på marina miljöer. (15 hp)
541. Staahlnacke, Simon, 2018: En sammanställning av norra Skånes prekambriska berggrund. (15 hp)
542. Martell, Josefin, 2018: Shock metamorphic features in zircon grains from the Mien impact structure - clues to conditions during impact. (45 hp)
543. Chitindingu, Tawonga, 2018: Petrological characterization of the Cambrian sandstone reservoirs in the Baltic Basin, Sweden. (45 hp)
544. Chonewicz, Julia, 2018: Dimensionerande vattenförbrukning och alternativa vattenkvaliteter. (15 hp)
545. Adeen, Lina, 2018: Hur lämpliga är de geofysiska metoderna resistivitet och IP för kartläggning av PFOS? (15 hp)
546. Nilsson Brunlid, Anette, 2018: Impact of southern Baltic sea-level changes on landscape development in the Verkeån River valley at Haväng, southern Sweden, during the early and mid Holocene. (45 hp)
547. Perälä, Jesper, 2018: Dynamic Recrystallization in the Sveconorwegian Frontal Wedge, Småland, southern Sweden. (45 hp)
548. Artursson, Christopher, 2018: Stratigraphy, sedimentology and geophysical assessment of the early Silurian Halla and Klinteberg formations, Altajme core, Gotland, Sweden. (45 hp)
549. Kempengren, Henrik, 2018: Att välja den mest hållbara efterbehandlingsmetoden vid sanering: Applicering av beslutsstödsverktyget SAMLA. (45 hp)
550. Andreasson, Dagnija, 2018: Assessment of using liquidity index for the approximation of undrained shear strength of clay tills in Scania. (45 hp)
551. Ahrenstedt, Viktor, 2018: The Neoproterozoic Visingsö Group of southern Sweden: Lithology, sequence stratigraphy and provenance of the Middle Formation. (45 hp)
552. Berglund, Marie, 2018: Basaltkuppen - ett spel om mineralogi och petrologi. (15 hp)
553. Hernnäs, Tove, 2018: Garnet amphibolite in the internal Eastern Segment, Sveconorwegian Province: monitors of metamorphic recrystallization at high temperature and pressure during Sveconorwegian orogeny. (45 hp)
554. Halling, Jenny, 2019: Characterization of black rust in reinforced concrete structures: analyses of field samples from southern Sweden. (45 hp)
555. Stevic, Marijana, 2019: Stratigraphy and dating of a lake sediment record from Lyngsjön, eastern Scania - human impact and aeolian sand deposition during the last millennium. (45 hp)

556. Rabanser, Monika, 2019: Processes of Lateral Moraine Formation at a Debris-covered Glacier, Suldenferner (Vedretta di Solda), Italy. (45 hp)
557. Nilsson, Hanna, 2019: Records of environmental change and sedimentation processes over the last century in a Baltic coastal inlet. (45 hp)
558. Ingered, Mimmi, 2019: Zircon U-Pb constraints on the timing of Sveconorwegian migmatite formation in the Western and Median Segments of the Idefjorden terrane, SW Sweden. (45 hp)
559. Hjorth, Ingeborg, 2019: Paleomagnetisk undersökning av vulkanen Rangitoto, Nya Zeeland, för att bestämma dess utbrottshistoria. (15 hp)
560. Westberg, Märta, 2019: Enigmatic worm-like fossils from the Silurian Waukesha Lagerstätte, Wisconsin, USA. (15 hp)
561. Björn, Julia, 2019: Undersökning av påverkan på hydraulisk konduktivitet i förorenat område efter in situ-saneringsförsök. (15 hp)
562. Faraj, Haider, 2019: Tolkning av georadarprofiler över grundvattenmagasinet Verveln - Gullringen i Kalmar län. (15 hp)
563. Bjermo, Tim, 2019: Eoliska avlagringar och vindriktningar under holocen i och kring Store Mosse, södra Sverige. (15 hp)
564. Langkjaer, Henrik, 2019: Analys av Östergötlands kommande grundvattenresurser ur ett klimtperspektiv - med fokus på förstärkt grundvattenbildning. (15 hp)
565. Johansson, Marcus, 2019: Hur öppet var landskapet i södra Sverige under Atlantisk tid? (15 hp)
566. Molin, Emmy, 2019: Litologi, sedimentologi och kolisotopstratigrafi över krita–paleogen-gränsintervallet i borrningen Limhamn-2018. (15 hp)
567. Schroeder, Mimmi, 2019: The history of European hemp cultivation. (15 hp)
568. Damber, Maja, 2019: Granens invandring i sydvästa Sverige, belyst genom pollenanalys från Skottenesjön. (15 hp)
569. Lundgren Sassner, Lykke, 2019: Strandmorfologi, stranderosion och stranddeposition, med en fallstudie på Tylösand sandstrand, Halland. (15 hp)
570. Greiff, Johannes, 2019: Mesozoiska konglomerat och Skånes tektoniska utveckling. (15 hp)
571. Persson, Eric, 2019: An Enigmatic Cerapodian Dentary from the Cretaceous of southern Sweden. (15 hp)
572. Aldenius, Erik, 2019: Subsurface characterization of the Lund Sandstone – 3D model of the sandstone reservoir and evaluation of the geoenergy storage potential, SW Skåne, South Sweden. (45 hp)
573. Juliusson, Oscar, 2019: Impacts of subglacial processes on underlying bedrock. (15 hp)
574. Sartell, Anna, 2019: Metamorphic paragenesis and P-T conditions in garnet amphibolite from the Median Segment of the Idefjorden Terrane, Lilla Edet. (15 hp)
575. Végvári, Fanni, 2019: Vulkanisk inverkan på klimatet och atmorsfärcirkulationen: En litterarurstudie som jämför vulkanism på låg respektive hög latitud. (15 hp)
576. Gustafsson, Jon, 2019: Petrology of platinum-group element mineralization in the Koillismaa intrusion, Finland. (45 hp)
577. Wahlquist, Per, 2019: Undersökning av mindre förkastningar för vattenuttag i sedimentärt berg kring Kingelstad och Tjutebro. (15 hp)
578. Gaitan Valencia, Camilo Esteban, 2019: Unravelling the timing and distribution of Paleoproterozoic dyke swarms in the eastern Kaapvaal Craton, South Africa. (45 hp)
579. Eggert, David, 2019: Using Very-Low-Frequency Electromagnetics (VLF-EM) for geophysical exploration at the Albertine Graben, Uganda - A new CAD approach for 3D data blending. (45 hp)
580. Plan, Anders, 2020: Resolving temporal links between the Högberget granite and the Wigström tungsten skarn deposit in Bergslagen (Sweden) using trace elements and U-Pb LA-ICPMS on complex zircons. (45 hp)

LUNDS UNIVERSITET

Geologiska institutionen
Lunds universitet
Sölvegatan 12, 223 62 Lund